FACULTY OF ENGINEERING SCIENCE
DEPARTMENT OF CHEMICAL ENGINEERING
Process Engineering for Sustainable Systems (ProcESS)
Celestijnenlaan 200F - box 2424
B-3001 HEVERLEE, BELGIUM
tel. + 32 0488987569
shushan.yuan@kuleuven.be
https://cit.kuleuven.be/process

Shushan Yuan

ADVANCED MEMBRANE SYNTHESIS METHODS: EXPLORATION OF 3D PRINTED MEMBRANES FOR OIL/WATER SEPARATION AND DEVELOPMENT OF NOVEL POLYMERS FOR ORGANIC SOLVENT NANOFILTRATION

December 2018

KU LEUVEN

ARENBERG DOCTORAL SCHOOL
FACULTY OF ENGINEERING SCIENCE

ADVANCED MEMBRANE SYNTHESIS METHODS: EXPLORATION OF 3D PRINTED MEMBRANES FOR OIL/WATER SEPARATION AND DEVELOPMENT OF NOVEL POLYMERS FOR ORGANIC SOLVENT NANOFILTRATION

Shushan Yuan

Supervisors:
Prof. dr. ir. Bart Van der Bruggen
Prof. dr. ir. Peter van puyvelde

Dissertation presented in partial fulfilment of the requirements for the degree of Doctor of Engineering Science (PhD): Chemical Engineering

December 2018

ADVANCED MEMBRANE SYNTHESIS METHODS: EXPLORATION OF 3D PRINTED MEMBRANES FOR OIL/WATER SEPARATION AND DEVELOPMENT OF NOVEL POLYMERS FOR ORGANIC SOLVENT NANOFILTRATION

Shushan Yuan

Promoter: Prof. Bart Van der Bruggen

Co-Promoter: Prof. Peter Van Puyvelde

Members of the Examination committee:
Prof. Adhemar Bultheel (Chairman, KU Leuven)
Prof. Christian Clasen (KU Leuven)
Prof. Pedro Fardim (KU Leuven)
Prof. Eric Nies (KU Leuven)
Prof. Davide Mattia (University of Bath)

Dissertation presented in partial fulfilment of the requirements of the degree of doctor of Engineering Science (PhD): Chemical Engineering

December 2018

© Shushan Yuan
Uitgegeven in eigen beheer, Shushan Yuan, Celestijnenlaan 200f - box 2424, 3001 Leuven
Alle rechten voorbehouden. Niets uit deze uitgave mag worden vermenigvuldigd en/of openbaar gemaakt worden door middel van druk, fotokopie, microfilm, elektronisch of op welke andere wijze ook zonder voorafgaandelijke schriftelijke toestemming van de uitgever.

All rights reserved. No part of the publication may be reproduced in any form by print, photoprint, microfilm, electronic or any other means without written permission from the publisher.

Acknowledgements

During the three years and three months' stay in KU Leuven, I have a great time here and have learnt a lot. This is a really good moment for me to look back on this wonderful journey. First of all, I would like to show my deepest gratitude and most sincere respect to my promoter Prof. Bart Van der Bruggen for your continuous support, excellent supervision and great encouragement. Thank you very much for accepting me as a PhD student in your group even without an interview. During my entire PhD, you gave me the complete trust and great freedom to explore the interesting topics in the research world. I was really moved by your encouragements and supports when I was trying new things. In addition to the academic aspects, I was truly inspired by your philosophy of helping people when I asked about your ambition in life. That's also what I felt when I was seeking help from you. I will follow your philosophy to try to help people around and to support my future life. Graduation is never the end of the bond between you and me; It's a new start. Let's never say goodbye.

I would like to express utter appreciation to my co-promoter Prof. peter van puyvelde. You opened the door to the world of 3D printing for me and offered me the chance to perform research relating to 3D printing. I greatly appreciate you for the full support and valuable suggestions in my research.

I would like to thanks Prof. Adhemar Bultheel from the Department of Computer Science, KU Leuven, for being the chairman of the jury for my PhD defense. I also would like to express my sincere gratitude to my assessors Prof. Christian Clasen (Department of Chemical Engineering, KU Leuven) and Prof. Pedro Fardim (Department of Chemical Engineering, KU Leuven) for their suggestions during my entire doctoral years. I express my deep appreciation to Prof. Davide Mattia (University of Bath, UK) and Prof. Eric Nies (Department of Chemistry, KU Leuven) for agreeing to be my jury members and their helpful suggestions.

I also would like to thanks two special persons: Prof. Jie Yang (Sichuan University, China) and Prof. Gang Zhang (Sichuan University, China). Prof. Jie, you were my promoter when I was a master student and are the person open the door to the world of research. Thank you very much for leading my career to research. Prof. Gang, you helped me a lot during my PhD thesis. You provided me valuable expertise on the polymer synthesis and saved me out when I lacked materials. Your generous support is the success of my PhD research. Additionally, I would like to thank the support and suggestions from the co-authors in my papers, namely, Prof. Xiaojun Wang from Sichuan University, Prof. Jiansheng Li from Nanjing University of Science & Technology, Dr. Alexander Volodin from the department of Physics and Astronomy, KU Leuven, Dr. Frederik Ceyssens from the Department of Electrical Engineering ESAT and Dieter Strobbe from the department of Mechanical Engineering, KU Leuven. Dieter, thank a million for your support in printing membranes during my PhD. Without your help, I could never know how to start my work in 3D printing.

My appreciation also goes to my colleagues which help me a lot during my PhD. First of all, I would like to express my sincere gratitude to Alena, Herman, Michele, Christine, Hannae and Jacques. Thank you very much for your kind help in the lab and my life. I also thank Junyong Zhu and Jian Li for their company in the three years' study and work in ProcSS. We came to Belgium almost at the same time. We supported each other through thick and thin. Now we will finish our PhD also almost at the same time. This unforgettable experience would never make our friendship fade away. Biggest thanks to all my colleagues in CIT who gave me a lot assistance in my research and made me feel blessed during my PhD: Abdellah, Asma, Bin Liu, Carlos, Duc, Dongyue Li, Fred, Indah, Jing Wang, Junfeng Zhen, Mokgadi, Miaomiao Tian, Pengrui Jin, Ruijun Zhang, Saeed, Shufen Wen, Trang, Violet, Yi Li, Yan Zhao, Zahra, Zhijuan Zhao, Yanling Liu, Zhaohuan Mai, Zhongsen Yan. Furthermore, I would like to thank my students Jasper, Karen for their huge contribution to my thesis. Thank you so much for your assistance and time I spent with.

I extend my gratitude to my dear Chinese friends: Jiahao Zhang, Yun Li, Yuhe Liao, Yongqiang Liu, Zhuangzhuang Liu, Linghui Kong, Yi He, Deweu Jia. Your company and support make my life in KU Leuven more wonderful.

I gratefully acknowledge China Scholarship Council (CSC) of the Ministry of Education, China, for funding me to study in KU Leuven and to give me the chance to change my views of the world and broaden my horizon. This experience definitely will give me an advanced stage for my further development.

Last but not least, I would like to express my deepest gratitude to my parents and my brother who deserves most of the acknowledgement. Dear Dad, Mom and brother, your encouragement, understanding and supporting are always the strongest power to support me through tough time. Thank you for the endless love. I hope I can make you proud.

Shushan YUAN

November 2018

Abstract

Various fabrication methods and different polymers have been applied in recent year to synthesize membranes. Combined with current membrane fabrication methods and commercial polymers, almost all kinds of polymeric membranes ranging from porous microfiltration membranes to dense reverse osmosis membranes have been fabricated in academic and commercial environments. However, membranes synthesized by currently used methods and polymers cannot solve all the problems encountered in industry. Novel fabrication methods with ability to control the structure and surface roughness of a membrane for oil/water separation are still urgently demanded. New polymers with good solvent stability are also highly needed for the fabrication of organic solvent nanofiltration (OSN) membranes. In this thesis, selective laser sintering as 3D printing techniques was explored as a novel membrane fabrication method, to synthesize a porous membrane. In addition, two high-performance polymers, poly (arylene sulfide sulfone) (PASS) and Kevlar, were used to fabricate OSN membranes.

First, a preliminary study was conducted by applying selective laser sintering to produce a membrane from polyamide-12 powder. The obtained membrane turned out to be a porous microfiltration membrane. Results show that processing parameters including laser power, hatch space and scanning count have a significant influence on the structure and performance of a membrane. A membrane fabricated with higher ED, like a larger laser power, a smaller hatch space and 2 counts, would have a denser structure and a lower water flux. Following the same procedure, polysulfone porous membranes were also obtained.

Unlike the smooth flat membrane fabricated from phase inversion, a 3D printed membrane has a rough surface, a 3-dimensional structure and a strong mechanical strength, enabling it to be the perfect substrate to construct a superhydrophobic membrane for oil/water separation. Therefore, two methods were proposed to modify the 3D printed membranes with a superhydrophobic surface. In the first approach, a 3D

printed polysulfone (PSU) membrane was immersed in a candle soot/hexane solution for 40 mins to obtain an ordered candle soot loose network on the surface. In the second method, the 3D printed polyamide-12 (PA-12) membrane was coated with a layer of micro/nano-structural zeolitic imidazolate framework (ZIF-L) and then chemically modified by polydimethylsiloxane (PDMS). Both modified membranes demonstrated superhydrophobic and super-oleophilic properties at the same time and exhibited a high separation efficiency of oil from oil/water mixtures.

Apart from the exploration of novel membrane fabrication methods, two high-performance polymers, PASS and Kevlar, were adopted to synthesize an OSN membrane. An oxidized PASS OSN membrane was fabricated by a post oxidation treatment of the pristine PASS membrane. This membrane showed an excellent chemical stability in aggressive organic solvents, even in 98% H_2SO_4, due to the significantly improved intermolecular interactions. During organic solvent filtration, a high rejection of Rose Bengal (RB), Erythrosin B (EB), Reactive orange 16 (RO16) and Sudan black B (SBB) was obtained, and a high dimethylformamide (DMF) permeability compared to other reported membranes. The Kevlar OSN membrane was synthesized by a simple thermal treatment of a hydrogel ultrafiltration membrane via the regeneration of hydrogen bonds. This membrane exhibited an excellent solvent resistance in commonly used solvents. It maintains a relatively high dye rejection during the filtration of dye solutions for 6 hours.

In conclusion, this thesis shows that membranes fabricated from selective laser sintering can be porous and in the range of microfiltration. Furthermore, the superhydrophobic modified membranes demonstrate a high separation efficiency of oil from oil/water mixtures. In addition, both PASS and Kevlar can be prepared into an OSN membrane. These OSN membranes exhibit an excellent solvent resistance and a high dye rejection in organic solvents.

Samenvatting

Verschillende aanmaakmethoden en verschillende polymeren werden in recente jaren toegepast voor het synthetiseren van membranen. Gecombineerd met huidige membraansynthesemethoden en commerciële polymeren, kunnen bijna alle soorten polymere membranen gaande van poreuze microfiltratiemembranen tot dense omgekeerde osmose membranen worden gefabriceerd in academische en commerciële omgevingen. Membranen die zijn gesynthetiseerd met de momenteel gebruikte methoden en polymeren kunnen echter niet alle problemen oplossen die zich in de industrie voordoen. Nieuwe fabricagemethoden met het vermogen om de structuur en oppervlakteruwheid van een membraan voor olie / waterscheiding te beheersen, zijn nog steeds vereist. Nieuwe polymeren met een grote stabiliteit in solventen zijn ook nodig voor de fabricage van membranen voor nanofiltratie in organische solventen (OSN). In dit proefschrift werd selectieve laser sintering als 3D-printtechniek onderzocht als een nieuwe methode voor membraanaanmaak, om een poreus membraan te synthetiseren. Daarnaast werden twee hoogwaardige polymeren, poly (aryleensulfidesulfon) (PASS) en Kevlar, gebruikt om OSN-membranen te fabriceren.

Eerst werd een voorstudie uitgevoerd door selectieve laser sintering toe te passen om een membraan van polyamide-12-poeder te produceren. Het verkregen membraan bleek een poreus microfiltratiemembraan te zijn. Resultaten tonen aan dat verwerkingsparameters inclusief laservermogen, hatch space en scanning count een significante invloed hebben op de structuur en de prestaties van een membraan. Een membraan vervaardigd met een hogere energiedichtheid, zoals een groter laservermogen, kleinere hatch space en 2 lagen, zou een dichtere structuur en een lagere waterflux hebben. Volgens dezelfde procedure werden ook poreuze membranen uit polysulfon verkregen.

In tegenstelling tot een vlak membraan gefabriceerd via fase-inversie, heeft een 3D-geprint membraan een ruw oppervlak, een driedimensionale structuur en een sterke

mechanische sterkte, waardoor het een perfecte substraat is om een superhydrofoob membraan voor de scheiding van olie en water te construeren. Daarom werden twee methoden voorgesteld om de 3D geprinte membranen met superhydrofoob oppervlak te modificeren. Bij de eerste benadering werd een 3D geprint PSU-membraan gedurende 40 minuten ondergedompeld in een kaarsroet / hexaanoplossing om een geordend kaarsroet netwerk op het oppervlak te verkrijgen. Bij de tweede methode werd het 3D-geprinte PA-membraan bekleed met een laag micro / nano-structureel zeolitisch imidazolaat (ZIF-L) en vervolgens chemisch gemodificeerd met PDMS. Beide gemodificeerde membranen vertoonden tegelijkertijd superhydrofobe en super-oleofiele eigenschappen en vertoonden een hoge scheidingsefficiëntie van olie uit een olie / watermengsel.

Naast de exploratie van nieuwe membraanfabricagemethoden, werden twee hoogwaardige polymeren, PASS en Kevlar, gebruikt om OSN-membranen te synthetiseren. Het geoxideerde PASS OSN-membraan werd vervaardigd door een post-oxidatiebehandeling van het zuivere PASS-membraan. Dit membraan vertoonde een uitstekende chemische stabiliteit in agressieve organische oplosmiddelen, zelfs in 98% H_2SO_4 als gevolg van de aanzienlijk verbeterde intermoleculaire interacties. Tijdens filtratie met organische solventen vertoonde het een hoge weerhouding van RB, EB, RO16 en SBB, en een hoge DMF-permeabiliteit in vergelijking met andere gerapporteerde membranen. Het Kevlar OSN-membraan werd gesynthetiseerd door een eenvoudige thermische behandeling van een hydrogel-ultrafiltratiemembraan via de regeneratie van waterstofbruggen. Dit membraan vertoont een uitstekende solventbestendigheid in courante solventen. Het behoudt een relatief hoge kleurstofweerhouding gedurende de filtratie van kleurstofoplossingen gedurende 6 uur.

Concluderend laat dit proefschrift zien dat poreuze microfiltratie membranen kunnen worden gefabriceerd via selectieve laser sintering. Bovendien vertonen de superhydrofobe gemodificeerde membranen een hoge scheidingsefficiëntie van olie uit olie / watermengsels. Bovendien kunnen zowel PASS als Kevlar worden gefabriceerd

als OSN-membranen. Deze OSN-membranen vertonen een uitstekende solventbestendigheid en een hoge kleurstofweerhouding in deze solventen.

List of Abbreviations

AM	Additive manufacturing
AFM	Atomic force microscopy
BSA	Bovine serum albumin
CA	Contact angle
CDLP	Continuous direct light processing
DMSO	Dimethyl sulfoxide
DMAC	Dimethylacetamide
DMF	Dimethylformamide
DLP	Direct light processing
DMLS	Direct metal laser sintering
ED	Energy density
EDX	Energy dispersive X-ray
EY	Eosin Y
EB	Erythrosin B
FT-IR	Fourier transform infrared spectroscopy
FDM	Fused deposition modelling
HS	Hatch space
IP	Interfacial polymerization
IPA	Isopropanol
MF	Microfiltration
MOFs	Metal-organic frameworks
MO	Methyl orange
NF	Nanofiltration
NMP	N-Methyl-2-pyrrolidone
NIPS	Nonsolvent-induced phase separation
OSN	Organic solvent nanofiltration
PBVF	Patent Blue VF

PASS	Poly (arylene sulfide sulfone)
PEEK	Poly(ether ether ketone)
PAN	Polyacrylonitrile
PA-12	Polyamide-12
PANI	Polyaniline
PBI	Polybenzimidazole
PDMS	Polydimethylsiloxane
PEG	Polyethylene glycol
PI	Polyimide
PIM	Polymer of intrinsic microporosity
PPS	Polyphenylene sulfide
PPSU	Polyphenylsulfone
PP	Polypropylene
PS	Polystyrene
PSU	Polysulfone
PVP	Polyvinyl pyrrolidone
RO16	Reactive orange 16
RO	Reverse osmosis
RB	Rose Bengal
SEM	Scanning electron microscopy
SLM	Selective laser melting
SLS	Selective laser sintering
SL	Sheet lamination
SA	Sliding angles
SLA	Stereolithography
SBB	Sudan black B
THF	Tetrahydrofuran
TIPS	Thermally induced phase separation
TFC	Thin-film composite

TMC	Trimesoyl chloride
UF	Ultrafiltration
XRD	X-ray diffraction
XPS	X-ray photoelectron spectroscopy
ZIF	Zeolitic imidazolate framework

Table of content

Chapter 1: Introduction **1**

1.1 Background 1

1.2 Motivation and objective of the thesis 3

1.3 Conventional membrane fabrication methods 4

1.3.1 Phase inversion 5

1.3.2 Interfacial polymerization 10

1.3.3 Stretching 11

1.3.4 Track-etching 13

1.3.5 Electrospinning 13

1.4 Polymers used to fabricate organic solvent nanofiltration (OSN) membrane 15

1.5 Additive manufacturing 18

1.5.1 Additive manufacture (AM) techniques 19

1.5.2 Application of AM in membrane technology 20

1.6 Thesis outline 22

Chapter 2: Materials and Methods 24

2.1 3D printing polymeric membrane by selective laser sintering 24

2.1.1 Chemicals 24

2.1.2 Filtration setup 25

2.1.3 Porous membrane fabricated by selective laser sintering 27

2.1.4 Superhydrophobic modification of 3D printed membrane 28

2.1.5 Membrane Characterization 30

2.1.6 Filtration experiment 32

2.2 Polymeric membrane fabrication for OSN 33

2.2.1 Chemicals 33

2.2.2 Filtration setup 35

2.2.2 Membrane fabrication 36

2.2.3 Membrane characterization 38

2.2.4 Solvent stability measurement 39
2.2.5 Organic solvent nanofiltration: permeation and rejection 40

Chapter 3: Production of polyamide-12 membranes for microfiltration through selective laser sintering 42
3.1 Introduction 42
3.2 Results and discussions 43
3.2.1 Membrane morphology, porosity and pore size distribution 43
3.2.2 Water flux and rejection 46
3.2.3 Mechanical strength 48
3.3 Conclusion and outlook 49

Chapter 4: Super-hydrophobic 3D printed polysulfone membrane with a switchable wettability by self-assembled candle soot for efficient gravity-driven oil/water separation 50
4.1 Introduction 50
4.2 Results and discussion 53
4.2.1 Morphology of 3D printed polysulfone (PSU) membranes 53
4.2.2 Performance of 3D printed PSU membranes 54
4.2.3 Coating of candle soot on PSU membrane surface 58
4.2.4 Super-hydrophobicity, super-oleophilicity and stability of 3D printed PSU membrane 63
4.2.5 Oil/water separation 66
4.3 Conclusions 69

Chapter 5: Surface architecture of 3D printed membrane via designing micro/nano-structural (zeolitic imidazolate frameworks) ZIF-L for efficient oil/water separation 71
5.1 Introduction 71
5.2 Results and discussion 74
5.2.1 Construction of superhydrophobic single micro-structural ZIF-L layer 74
5.2.2 Construction of superhydrophobic micro/nano structural ZIF-L layer 80
5.2.3 Oil/water separation performance of superhydrophobic membrane 84
5.3 Conclusions 85

Chapter 6: New promising polymer for organic solvent nanofiltration: Oxidized poly (arylene sulfide sulfone) (PASS) 87

6.1. Introduction 87

6.2. Results and Discussion 90

6.2.1 Chemical changes of PASS membrane during oxidization 90

6.2.2 PASS membrane physical properties and filtration performance before and after modification 92

6.2.3 OSN performance of oxidized PASS membranes 98

6.3. Conclusion 101

Chapter 7: Facile synthesis of Kevlar nanofibrous membranes via regeneration of hydrogen bonds for organic solvent nanofiltration 102

7.1 Introduction 102

7.2 Results and discussion 106

7.2.1 Kevlar Nanofiber, Kevlar hydrogel membrane 107

7.2.2 Morphology of Kevlar OSN membranes 111

7.2.3 Performance of nanofiltration membranes 115

7.3 Conclusions 118

Chapter 8: Conclusions and recommendations for future research 120

8.1 General conclusions 120

8.2 Recommendations for future research 122

Reference 124

Curriculum Vitae 149

Chapter 1

Introduction

1.1 Background

Separation processes play a remarkable role in the chemical and pharmaceutical industries, where they account for 40–70% of both capital and operating costs [1-3]. Water is the basic solvent for production processes in the chemical industry, with a global estimated 3:1 volume-to-product ratio [4, 5]. With the growth of water related industries including oil and gas, metalworking, textile and paper, food processing, cosmetics and pharmaceuticals industry [6], an increasing amount of water is consumed, but various technical and management developments lag behind, resulting in a lot of waste water, forming pollution [7]. Thus, treating the vast amounts of produced waste water in a cost-effective way is urgently demanded. In addition to the aqueous waste streams, organic streams produced by organic syntheses in the chemical and pharmaceutical industry are another issue [8]. These organic streams normally contain products with high added value that should be removed from the organic solvents. In addition, organic solvents in these streams, used as raw materials for chemical syntheses and as cleaning agents, have to be recovered or discarded at the end of the process to avoid the associated environmental problems [9]. Conventional treatment technologies, such as hydrocyclones, gas flotation, adsorption, distillation, liquid-liquid extraction, media filtration and macro-porous polymer extraction are able to treat most of these aqueous and organic streams, but suffer from the limits of a low efficiency and a high operation cost [10, 11]. Therefore, a cost-effective separation process is highly needed.

Membranes technology has gained an important place in purification, separation and concentration and been widely used in a broad range of applications. Many different

membrane processes including microfiltration (MF), ultrafiltration (UF), nanofiltration (NF), reverse osmosis (RO) have been developed and are widely used in water treatment, gas purification, energy and pharmaceutical industry, due to the relatively simple process, which is easy to operate, has a low initial investment and low maintenance cost compared to conventional techniques [12-14]. For example, the application of RO in seawater desalination has significantly reduced the energy consumption of seawater desalination to 2–4 kWh/m^3, which makes membrane-based separation processes much more competitive [15, 16].

The membrane is the critical part in these membrane-based separation processes [17-19]. In the last several decades, extensive studies have investigated membrane fabrication by various methods including phase inversion, interfacial polymerization, stretching, track-etching and electrospinning to produce membranes with high performance in terms of selectivity and permeability [20, 21]. Among these membrane synthesis techniques, phase inversion methods, i.e., nonsolvent-induced phase separation (NIPS), thermally induced phase separation (TIPS) and vapor induced separation are the most commonly used processes because of their simplicity and ease to scale up [22-24]. However, in these processes, a large amount of solvents is consumed, resulting in a large waste stream, leading to air and water pollution. Similar observations can be made for interfacial polymerization and electrospinning. Solvent-free processes have been developed as well. Membranes fabricated by track-etching have a very low porosity, and a corresponding relatively low permeability. Additionally, the high cost hinders their extensive application [25]. Stretching offers a promising perspective in terms of environment and cost, but the strict material requirements limit its use to semi-crystalline polymers such as for instance polypropylene. Thus, there is still a long way to go to find a membrane fabrication process with a perfect control of the membrane structure, at low cost and without the extensive use of solvents. New manufacturing techniques developed in other fields may therefore be of interest for membranes.

Additionally, apart from membrane fabrication methods, the polymer itself determines the intrinsic nature and properties of a membrane. So far, almost all commercial polymers have been prepared into a membrane. However, with the spreading of membrane technology in various applications, membranes with special characteristics, for example solvent resistance, are increasingly demanded, especially for applications in aggressive organic media. Many polymers like polyimide (PI) [26], polydimethylsiloxane (PDMS) [27], polyacrylonitrile (PAN) [28], poly(ether ether ketone) (PEEK) [29] and polybenzimidazole (PBI) [30, 31] have been utilized to synthesize solvent resistance membranes. Nevertheless, existing problems such as swelling and dissolution of these polymers in aggressive solvents, which inevitably result in a loss of membrane selectivity, are still a problem for practical applications. Therefore, the exploration of new polymers and advanced modification methods to fabricate membranes is a research trend in the field of membrane technology.

1.2 Motivation and objective of the thesis

Till now, various types of polymeric membranes have been fabricated in academic and commercial environments by varying parameters like polymer, temperature, additives and solvents. However, the two most critical factors that determine the performance and application of a polymeric membrane are the nature of the polymer and the fabrication method. The combination of different polymers and various synthesis methods have resulted in almost all kinds of membrane. However, membranes fabricated by currently used methods and polymers cannot solve all the problems encountered in industry. For example, the most commonly used membrane fabrication method, NIPS, still suffers from the limit of controlling the structure of the fabricated membrane. Solvent resistant polymers are also highly needed for the fabrication of organic solvent nanofiltration (OSN) membrane. Therefore, the exploration of new fabrication methods from other manufacturing sectors and the further development of high-performance polymers in the field of polymer science are meaningful.

In this thesis, selective laser stinting, popularly known as one of the additive manufacturing or 3D printing techniques, will be explored to fabricate a porous membrane. This technique is expected to yield a membrane with pore sizes in the macroscale-range and with a rough surface. More specifically, the following research objectives are defined.

1) To investigate the effect of processing parameters including laser power, hatch space and scanning count on the structure and performance of the membrane.
2) To fabricate polymeric porous membranes from different polymer powders, for example, PA-12 powder and PSU powder.
3) To explore the application of these 3D printed membranes in the field of oil/water separation.
4) To develop superhydrophobic modification methods for 3D printed membranes.

Additionally, high-performance polymers, PASS and Kevlar, will be prepared into solvent resistant membranes for OSN. The objectives are summarized in detail as follows:

1) To find out a proper method to improve the sovlent resistant properties of PASS membrane;
2) To develop a post treatment approach to synthesize a Kevlar membrane in the range of nanofiltration.

1.3 Conventional membrane fabrication methods

The membrane plays the key role in membrane-based processes and determines the technological and economical efficiency of membrane technology. The performance of a membrane can be greatly affected by the fabrication methods. The commonly used membrane fabrication methods are phase inversion, interfacial polymerization, stretching, track-etching and electrospinning [32].

1.3.1 Phase inversion

Phase inversion is the most versatile, economical and reproducible formation method, thus commonly used to fabricate a polymeric membrane from a polymer solution [33]. Almost all soluble polymers can be used to synthesize membranes. The resulting membranes have a typical asymmetric structure (Fig. 1.1) composed of a thin skin layer for separation and a porous support layer resulting from the interplay of mass transfer and phase separation [34].

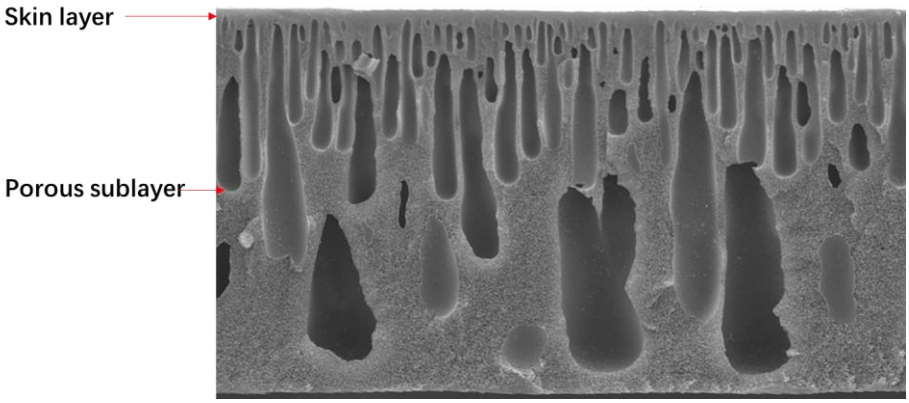


Fig. 1.1 Typical asymmetric structure of a membrane synthesized from phase inversion

Phase inversion can be described as a demixing process whereby the initially homogeneous polymer solution is exposed to a certain environment to induce the transformation of a liquid polymer solution to a solid state in a controlled manner. Depending on the different exposure environment, this transformation can be accomplished in four different ways.

Immersion induced phase inversion is performed by immersing the dope solution in a coagulant (typically water), which is miscible with solvents, but immiscible with the polymer. Demixing and precipitation occur due to the exchange of solvent (from polymer solution) and non-solvent (from coagulation bath). During the solvent exchange, the non-solvent will diffuse into the cast film (at a flux = J_1) whereas solvent

diffuses into the coagulation bath (at a flux = J_2). While the exchange of solvent and non-solvent proceeds, the polymer solution becomes thermodynamically unstable, inducing the demixing. A solid polymeric membrane with an asymmetric structure is finally obtained. Normally, when $J_2 \gg J_1$, "skin" UF membranes with pore size of 10–300 Å are obtained, while at $J_2 = J_1$, MF membranes with pore size of 0.2–0.5 μm are fabricated [35].

Thermally induced phase separation is another popular way to fabricate polymeric membranes. Specifically, a polymer is dissolved in a high-boiling solvent at an elevated temperature to form a homogeneous dope solution. Then, this dope solution is casted into the desired shape, for example a flat-sheet or a hollow fiber. The phase inversion is then induced by cooling the casting solution in a controlled manner. After solvent extraction, a membrane is finally yielded [36]. Thus, the membrane is formed by removing the thermal energy in the dope solution to induce phase separation. In this way, the membrane structure can be tuned by changing the polymer–solvent interaction, cooling rate, cooling media, and thermal gradient.

For solvent evaporation-induced phase separation, apparently, the phase inversion is induced by solvent evaporation. By using this method, a polymer solution is first made in a solvent or in a mixture of solvent and volatile non-solvent. The evaporation of the solvent leads to a demixing/precipitation, resulting in the formation of two phases: a polymer-rich phase and a polymer-lean phase. Finally, a membrane with a porous structure is formed by removing the polymer-lean phase [37].

The last phase inversion method is vapor-induced phase inversion. Vapor (usually water vapor) is used as the nonsolvent phase to bring about the demixing/precipitation of homogeneous polymer solution to generate a porous structure in the film [38].

Among these techniques, immersion induced phase separation is the most commonly used method in the fabrication of polymeric membranes with various morphologies [39, 40]. Therefore, this technique is discussed in detail.

1.3.1.1Immersion induced phase separation

Extensive knowledge has been obtained on how to “tailor” the membrane's pore size as well as its cross-section morphology by the selection of polymer, solvent and non-solvent, additives, precipitation time, bath temperature and other parameters during immersion precipitation [41-47]. Many polymers have been developed into membranes by using this fabrication method. Their advantages and disadvantages are summarized in Table 1.1.

Table 1.1. Main polymers used in membrane formation via immersion precipitation [20, 32, 48-50].

Polymer	**Advantages**	**Disadvantages**
Cellulose acetate	• Hydrophilicity • Flexibility in fabrication • Low cost	• Low thermal resistance (< 30 °C) • Low chemical resistance, pH range (2–8) • Poor resistance to chlorine
Polystyrene (PS) and Polyethersulfone	• High thermal resistance (up to 75 °C) • Wide pH tolerances (1–13) • Good chlorine resistance •Flexibility in membrane fabrication • Wide range of pore size • High mechanical characteristics	• Low operating pressure limits • Hydrophobicity
Polyvinylidene fluoride	• High mechanical strength • High chemical resistance • High thermal stability (up to 75 °C)	• Hydrophobicity
Polyamide (PA)	• Wide pH tolerance • High thermal stability • High mechanical properties	• Poor chlorine resistance

As demonstrated in the table above, a polymer with different chemical nature would endow the resulting polymeric membrane with associated properties. Apart from this, the concentration of the polymer is another key factor determining the structure and performance of a polymeric membrane. A higher concentration in the polymer dope solution results in a membrane with smaller pore size and lower porosity. In contrast, a low concentration in the polymeric dope solution tends to form a membrane with sharp finger-like structures near the surface and many macro-voids near the bottom of the membrane. By increasing the concentration of the dope solution, the finger-like and macro-void structures would be suppressed and the membrane tends to form a sponge-like structure. UF membranes can be obtained within a range of polymer concentration of 12%-20%, whereas polymeric membranes synthesized from nanofiltration membranes are typically prepared from casting solutions with a polymer concentration higher than 20 wt%.

The choice of a solvent−nonsolvent system in phase inversion membrane formation has a dramatic influence on membrane morphology, mechanical properties, interfacial characteristics and separation performance. There is a large number of compatible polymer/solvent−nonsolvent pairs, each with their own specific thermodynamic behavior and miscibility. The higher the mutual affinity (or miscibility) between the solvent and nonsolvent, the more likely instantaneous demixing will occur so that a more porous membrane is obtained. In the case of low mutual affinity, an asymmetric membrane with a dense nonporous top layer is likely obtained. Although other parameters influence the membrane structure, the choice of a solvent−nonsolvent pair is crucial [39, 51, 52].

To tune the structures and properties of a membrane, various additives have been incorporated in the polymer casting solution either to influence the phase inversion process or to endow the membrane with specific properties[53]. These commonly used additive can be classified as the following several categories: inorganic salts, organic compounds and nanoparticles. The inorganic salts and organic compounds can dissolve

in the solvent utilized to prepare polymer dope solution and the coagulant for the phase inversion, demonstrating a significant influence on the exchange between solvent and coagulant during phase inversion. Thus, these additives are normally applied to tailor membrane structure by changing the finger-like macrovoid and sponge formation, to increase pore interconnectivity and hydrophilicity. In specific, the commonly used inorganic salts are $CaCl_2$ and LiCl; the commonly used organic compounds are high molecular weight organic chemicals (such as polyvinyl pyrrolidone (PVP) or polyethylene glycol (PEG)) and surfactants. General results of adding PVP, PEG, LiCl and surfactant are summarized in Table 1.2.

Table 1.2. Influence of commonly used additives on the formation of polymeric membranes

Additives	Influence on membrane morphology
LiCl	• Increase in viscosity of dope solution [54] • Increased the dope's thermodynamic instability in reaction with water • Suppressed macrovoid formation at high concentration [55, 56]
PEG	• Hydrophilicity • Casting solution becomes less stable [57] • Increase pore size • Enhance polymer solution viscosity [58] • Pore-forming agent • Leach out after during operation
Surfactants	• Enhance the affinity between solvent and coagulant • Suppress macrovoids [59]
PVP	• Hydrophilicity • Increase pore number and porosity [60] • Suppresses formation of macrovoids [61] • Leach out during operation [62] • Thicker skin layer

Inorganic nanoparticles and organic nanoparticles as additives have played a significant

role in membrane fabrication, and work as an integral part of the membrane to endow this membrane with additional properties such as hydrophilicity, solvent resistance, antifouling properties and antibacterial properties. Various nanoparticles such as titanium dioxide, mesoporous silica, multi-walled carbon nanotubes and silver have been utilized in fabricating membrane[63-65]. Jamshidi Gohari et al. fabricated polyethersulfone ultrafiltration membrane by blending highly hydrophilic hydrous manganese dioxide nanoparticles with dope solution. The hydrophilicity of the obtained membrane was dramatically improved, and it demonstrate an excellent antifouling properties [66]. To address the membrane fouling bacteria during long-term filtration, antibacterial polyethersulfone membranes were fabricated by incorporating silver particles, exhibiting 100% an inhibition against Escherichia coli (E. coli) growth within 24 h incubation.

1.3.2 Interfacial polymerization

Interfacial polymerization (IP) is the most important method to fabricate thin-film composite (TFC) RO and NF membranes. The first interfacially polymerized TFC membranes were developed by Cadotte et al. in 1980, which was a breakthrough in membrane performance for RO applications [67]. Such TFC membranes synthesized by IP typically have a better salt rejection than an integrally-skinned asymmetric membrane, and a higher water flux [68]. Besides, each layer (i.e., top selective layer and bottom porous substrate) of a TFC membrane can be independently controlled and optimized to achieve the desired selectivity and permeability while offering an excellent mechanical strength and compression resistance [69].

During membrane fabrication, interfacial polymerization takes place at the interface between an aqueous solution containing one monomer and an organic solution containing a second monomer. The porous support membrane is firstly immersed in an aqueous solution containing an aliphatic/aromatic diamine, and then the amine impregnated membrane is immersed in a solution of acid chloride monomer in hexane

for the reaction (Fig. 1.2). After the reaction has proceeded for a certain time, the membrane is treated by heat. Many factors such as the concentration of monomers, solvent type, reaction time, post-treatment conditions and the structure of the support membrane affect the structural morphology and composition of the thin polyamide layer.

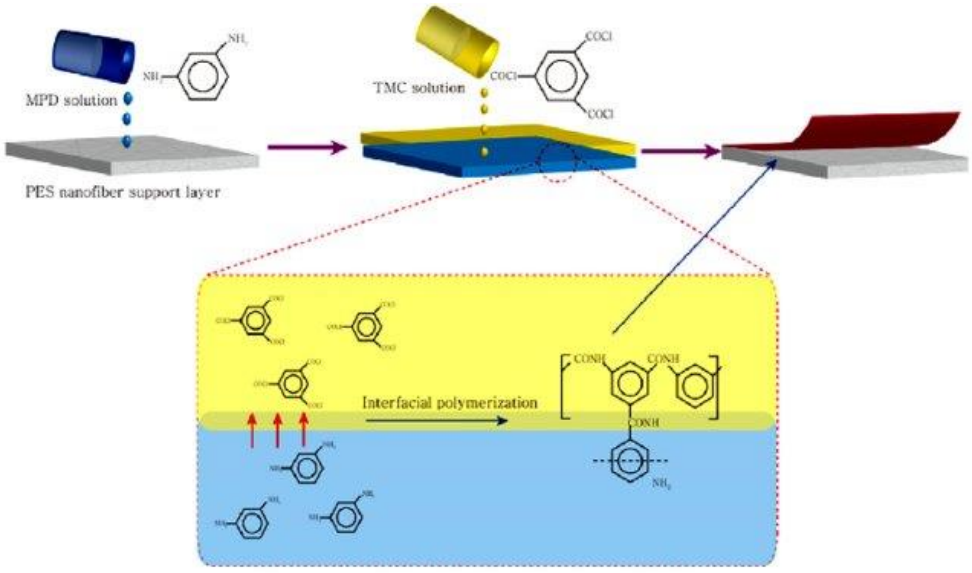


Fig. 1.2 Illustration of interfacial polymerization for the fabrication of thin film composite membranes [70]

The commonly used reactive diamine monomers are piperazine, m-phenylenediamine and p-phenylenediamine. The acid chloride monomers are trimesoyl chloride, isophthaloyl chloride and 5-isocyanato-isophthaloyl chloride. Among these materials, the cross-linked aromatic polyamide composite membrane produced by interfacial polymerization of metaphenylene diamine with trimesoyl chloride (TMC) is the most successful commercial product in the past and present. Recently, novel monomers have been designed to endow the membrane with special properties, such as hydrophobicity, and chlorine resistance [71] [50, 72].

1.3.3 Stretching

Stretching is used to fabricate porous MF, UF membranes. This method is a solvent free process and is suitable for highly crystalline polymers where the crystalline regions of

the polymer provide strength and amorphous regions form a porous structure (Fig. 1.3). The fabrication process by stretching is carried out in three main consecutive stages: (1) production of the precursor film with a lamellar morphology, (2) annealing of the film to thicken the lamellae, and (3) stretching of the film at low temperature to create voids and then stretching at high temperature to enlarge the pores [73]. In this process, material properties including crystallinity, melting point, and tensile strength and the applied processing parameters control the final porous structure and properties of the membranes [74]. The molecular weight and molecular weight distribution of the resins are the main material parameters controlling the crystalline lamellae and amorphous structure. For the fabrication of microporous polypropylene (PP) membranes, the adding a small amount of a long branched PP in the linear PP would improve the orientation of the both crystalline and amorphous phases in the precursor films and increase the porosity of the blend membrane [75, 76]. Annealing is another important factor influencing the performance of the membrane. During annealing, defects resulting from the disruption of chain folding in the blocks or plane slippage are removed. It also improves the long spacing (the total thickness of the periodically repeated crystalline and amorphous phases), resulting in a more uniform lamellae thickness distribution [77]. Cold and hot stretching steps determine the configuration and properties of the obtained membrane.

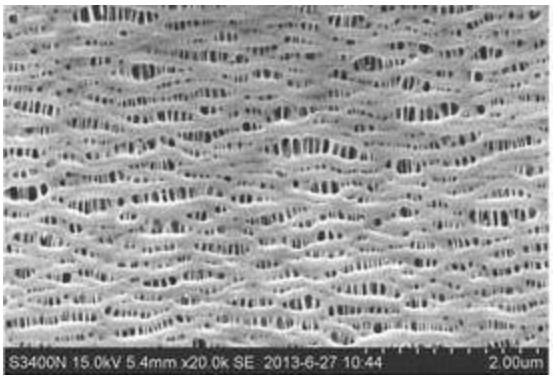


Fig. 1.3 Morphology of surface and pore structures of PP membrane fabricated from stretching [78].

1.3.4 Track-etching

This technique is of interest for its precise control of the pore size distribution of the membrane. In track etching, a nonporous polymeric film is irradiated with energetic heavy ions, leading to the formation of linear damaged tracks across the irradiated polymeric film. A schematic representation of a single ion-irradiation setup is shown in Fig. 1.4a. By this method, the pore size and pore density are independent parameters and can be controlled in a wide range from a few nanometers to tens of micrometers for the pore size, and $1–10^{10}$ cm^{-2} for the pore density. Due to these properties, it makes a simple relationship between water transport properties and membrane structure. The membrane porosity is mainly determined by the duration of irradiation, the pore size is determined by the etching time and temperature. However, in order to reduce the probability of defects, i.e., double or triple pores (Fig. 1.4b), the resulting membranes have a rather low porosity (up to 15%) and pore density compared to the membrane fabricated by phase inversion and stretching [79].

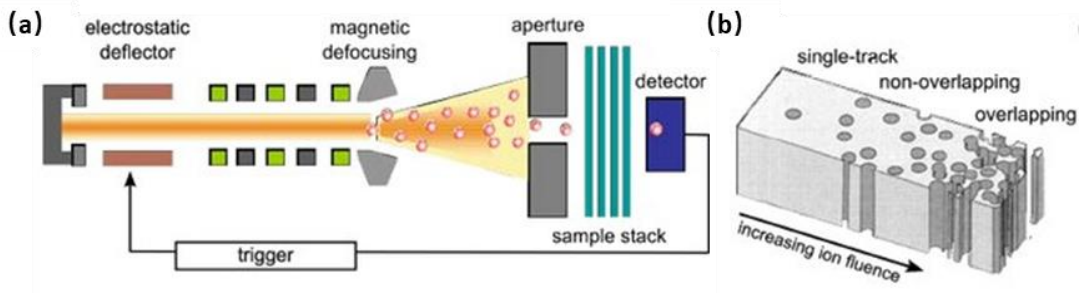


Fig. 1.4 (a) Schematic of single-ion irradiation setup; (b) Track-etched membrane illustrating the porosity regime available by means of ion-track technology: single channel, non-overlapping channels, and overlapping channels. [80].

1.3.5 Electrospinning

The electrospinning technique may be considered as a variant of the electrostatic spraying (for electrospray) process. This technique involves the use of a high voltage to induce the formation of a liquid jet. In specific, a typical electrospinning process

involves the application of an electrical field, induced by a high voltage power supply, between the polymer solution or melt in a spinneret and a collector (a counter or grounded metal electrode such as a plate or a rotating drum) separated at a suitable distance (Fig. 1.5). Under a sufficiently high field, the electrical force would overcome the surface tension of the polymer solution, deforming the pendent drop at the tip of the spinneret into a Taylor cone, and resulting in the ejection of a thin jet [81]. The charged jet undergoes a stable stretching firstly, then it starts bending and whipping randomly, which leads to further stretching due to the combined effects of solvent evaporation and charge repulsion. This unstable stretching can result in a very large spin-draw ratio, where the terminal jet speed can reach a fraction of the sound speed. As a result, the solidified fibers on the collector can be in sub-micron diameter, and have a randomly oriented non-woven structure. After the production of such fiber on the roll, a membrane with non-woven structure is formed.

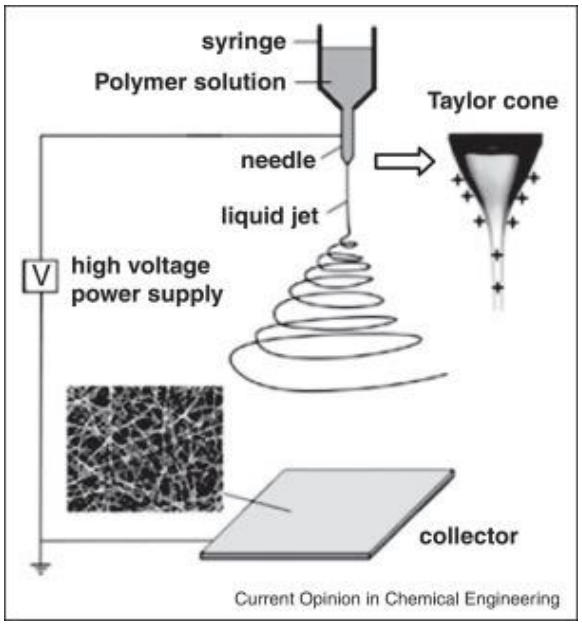


Fig. 1.5 Schematic illustration of the electrospinning process [82, 83]

Careful control of operating conditions and solution parameters can lead to the production of highly porous structures of smooth, defect-free non-woven nanofibrous membranes with different pore sizes. Since the rheology of the polymer solution is vital

to the fiber formation process, solution properties such as polymer molecular weight and concentration directly affect fiber properties. The conductivity of the polymer solution is also known to change properties of the resultant fibers. Fiber properties are also directly affected by operating conditions such as the applied voltage, the solution flow rate and the tip-collector distance. Ambient conditions such as temperature and humidity of the electrospinning chamber can also alter the fiber morphology. The influence of these parameters on the structure of fiber is summarized in Table 1.3.

Table 1.3 Influence of operating conditions and solution parameters on the structure of fiber.

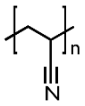
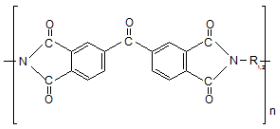
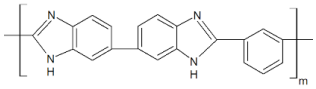
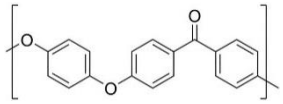
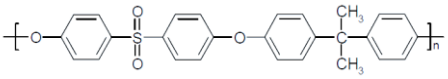
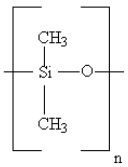
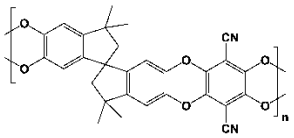
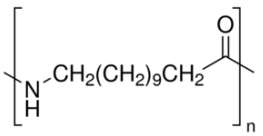
Parameters	Influence on membrane morphology
Concentration/ viscosity	• Low concentration (viscosity) cause instability, resulting in particles rather than fibers [84] • Higher concentration (viscosity) lead to smoother surface and lager diameter of the fiber [85]
Solvent volatility	• When a low volatility is used, solvent loss does not take place as rapidly and wet fibers form • When the solvent volatility is too high, fibers will not be formed as the polymer jet will solidify upon exiting the needle.
Electrostatic potential	• When it is lower than a certain value, continuous fibers cannot be obtained.
Humidity	• The porosity and pore diameter were found to increase with increasing humidity [86]

1.4 Polymers used to fabricate OSN membrane

Apart from the membrane fabrication methods, the polymer determines the intrinsic nature and properties of a membrane, especially for the OSN membrane because of the high requirement of solvent resistance. OSN is a promising energy and waste efficient unit process to separate mixtures down to a molecular level and to reuse organic

solvents. The process has gained increasing attention in the pharmaceutical industry [87]. Membranes with a molecular weight cut-off ranging from 200 to 1000 Da and pore sizes in the range of 0.5 to 2.0 nm are the critical part in OSN [88-90].

Table 1.4 Polymers used to prepare OSN membranes.

Polymer	Structure
PAN	
PI, P84	
PBI	
PEEK	
PSU	
PDMS	
Polymer of intrinsic microporosity	
Polyamides (PA)	

OSN membranes have been prepared from both polymeric and inorganic materials. To have excellent membranes, these materials should have a good mechanical, chemical, and thermal stability. Nowadays, the majority of OSN membranes are based on polymers because of the relatively easy processing, low cost and good reproducibility

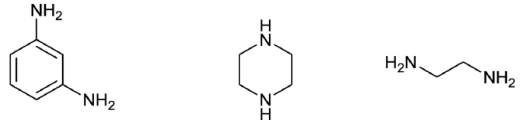
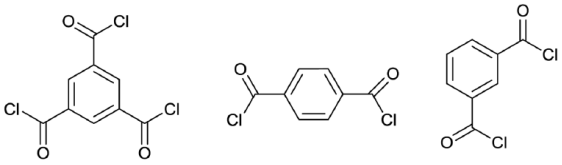
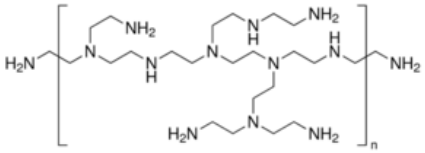
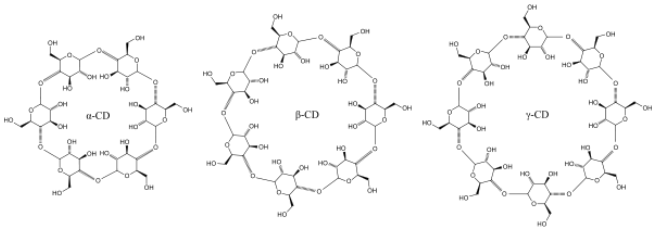
compared to inorganic membranes. It is also much easier to tailor polymeric membranes according to applications compared to ceramic membranes. Table 1.4 lists the polymers that have been used to prepare OSN membranes [91, 92].

To fabricate OSN membranes, these polymers should be firstly dissolved in an aggressive solvent like N-Methyl-2-pyrrolidone (NMP), Dimethylacetamide (DMAC) to obtain homogeneous dope solutions. Membranes are synthesized by immersing the dope solution in a nonsolvent bath for phase inversion. These obtained membranes can be directly used as OSN membranes in non-aggressive solvents (e.g., methanol, ethanol) and in nonpolar solvents (e.g., n-hexane, heptane). However, to be eventually used in an aggressive solvent, a further treatment to improve their solvent resistance is needed. Crosslinking is the most commonly used method to improve the solvent resistance of a polymer; this method aims at creating a network structure. For example, Hendrix et al. [93] reported cross-linked PEEK membranes from lab-synthesized polymers via phase inversion. This membrane demonstrated a Rose Bengal rejection of around 90% in isopropanol. Apart from PEEK, almost all of the polymers listed in the Table 1.4 have to be crosslinked to obtain OSN membranes that can be applied in aggressive solvents.

Alternatively, polymeric membranes synthesized by interfacial polymerization of a thin active separation layer on a solvent resistant UF support membrane have been developed. Details about interfacial polymerization were discussed in Chapter 1.4.2. Table 1.5 lists the monomers and polymers used in the fabrication of OSN membranes. Although PA-based membranes synthesized by interfacial polymerization have been mainly prepared for aqueous applications, they also exhibit perfect performance in organic solvents filtration. Especially in 2015, a substantial progress has been made on the fabrication of such polyamide membranes for OSN. By applying a sacrificial layer during interfacial polymerization, free-standing polyamide nanofilms less than 10 nanometers in thickness on alumina supports were synthesized. These membranes exhibited a high retention of solutes, with acetonitrile permeances up to 112 L/(m²h bar). This is more than two orders of magnitude higher than permeances of

commercially available membranes with equivalent solute retention [94].

Table 1.5 Monomers and polymer used in the fabrication of OSN membrane by interfacial polymerization

Monomer/polymer	structures
Diamines	
Acyl chlorides	
Polyethylenimine	
Cyclodextrin [88]	

1.5 Additive manufacturing

Additive manufacturing (AM), popularly known as 3D printing, is defined as a group of techniques that uses layer-by-layer joining of materials to make parts from 3D model data [95-97]. Unlike conventional manufacturing techniques such as machining, molding and stamping that fabricate products by removing materials from a larger stock or sheet metal, additive manufacturing creates the final shape by adding materials. It has the ability to make efficient use of raw materials and produce minimal waste while reaching a satisfactory geometric accuracy [98, 99]. This technique can transform a computerized 3D solid model to a final product without the use of additional cutting tools [100].Thus, additive manufacturing opens up the possibility of producing parts with complex geometry that are difficult to obtain using material removal processes.

Therefore, AM has become the major innovation in many areas including medical applications [101], art [102], education [103], manufacturing and engineering [104].

1.5.1 AM techniques

To date, various AM techniques have been developed and can be generally categorized into four types: (i) photopolymerization, (ii) powder, (iii) material extrusion, and (iv) lamination [105].

1.5.1.1 Polymerization

Stereolithography (SLA), direct light processing (DLP) and continuous DLP (CDLP) are the three AM techniques using photopolymerization to build parts. SLA is the most common laser-lithography-based technique [106]. In this technique, an ultraviolet laser is used to induce the polymerization of liquid photo-reactive chemicals, and thus form a solid trace. Once the trace is completed, the platform is lowered, so that the part is coated with a new layer of photo-reactive resin. This process is repeated to produce a final solid part [107, 108]. The final parts are typically then post-cured by UV light or heat to improve their mechanical properties.

DLP is a technique using a similar mechanism to build parts. The main difference is that DLP uses a digital light projector screen to flash a single image of each layer all at once, which makes it much faster than SLA [108]. CDLP is also known as Continuous Liquid Interface Production. It produces parts in exactly the same way as DLP [109]. However, it relies on the continuous motion of the build plate in the Z direction, eliminating the separate and discrete steps required for the traditional SLA printer, thus radically reducing the building time between layers.

1.5.1.2 Powder

Powder bed fusion technologies involve the use of a thermal source that induces fusion between the particles of a plastic or metal powder one layer at a time. Selective laser

sintering (SLS), selective laser melting (SLM) and direct metal laser sintering (DMLS) belong to this category. SLS uses a high power laser to fuse small particles of the building materials [110]. The fabrication powder bed is preheated to just below the melting point of the material to minimize thermal distortion and facilitate fusion to the previous layer. The process begins by spreading an initial layer of powder over the build platform. Each layer drawn on the powder is selectively sintered by the laser. The sintered material forms the part, while the un-sintered powder remains in place to support the structure and may be cleaned away and recycled once the build is completed [96]. SLM and DMLS produce parts based on a similar method to SLS. The main difference is that SLM and DMLS are used in the production of metal parts. SLM achieves a full melt of the powder, while DMLS heats the powder to near melting temperatures until they chemically fuse together [95, 111].

1.5.1.3 Material extrusion

Fused deposition modelling (FDM) is the most widely used 3D printing technology. It works by extruding a filament of polymeric material at the appropriate temperature [112]. When the thermoplastic filament is pushed through a heated nozzle, it is melted. The printer continuously moves the nozzle around, laying down melted material at precise locations following a pre-determined path. The extruded hot material hardens and adheres to the preceding layer [113].

1.5.1.4 Lamination

Sheet lamination (SL) technology is mainly used to produce colored objects in a high detailed resolution and works by gluing shaped layers together by adhesive. These shaped layers are normally cut from papers or aluminum foils by laser or sharp blade [114].

1.5.2 Application of AM in membrane technology

Recently, the use of AM has been extended to membrane systems, including spacers and membranes. Membrane modules with optimized spacers produced through SLS were used by Li and coworkers to reduce fouling, increase mass transfer and reduce the concentration polarization at the membrane surface [115]. Their novel spacer had a 30% higher Sherwood number (a larger Sherwood number indicates a high mass transfer) and 40% lower power consumption as compared to the optimal non-woven spacers [115]. Digital light processing (DLP) prototyper offered freedom in interface geometry optimization of PDMS membranes for a gas-liquid contactor [116-118]. Wessling at al. reported a three-dimensional membrane geometry using rapid prototyping (Fig. 1.6) [116]. The novel membrane geometries display superior mass transport of CO_2 through PDMS into water compared with computational fluid dynamics simulations of state-of-the-art hollow-fiber membranes of equal geometry parameters. In addition, ink-jet printing has been shown to assist in the fabrication thin film composite membranes [119, 120]. Arnusch et al. explored the hybridization between ink-jet printing technology and the interfacial polymerization process to fabricate thin film composite membranes. They found that the combination of printing technology with interfacial polymerization facilitated the fabrication of unique selective layers and demonstrated to be a potentially useful new laboratory membrane fabrication tool.

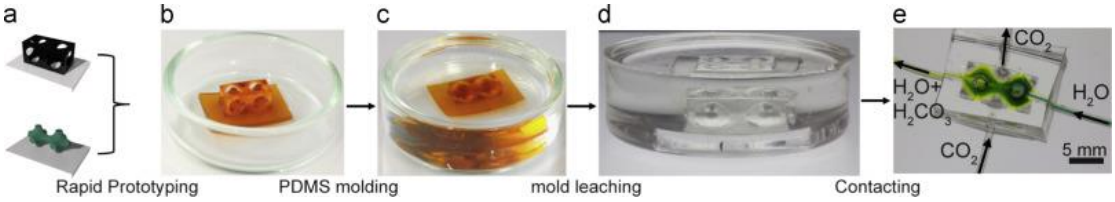


Fig. 1.6 Preparation of tricontinuous membrane geometries based on three different triple periodic minimum surface architectures. (a)–(e) Step-by-step fabrication for the Schwarz-P geometry: (a) rapid prototyping of the sacrificial mold, (b, c) backfilling of the mold with PDMS followed by thermal curing, (d) alkaline removal of the mold material and (e) Obtained membrane under steady-state operation [116].

1.6 Thesis outline

The aim of this thesis is to explore the use of selective laser sintering to fabricate porous membranes and to develop high-performance polymers, PASS and Kevlar, into solvent resistant membranes for organic solvent nanofiltration. Chapter 2 gives a detailed description of the membrane fabrication methods, characterization of membranes and filtration processes. Special attention is paid to the membrane fabrication process by selective laser sintering, the superhydrophobic modification of 3D printed membranes and the fabrication of PASS and Kevlar OSN membranes.

Chapters from 3 to 5 mainly focus on the fabrication of polymeric porous membranes by selective laser sintering for oil/water separations. More specifically, chapter 3 demonstrates a study on the printing of polyamide-12 porous membranes by selective laser sintering. The effect of processing parameters including laser power, hatch space and scanning count on the structure and performance of the 3D printed membrane is investigated in detail. By using a different polymer powder, Chapter 4 explores the fabracation of a porous membrane from amorphous PSU powder by selective laser sintering. Moreover, this 3D printed membrane was modified by candle soot particles to endow it with superhydophobic properties. This superhydrophobic membrane was applied in oil/water separation. Its performance in oil/water separation is detailly investigated. In Chapter 5, to construct a superhydrophobic porous surface for efficient oil/water separaton, a micro/nano-structural zeolitic imidazolate framework (ZIF-L) layer was constructed on the 3D printed PA membrane to yield a multiscale structural surface by designing the structure of ZIF-Ls. After coating with PDMS, water wettability and oil/water separation performance of this membrane were studied.

Chapter 6 and Chaper 7 spotlight the synthesis of solvent resistant membranes for OSN from PASS and Kevlar. In chapter 7, PASS membranes were fabricated by phase inversion. These membranes were oxidized by a post treatment to increse interactions between polymer chains. The solvent resistance and OSN performance of these

membranes were investigated. Chapter 7 demonstrated another OSN membrane fabraicted from Kevlar. Hydrogel UF membranes were fist synthesized. The OSN membrane was obtained by a simple heat treatment of these hydrogel membranes. The solvent resistance and OSN performance of these membranes were stutied.

Finally, general conclusions and future perspectives are demonstrated in Chapter 8.

Chapter 2

Materials and Methods

This section outlines the materials and methods used in this thesis. The first section summarizes the detailed membrane preparation by selective laser sintering for oil/water separation. The second section covers the synthesis of organic solvent nanofiltration (OSN) membranes from poly (arylene sulfide sulfone) (PASS) and Kevlar.

2.1 3D printing polymeric membrane by selective laser sintering

2.1.1 Chemicals

2.1.1.1 Polymer power for sintering

Polysulfone (PSU) powder with particle size around 50 μm was grinded from PSU pellets. Polyamide-12 powder (trade name PA2200) was obtained from EOS GmbH (Germany). PA2200 is the standard SLS grade with average diameter of 59 um and a span of 0.84, as shown in Table 2.1. For the membrane production, a mixture of 30 % recycled and 70 % virgin powder was used. PS latex (diameter 1 μm) was purchased from Sigma–Aldrich and used as model for rejection tests.

Table 2.1 PA12-PA2200 particles size distribution

	D_{10} (μm)	D_{50} (μm)	D_{90} (μm)	Span
PA12-PA2200	38.8	58.6	88.3	0.84

Span was used to define the particle size distribution width.

$$\text{Span} = \frac{D_{90} - D_{10}}{D_{50}} \qquad (2.1)$$

in which D_{50} has been defined as the diameter where half of the population lies below this value. Similarly, 90% of the distribution lies below D_{90}, and 10% of the population

lies below D_{10}.

2.1.1.2 Commercial chemicals from companies

Hexane, petroleum ether, heptane and mineral oil were purchased from Sigma–Aldrich (Belgium). PDMS (Sylgard 184A), curing agent (Sylgard 184B) $Zn(NO_3)_2 \cdot 6H_2O$ and 2-methylimidazole (Hmim) were purchased from Sigma-Aldrich (Belgium). $Zn(NO_3)_2 \cdot 6H_2O$ and Hmim were used to synthesize Zeolitic imidazolate frameworks (ZIFs).

2.1.1.3 Chemicals synthesized in lab

In order to obtain candle soot particles, a clean metal plate was placed on the top of a candle mid-flame position at a distance of 2 cm for 10 minutes [121]. Candle soot deposited on the metal plate was scraped off and stored for the membrane modification.

2.1.2 Filtration setup

A lab scale crossflow filtration setup provided by Zhejiang Circle-tech Membrane Technology Co. Ltd. (China) (Fig. 2.1) was used to measure the water flux of 3D printed membranes. During the filtration, a membrane with a diameter of 8 cm is put in the cell. The feed solution is pumped to the cell by a booster pump.



Fig. 2.1 Picture of filtration unit of the crossflow filtration setup.

The oil/water separation was performed in a lab assembled apparatus (Fig. 2.2). The membrane is placed between two glass vessels. During filtration, the oil/water mixture is poured into the top glass vessel. The separation is hence driven by gravity.

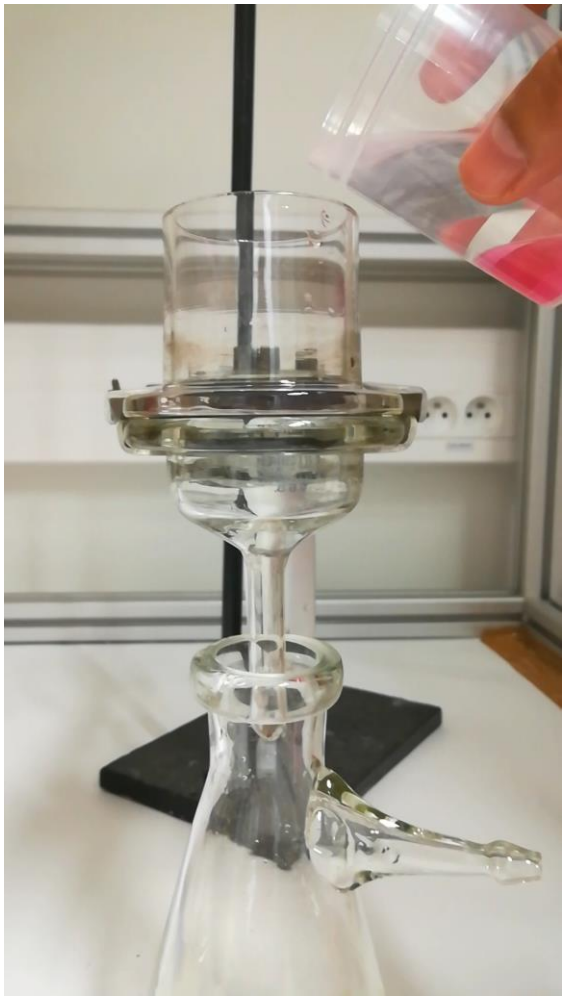


Fig.2.2 Lab assembled apparatus for oil/water separation

2.1.3 Porous membrane fabricated by selective laser sintering

2.1.3.1 3D printing of polyamide-12 membranes

A (porous) membrane is a film with high porosity, and one layer of deposition and sintering of polyamide powder is already enough to fabricate a thin film which can be used as membrane. Selective laser sintering of polyamide-12 powder was performed on a DTM Sinterstation 2000 equipped with a CO_2 laser (Gaussian profile with diameter 450 micron). The process is carried out under N_2 atmosphere with up to 5.5% O_2. The powder bed is preheated to 163 °C and subsequently the laser scans one single powder layer on the powder bed surface with circular geometry and diameter of 8 cm.

Three laser parameters are varied: laser power P, hatch space (HS, the distance between laser tracks) and the scanning count. The scan speed v is kept constant at 1 m/s. Laser power ranges from 5 to 20 W. Hatch spaces of 0.1 mm and 0.15 mm were tested. The energy density (ED) is an engineering parameter that combines these laser parameters.

$$ED = \frac{P}{HS \,.v} \tag{2.2}$$

The effect of a single and double scan count on the structure and performance of 3D printed membranes was also studied. Table 2.2 lists the detailed processing parameters for each sample. For every combination of processing parameter, samples are produced in threefold.

Table 2.2 Membrane samples and their processing parameters

Sample	a1	a2	a3	a4	b1	b2	b3	c1	c2	c3	c4	d1	d2	d3
P (W)	5	10	15	20	5	10	15	5	10	15	20	5	10	20
HS (mm)	0.1	0.1	0.1	0.1	0.1	0.1	0.1	0.15	0.15	0.15	0.15	0.15	0.15	0.15
ED (J/mm²)	0.05	0.1	0.15	0.2	0.05	0.1	0.15	0.033	0.067	0.1	0.13	0.033	0.067	0.13
Count	1	1	1	1	2	2	2	1	1	1	1	2	2	2

2.1.3.2 3D printing of PSU membranes

Following the same procedure, a series of PSU membranes with a diameter of 8 cm were fabricated by SLS. In order to find the optimal membrane for the preparation of super-hydrophobic PSU membranes, the effect of processing parameters, like hatch space (HS) and the scanning count, on the structure and performance of PSU membranes were investigated. The processing parameters for the four membranes, M1, M2, M3 and M4, are summarized in Table 2.3.

Table 2.3 Processing parameters of PSU membranes

Sample	Laser Power (W)	Hatch space (mm)	Scanning count
M1	15	1.5	1
M2	15	1.5	2
M3	15	0.8	1
M4	15	0.8	2

2.1.4 Superhydrophobic modification of 3D printed membrane

2.1.4.1 Superhydrophobic modification of PSU membrane by candle soot

After obtaining the candle soot from the metal plate, a mixture of candle soot/hexane solution (0.1 wt%) was formed by dispersing 40 mg of candle soot particles into 40 g hexane by sonication for 30 minutes. Then, the 3D printed PSU membranes were immersed in this solution for a certain time under sonication. Afterwards, the PSU membranes were placed in an oven at 60 °C for 10 minutes to evaporate the hexane on the membrane surface. Finally, the PSU membranes were rinsed in hexane to remove the loosely attached candle soot particles and dried in a fume hood at room temperature.

The immersion time plays an important role on the amount of candle soot deposited on the 3D printed PSU membranes. In order to find the optimal time

for the membrane modification, eight pieces of small square membrane samples with a size 1.5x1.5 cm^2 were cut from the PSU membrane. These samples were immersed in hexane for 1 hour under sonication to remove the PSU powder that was not firmly connected to the membranes. Then, they were dried in an oven for 10 minutes, and subsequently weighted on an analytical balance. Afterwards, these samples were immersed in a container with 10 ml 0.1 wt% candle soot/hexane solution for 4 mins, 8 mins, 12 mins, 16 mins, 20 mins, 24 mins, 28 mins and 40 mins respectively. Following the candle soot coating route described above, 8 dry modified PSU membrane samples were hence obtained. The mass of these samples was measured again. Based on the mass of the membrane modified before and after, the deposition rate of candle soot on the membrane surface was calculated by the following equation:

$$R_{\text{dep}} = \frac{m_2 - m_1}{m_1} \tag{2.3}$$

in which, R_{dep} (mg/g) is the deposition ratio of candle soot particles, m_1 and m_2 are the mass of the membrane samples modified before and after respectively.

2.1.4.2 Superhydrophobic modification of PA membrane by ZIF-Ls and PDMS

Synthesis of free ZIF-L crystals: $Zn(NO_3)_2 \cdot 6H_2O$ (0.1 mol/L) and 2-methylimidazole (0.4 mol/L) aqueous solutions were prepared. Then, a 20 ml 2-methylimidazole aqueous solution and a 10 ml zinc nitrate aqueous solution were mixed together for reaction and stirred by a magnetic stirrer with a speed of 500 rpm. One ml of the mixture with ZIF-Ls was taken out from the reaction solution after 5 min, 10 min, 20 min, 30 min, 40 min, 60 min, 80 min, 100 min and 120 min. These products were collected by centrifugation (at 4000 rpm for 10 min) and washed with water three times, and then dried in a vacuum oven at 60 °C overnight.

Synthesis of ZIF-Ls on 3D printed PA membrane: $Zn(NO_3)_2 \cdot 6H_2O$ (0.1 mol/L) and 2-methylimidazole (0.4 mol/L) aqueous solutions were firstly prepared. Then 3D printed PA membranes were immersed in the 20 ml 2-methylimidazole aqueous solution. After that, 10 ml zinc nitrate solution was added under stirring. After reaction for different times (5 min, 10 min, 20 min, 30 min, 40 min 60 min, 80 min, 100 min and 120 min), a series of wet ZIF-L coated PA membranes were fabricated. These ZIF-L coated PA membranes were washed with water and then dried in an oven at 60 ^oC for 12 hours.

Synthesis of multiscale ZIF-L by second growth: First, 20 ml of Hmim (0.8 mol/L) and 20 ml of $Zn(NO_3)_2 \cdot 6H_2O$ (0.05 mol/L) solutions were prepared. The obtained ZIF-L coated PA membranes were placed into the above mixed two solutions for different times (5 min, 15 min, and 30 min). The ZIF-L coated 3D printed membranes obtained in this way were washed with pure water, and dried in an oven at 60 ^oC for 12 hours.

Superhydrophobic modification of ZIF-L coated PA membrane by PDMS: The PDMS coating solution was prepared as reported.[122] Briefly, PDMS (1 g) and curing agent (0.1 g) were dissolved in 40 mL n-hexane and ultrasonically dispersed for 2 min.[122] Then, various ZIF-L coated PA membranes were immersed in the coating solution for 10 min. After the n-hexane on the surface of these membrane was evaporated, these membranes were placed in an oven at 70 ^oC for 30 mins for solidification.

2.1.5 Membrane Characterization

2.1.5.1 Scanning electronic microscopy (SEM)

The surface, cross-section and bottom surface of the prepared membranes, and the nanoparticles, were visualized by SEM imaging. The cross-section samples were obtained by mechanical fracturing the membranes in liquid nitrogen. These samples were then dried and sputter-coated with a 5 nm thickness gold layer under an argon atmosphere to achieve the necessary conductivity. The microscopic analyses were performed at 12 kV using a Philips Scanning Electron Microscope XL30 FEG (the

Netherlands).

2.1.5.2 Mechanical strength test

A mini tensile/compression machine (INSTRON 5943) was used to measure the tensile strength of the produced membranes. The samples were made by cutting the membranes into small strips with a width of 5 mm and a length of 5 cm. The sample thickness was measured by a thickness gauge.

2.1.5.3 Pore size distribution and porosity

The pores on the separation layer of membrane is the functional part of a membrane that greatly affects the selectivity and permeability, and it is very important to know the mean pore size and pore size distribution of a membrane. A POROLUX 1000 device (Porometer, Eke, Belgium) was used to measure these two properties. Details about this measurement technique have been described by Francis et al**.** [123]

Apart from pore size, porosity is another factor that influences the permeability of a membrane. The porosity of the PA membrane was obtained from the weight of the membrane in the wet and in the dry state. The wet membrane was weighed after the remaining water drops on the membrane surface were removed with filter paper. Finally the wet membrane was placed into an air-circulating oven at 60℃ for 24 h, after which its dry weight was measured. The porosity of a membrane was calculated by the following formula [124]**:**

$$P = \left(\frac{W_w - W_d}{Ad\rho}\right) \times 100\% \qquad (2.4)$$

Where P_r is the porosity, W_w and W_d are the weights of the membrane at the wet and dry state, respectively, A is the membrane area (m^2), d is the thickness of membrane in the wet state, and ρ is the density of water (1 g cm^{-3}). The reported porosity data are averaged values of 4 samples for each membrane.

2.1.5.4 Contact angle

The water and oil contact angles (CAs) and sliding angles (SAs) were measured by a contact angle goniometer (OCA20, Data physics Instruments, Germany) at room temperature. The average water CA and SA values were obtained by measuring the same sample in at least three different positions. The error bar of the contact angle was calculated based on three results.

2.1.6 Filtration experiment

2.1.6.1 Water flux and rejection measurement under pressure

A cross flow filtration setup (Fig. 2.1) was used to study the permeation and rejection of the resulting membranes. The effective area of the filtration cell was 22.22 cm^2. The water flux is normally used to express the rate at which the water permeates the membrane. It is typically defined as follows:

$$J = \frac{V}{A \times \Delta t} \qquad (2.5)$$

where V is the permeate volume (L), A is the effective membrane area (m^2), Δt is the permeation time (h).

The permeation of 3D printed polyamide membrane was measured at a pressure of 1 bar. The permeation of 3D printed polysulfone membrane was measured at a pressure of 2 bar. The water permeation was calculated as follows:

$$P = \frac{J}{\Delta P} \qquad (2.6)$$

in which ΔP is the applied pressure (bar); J is the flux.

In the rejection tests, polystyrene latex with diameter 1 um was used as a model to test

the rejection of 3D printed polyamide membranes. The rejection R is given by

$$R(\%) = \left(1 - \frac{C_p}{C_f}\right) \times 100 \tag{2.7}$$

in which C_p and C_f (mg/mL) are the concentration of permeate and feed solutions, respectively.

2.1.6.2 Gravity driven water or solvent permeation

The gravity driven water (solvent) flux of 3D printed membranes was measured by utilizing the lab scale assembled apparatus (Fig.2.2). The flux was calculated by equation (2.5).

2.1.6.3 Oil/water separation

A lab assembled device (Fig. 2.2) was used to study oil/water separation. A series of oils including hexane, petroleum ether, heptane and mineral oil was used. During this separation process, gravity was the only driving force for the separation of oil/water mixtures (50% v/v). The gravity driven flux was calculated by Eq. 2.5 and the separation efficiency was calculated by the following equation:

$$\eta = \frac{m_1}{m_0} \times 100\% \tag{2.8}$$

in which η is the separation efficiency; m_1 and m_0 are the mass of water before and after the separation process, respectively.

2.2 Polymeric membrane fabrication for OSN

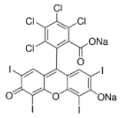
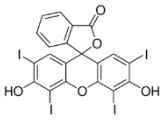
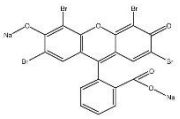
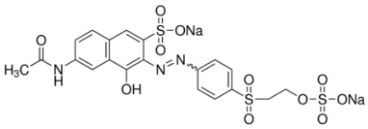
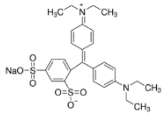
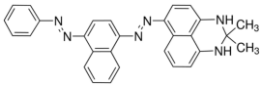
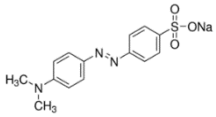
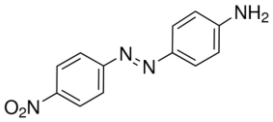
2.2.1 Chemicals

PASS ([η]=0.56) was synthesized by aromatic nucleophilic substitution at atmospheric pressure [125]. Deionized water was employed in the experiments. The other chemicals used in the experiments are listed in Table 2.4. Dyes were used as solutes and their specific properties are summarized in Table 2.5.

Table 2.4 Chemicals reagents

Chemicals	Chemical Formula	Purity (%)	Supplier
N-methyl-2-pyrrolidone (NMP)	C_5H_9NO	99	Sigma-Aldrich
Bulk Kevlar 69	$-(C_{14}H_{10}N_2O_2)-$	---	Thread Exchange (USA)
Potassium hydroxide	KOH	85	Sigma-Aldrich
Bovine serum albumin (BSA)	Globular proteins	99	Sigma-Aldrich
Dimethyl sulfoxide (DMSO)	C_2H_6OS	99.5	ACROS ORGANICS NV
Carbon tetrachloride	CCl_4	99.8	Sigma-Aldrich
Ethanol	C_2H_6O	99	Sigma-Aldrich
Methanol	CH_3OH	99.9	Sigma-Aldrich
Dimethylformamide (DMF)	C_3H_7NO	99.8	Sigma-Aldrich
Tetrahydrofuran (THF)	C_4H_8O	99.5	Sigma-Aldrich
Isopropanol (IPA)	C_3H_8O	99.5	Sigma-Aldrich
n-Heptane	C_7H_{16}	99	Sigma-Aldrich
Sulfuric acid	H_2SO_4	97~98	Sigma-Aldrich
Hydrogen peroxide	H_2O_2	30	Sigma-Aldrich
Acetic acid	CH_3COOH,	99	Sigma-Aldrich
Rose Bengal (RB)	$C_{20}H_2Cl_4I_4Na_2O_5$	90	Sigma-Aldrich
Reactive orange 16 (RO16)	$C_{20}H_{19}N_3O_{11}S_3$	70	Sigma-Aldrich
Disperse orange 3	$C_{12}H_{10}N_4O_2$	90	Sigma-Aldrich
Sudan black B (SBB)	$C_{29}H_{24}N_6$	High purity	Acros Organics.
Erythrosin B (EB)	$C_{20}H_6I_4Na_2O_5$	High purity	Acros Organics.
Eosin Y (EY)	$C_{20}H_6Br_4Na_2O_5$	High purity	Sigma-Aldrich
Patent Blue VF (PBVF)	$C_{54}H_{62}CaN_4O_{14}S_4$	50	Sigma-Aldrich
Methyl orange (MO)	$C_{14}H_{14}N_3NaO_3S$	High purity	Acros Organics.

Table 2.5 Characterizations of dyes used in this thesis

Dyes	MW[a] (g mol^{-1})	Chemical structure	λ^{b}mas (nm)
Rose Bengal	1018		549
Erythrosin B	836		533
Eosin Y	692		524
Reactive orange 16	618		494
Patent Blue VF	567		635
Sudan black B	457		598
Methyl orange	327		505
Disperse orange 3	242		443

a Molecular weight; b Maximum absorption wavelength

2.2.2 Filtration setup

Both the dead-end setup (Fig. 2.3) and high-pressure crossflow equipment (Fig. 2.4) were used to perform the organic solvent nanofiltration. The dead-end equipment consists of a dead-end filtration cell (Fig. 2.3a), a 3-way valve to be placed on the top of the filtration cell (Fig. 2.3b) and nitrogen gas supply (line, 50 bars max) with a pressure regulator (Fig.2.3 c).

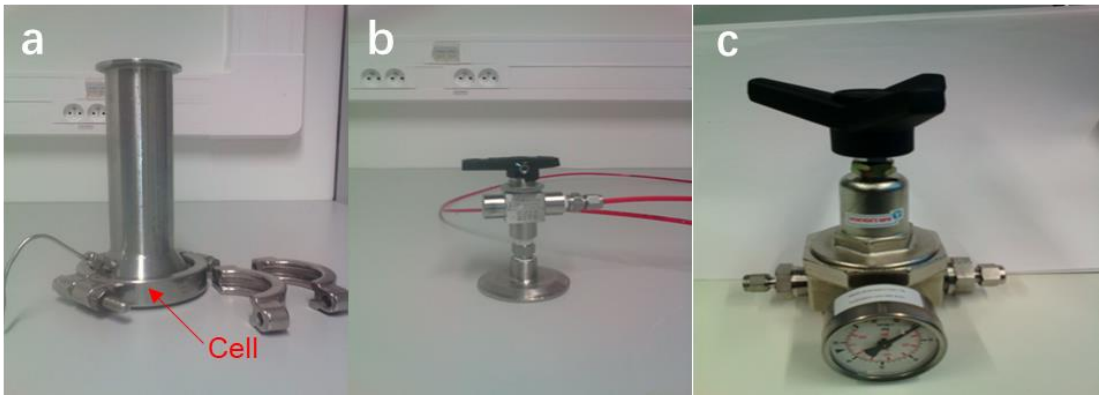


Fig. 2.3 Picture of dead-end equipment. a filtration cell; b 3-way valve; pressure regulator.

The high-pressure crossflow equipment was obtained from Evonik. For this equipment, the feed solution circulates in the system driven by a gear pump. The gas pressure is applied to create a high pressure in the system to conduct the separation. This device can test two membranes at the same time.

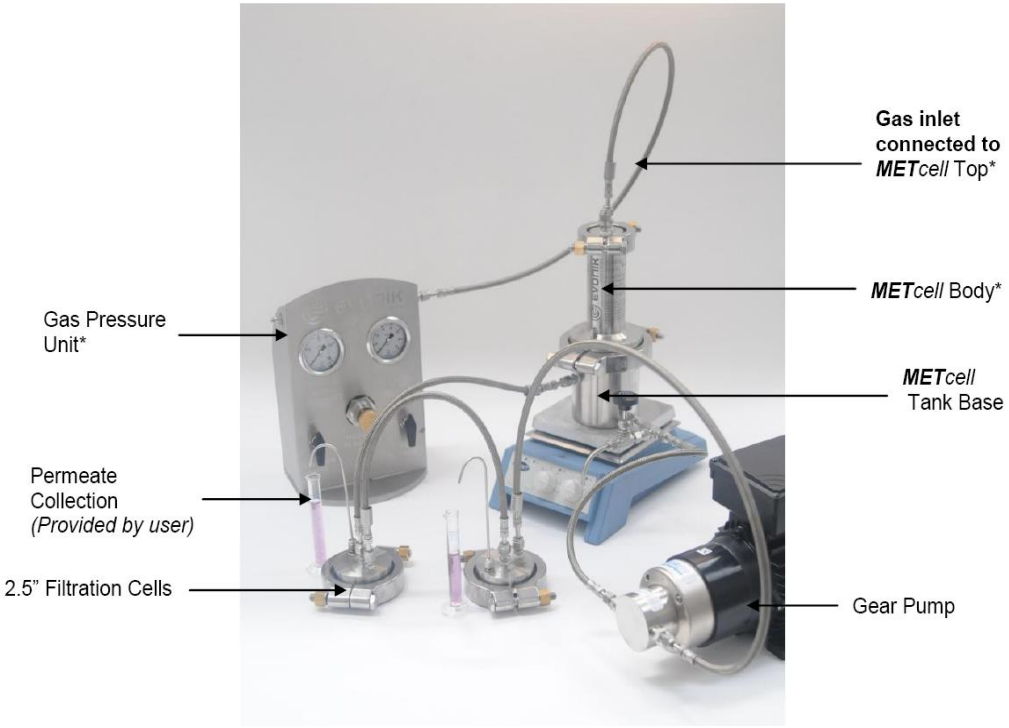


Fig. 2.4 Assembled METcell Cross-Flow system

2.2.2 Membrane fabrication

2.2.1.1 Preparation of PASS membranes

PASS membrane preparation: Before casting a PASS solution (20 wt%, 24 wt%) on a glass plate, the solution was degassed at room temperature. Subsequently, the glass plate with the polymer solution was immediately immersed in the pure water coagulation bath for phase separation. After the formation of PASS membranes, they were immersed in pure water to remove the residual NMP. The casting process was performed using a controllable casting machine. The casting knife thickness for the PASS solution casting is 150 μm. PASS membranes fabricated from 20 wt% PASS solutions were employed to investigate the influence of oxidation on the filtration and solvent resistant performance, because these membranes have a high water flux and lower rejection, which makes the effect of oxidation on the membrane performance more obvious, while PASS membranes used in organic solvent nanofiltration were fabricated from a PASS solution with a concentration of 24%.

Modification of PASS: The obtained PASS membranes were immersed in a solution with a composition of 91 vol% acetic acid, 3 vol% concentrated sulfuric acid (98%) and 3 vol% hydrogen peroxides (30%) for 12 hours at 25°C. Then, oxidized membranes were rinsed by deionized water to remove the residual chemicals before testing.

2.2.1.2 Preparation of Kevlar membranes

Preparation of aramid nanofibers: 2.0 g of bulk Kevlar 69 was dissolved in DMSO/water (40:1) with 2.0 g KOH to obtain a 2 wt% of Kevlar nanofiber solution by stirring for one week at room temperature until a dark red, viscous solution was formed. Then, this Kevlar dope solution was left for one month for the further splitting of the fibers into nanofibers. Kevlar solutions with concentration of 1.0 wt% and 1.5 wt% were obtained by diluting the 2 wt% of Kevlar solution with DMSO.

Preparation of a Kevlar *hydrogel membrane*: Kevlar nanofiber solutions were casted onto a glass plate by a casting knife with a certain gap at room temperature with a humidity of 50-60%. The glass plate with nanofiber solution was immediately immersed in deionized water bath to form a hydrogel membrane. Six different hydrogel

membranes fabricated from different concentrations with different thickness were synthesized. These membranes were named by the concentration and thickness as follows: M1%-200 M1.5%-200, M2%-200, M2%-100, M2%-60 and M2%-20. These obtained hydrogel membranes were submerged in water to remove the residual solvent.

Nanofibrous Kevlar membrane: The Kevlar OSN membranes were fabricated by the regeneration of hydrogen bonds induced by the evaporation of water between nanofibers during the thermal treatment of hydrogel membranes in an oven at 60 ºC for 12 h.

2.2.3 Membrane characterization

2.2.3.1 Fourier transform infrared spectroscopy (FT-IR)

The FT-IR spectrum of the PASS membrane acquired from a NEXUS670 FT-IR spectrometer was used to study the chemical changes of the oxidation reaction.

2.2.3.2 X-ray photoelectron spectroscopy (XPS)

XPS analysis was used to evaluate the element valence on the membrane surfaces. This was carried out on a Krais ULFRA^{DLD} spectrometer employing a Mono Al achromatic X-ray source operated at a total power of 160 W.

2.2.3.3 Scanning electron microscopy (SEM)

The surface and cross-sections morphology were visualized by SEM imaging via a Philips Scanning Electron Microscope XL30 FEG (Eindhoven, the Netherlands). The cross-section samples were prepared by mechanical fracturing of membranes in liquid nitrogen. Each sample was dried and sputter-coated with a thin layer of gold before testing. In order to preserve the macro-structure of Kevlar hydrogel membrane samples during the thermal treatment, supercritical CO_2 drying was applied.

2.2.3.4 Atomic force microscopy (AFM)

The surface roughness of the membranes was determined by using a Dimension 3100 AFM device (Bruker, USA) under ambient conditions and with a scanning area of 1×1 μm^2 and 5×5 μm^2. Tapping mode was applied using NCSHR probes (NanoAndMore GmbH, Germany) with a silicon tip having a radius of < 7 nm and a spring constant of 40-50 N m^{-1}. The membrane roughness values reported in this thesis were averaged from at least three different spots and expressed as root-mean-square roughness (R_{rms}); average roughness (R_a) and maximum vertical distance (R_m) between the highest and lowest points of the membrane surfaces were also investigated.

2.2.3.5 Contact angle

Contact angle measurements of a DI water droplet on the membrane surface were performed to observe the hydrophilicity changes of the membranes before and after modification via a contact angle goniometer (OCA20, Data physics Instruments, Germany). Before the test, PASS membranes were dried overnight at the oven at 60°C. The reported contact angle represents the average value of five measurements on each membrane.

2.2.3.6 Water content and swelling rate of Kevlar hydrogel membranes

The water content and water swelling ratio of these Kevlar membranes were measured by the mass of hydrogel membrane in wet state (m_{wet}) and in dry state (m_{dry}).

$$Water\ content = \frac{m_{wet} - m_{dry}}{m_{wet}} \quad (2.9)$$

$$Swelling\ ratio = \frac{m_{wet} - m_{dry}}{m_{dry}} \quad (2.10)$$

2.2.4 Solvent stability measurement

2.2.4.1 Solvent resistance of oxidized PASS membrane

In order to test the chemical stability of PASS membranes in organic solvents, PASS and O-PASS membranes were immersed in $CHCl_3$ and NMP, and 98% H_2SO_4 for 72 h,

respectively. Before immersing membranes in $CHCl_3$, O-PASS membranes were put in ethanol for 10 minutes to remove the water in membranes, and then the residual ethanol on membrane surface was wiped by tissue. For the NMP and 98% H_2SO_4, O-PASS membranes were directly immersed in these two solvents. After immersion in the solvent for 72 h, the $CHCl_3$ treated O-PASS membranes were washed with ethanol, and then washed with water. For the NMP, and 98% H_2SO_4 treated membranes, they were washed directly by water. Then all of the membranes were kept in water before the further characterization. The water flux and dye rejection of these solvent treated membranes were tested in a dead-end setup to observe whether the membranes were damaged by these solvents. In addition, microstructural changes of these membranes were visualized by the SEM images.

2.2.4.2 Solvent resistance of Kevlar membrane

Kevlar membranes M2%-200 were immersed a series of solvents including methanol, ethanol, IPA, hexane and CCl_4 for 7 day. After this, the Rose Bengal rejection of these membrane was measured. Through the change of rejections, the solvent stability can be demonstrated.

2.2.5 Organic solvent nanofiltration: permeation and rejection

2.2.5.1 Permeation and rejection

O-PASS membranes fabricated from a polymer solution of 24 wt% were applied in organic solvent nanofiltration. The solvent permeation and dye rejection of modified membranes were measured by using a stainless-steel dead-end apparatus (HP4750, Fig. 2.3) with an effective area of 13.2 cm^2. During the filtration measurement, the operating pressure and temperature were 6 bar and 25°C, and the feed solution was constantly stirred at 600 rpm to minimize concentration polarization. The permeation of the membrane was calculated by Eq. 2.6. Kevlar membrane was measured by high pressure crossflow equipment (Fig.2.4).

Dyes (Table 5) with molecular weight ranging from 242.23 g/mol to 1017.64 g/mol were selected as solutes for the rejection tests. All dye solutions had a 35 μM concentration. Dye rejections were calculated based on the concentration difference between the feed and the permeate. It was calculated by using Eq. 2.7.

2.2.5.2 Long term filtration experiment

To investigate the (relatively) long-time chemical stability of oxidized PASS membranes, the permeation of DMAC was studied for a duration of 30 h; the rose Bengal rejection was measured after one hour of filtration, and at the end of the 30 hours filtration test.

Chapter 3

Production of polyamide-12 membranes for microfiltration through selective laser sintering

Adapted form: Shushan Yuan, Dieter Strobbe, Jean-Pierre Kruth, Peter Van Puyvelde, Bart Van der Bruggen, Production of polyamide-12 membranes for microfiltration through selective laser sintering, Journal of Membrane Science, 525 (2017) 157-162.

3.1 Introduction

As reviewed in Chapter 1, section 1.1, the conventional membrane fabrication methods exhibit various disadvantages, such as water pollution by solvent, and surfers from the limit of controlling the structure of a membrane fabricated. Thus, there is still a long way to go to find a membrane fabrication process with a perfect control of the membrane structure, at low cost and without the extensive use of solvents. New manufacturing techniques developed in other fields may therefore be of interest for membranes.

Additive manufacturing (AM), popularly known as rapid prototyping or 3D printing, is defined as the group of techniques that uses layer-by-layer joining of materials to make parts from 3D model data [95-97]. The techniques make use of either extrusion, jetting, photo-curing, laminating or fusion of materials. Fused deposition modeling (FDM), stereolithography (SLA) and selective laser sintering (SLS) are the most important AM techniques for polymer processing [126, 127]. These technologies have the possibility to revolutionize the current membrane technology and can potentially reduce the energy consumption and solvent usage in the membrane fabrication process.

AM is gradually introduced in the field of membrane technology. As indicated in Chapter 1, section1.5.2, AM techniques have been applied in the fabrication of

membrane module, Polydimethylsiloxane (PDMS) membranes and thin film composite membranes [115-118] [119, 120]. However, to the best of our knowledge, SLS has not been investigated so far as a process to directly produce functioning membranes. Porosity of SLS parts resulting from incomplete powder coalescence reduces mechanical strength and performance. Most of the research in this field focusses on improving the sintering of powders and decrease the part porosity by a proper material selection, powder modification and by optimizing processing parameters [128-130]. However, this inherent porosity can be an advantage in membrane synthesis. In addition, this fabrication process will eliminate the high cost of solvent and membrane design and environmental issue caused by solvent. So, in this work, SLS is explored for the first time to make microfiltration membranes from polyamide-12 (PA) which is the most popular material for SLS and also an important polymeric membrane material.

3.2 Results and discussions

3.2.1 Membrane morphology, porosity and pore size distribution

Fig. 3.1 shows the surface structure of the SLS made membranes. From these images, it can be seen that membranes with different pore sizes were obtained. Laser power had a significant influence on the morphology of these membranes. In specific, with increasing laser power, membrane surfaces became denser, which could be concluded from the images of samples a1, a2, a3 and a4 or c1, c2, c3 and c4. When the laser power reached 20 W (samples a4 and c4), a lot of grooves could be spotted on the surface, probably caused by the overheating of polyamide. From the images of samples a1 and b1 or c1 and d1, it is found that the count of laser scanning also had obvious effects on membrane surface. Membranes synthesized by two counts have a denser surface structure than those made by one count. Hatch space was another parameter that influenced the energy input during the membrane fabrication process, but its influence was not as apparent as laser power and laser scanning count. From the images of samples a1 and c1, it can be seen that membranes made with a HS of 0.1 mm more or less showed a denser surface than those made with a HS of 0.15 mm. So, in general,

membranes fabricated with a higher laser power, smaller HS and 2 counts have a smaller pore size and denser structure than those fabricated with smaller laser power, larger HS and 1 count. At these processing parameters, more energy is absorbed by the polymer powders, leading to a better coalescence of polymer powders and a narrower gap between polymer powders.

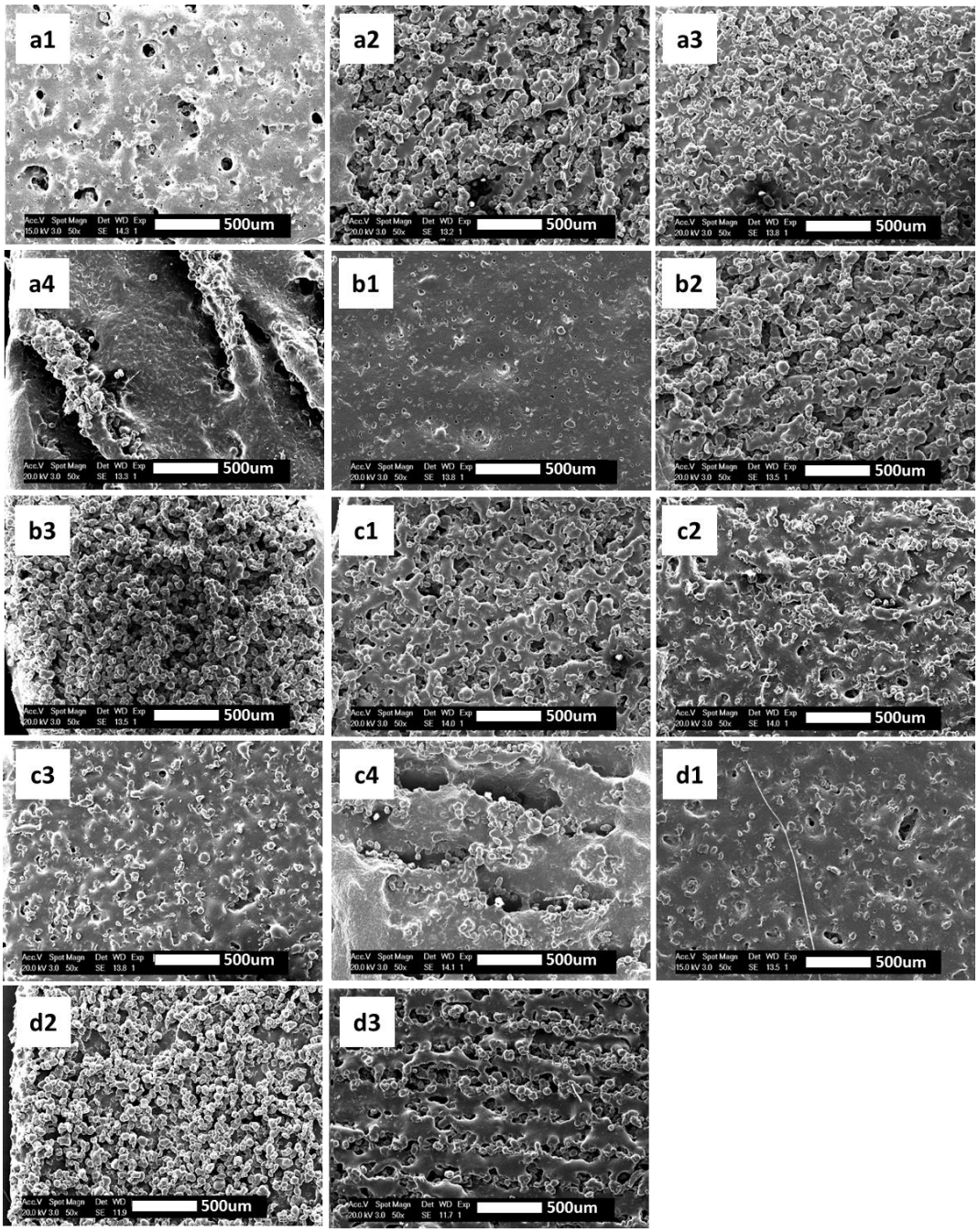


Fig. 3.1 Surface morphology of polyamide microfiltration membrane, magnification 50.

Fig. 3.2 shows the cross-section of membrane samples b1, b2 and b3. These pictures show that just like traditional membranes, SLS membranes also have a dense top layer, and a relatively porous sublayer. With increasing the distance from the top, the energy that the polymer powder absorbs decreases. This results in less melting, less coalescence and a more porous structure. In the end, the surface of the sublayer consists of partly molten and coalesced particles, which can be seen in the images of samples b1, b2 and b3 in Fig. 3.2. In addition, from these three images, the thickness of the membrane grows with the increase of laser power because the higher the laser power, the deeper the laser can reach into the polyamide powder.

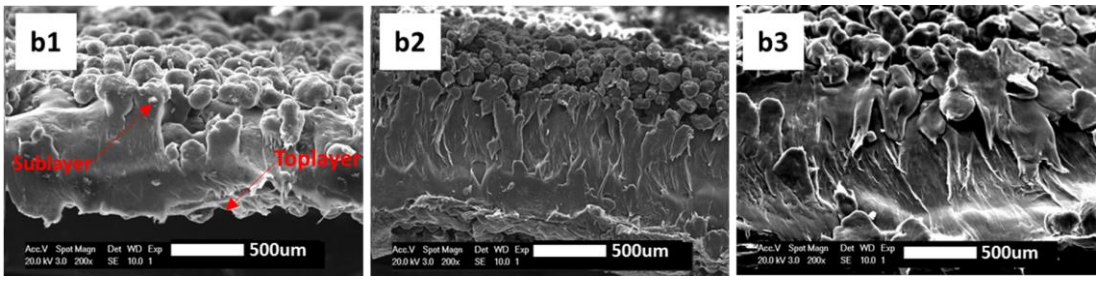


Fig. 3.2 cross-section morphology of polyamide microfiltration membrane, magnification 50.

The structural changes of membranes processed at different conditions were further confirmed by the porosity tests. In Fig. 3.3a, it is shown that with increasing laser power, increasing laser scanning counts and decreasing hatch space, the porosity of the membrane is decreased. The membrane with the highest porosity of 30.7% was made by using a laser power of 5 W, a hatch space of 0.15 and 1 scanning count (sample c1). Compared to traditional membranes made by nonsolvent-induced phase separation (NIPS), these membranes have a relative low porosity [131], mainly because the part between two neighboring pores are solid rather than porous.

The pore size distribution was obtained by POROLUX 1000. As an example, the results for samples d1 and d2 are shown in Fig. 3.3b. The mean pore size of these two samples is 14.5 μm and 9.8 μm, respectively. Sample d2, which was manufactured with a higher laser power, has a relatively narrower pore size distribution compared to

sample d1. The largest pore size of sample d1 goes up to 27 μm while it is 18 μm for sample d2. These differences were caused by the ED input during the processing.

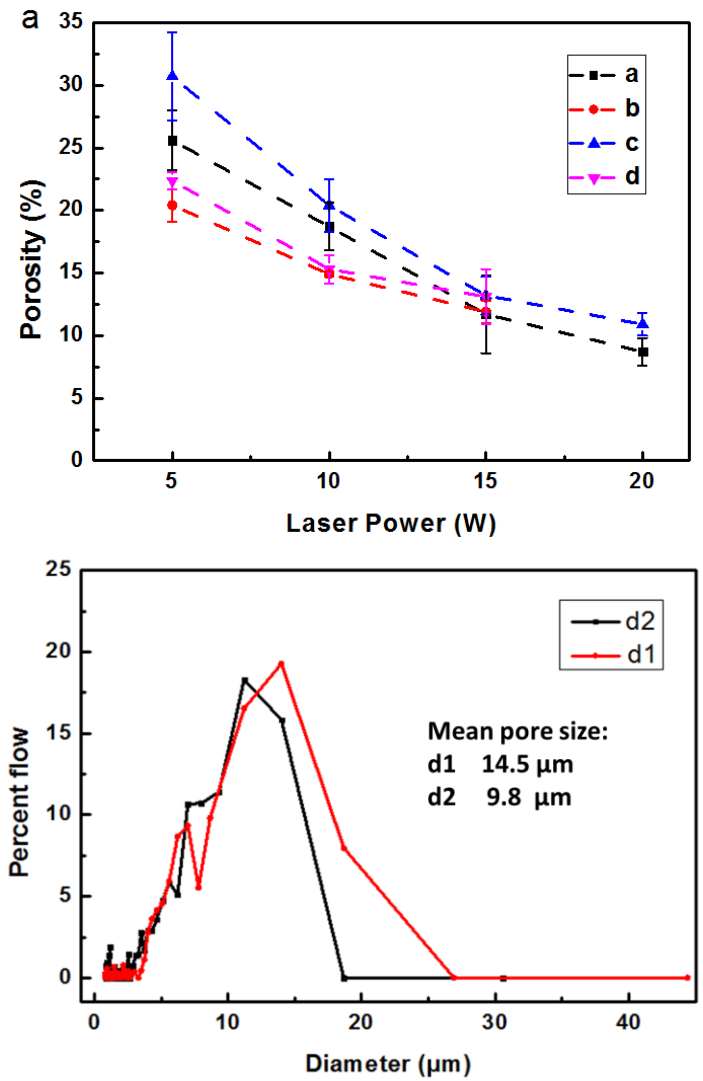


Fig. 3.3 a, the porosity of resultant membrane samples; b, the pore size distribution of membrane sample d1 and d2

3.2.2 Water permeance and rejection

The water permeance is greatly affected by the membrane structure and pore size, and it increases with the increase of porosity and pore size. It can be seen from Fig. 3.4 that membranes made with a higher laser power, lower hatch space and 2 counts have a smaller pure water permeance, which confirms the trend observed for pore size and membrane porosity as discussed above. Fig. 3.4 shows that with increasing laser power,

the water permeance decreases significantly. Generally, the lower hatch space of 0.1 mm also results in lower water permeance, compared to the hatch space of 0.15 mm. Increasing ED during processing, results in lower water permeance. This corresponds to the literature, where it was indeed suggested that material porosity decreases with increasing laser ED [132]. Fig. 3.4 also shows that repeated scanning results in a decrease in water permeance. However, when the ED is too high, the water permeance is zero. Compared to traditional microfiltration membranes, the SLS membranes have a relatively high water permeance [133].

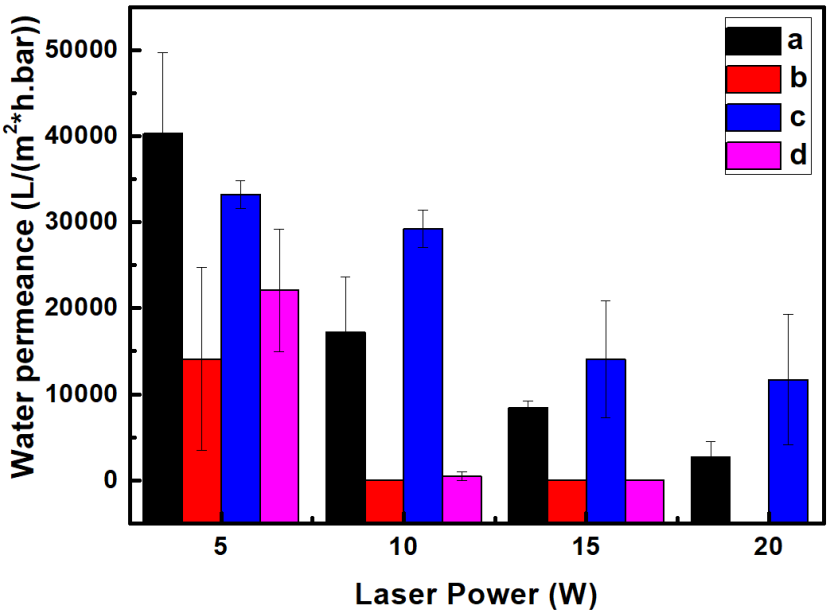


Fig. 3.4 Water permeance of membrane samples

A polystyrene latex solution was used to test the rejection of microfiltration membranes. Fig. 3.5 shows that with increasing ED or laser power, the rejection increases from 25.1% to 37.4% for hatch space 0.1 and from 21.7% to 36.3% for hatch space 0.15 mm, and then decreases to 32.6% and 35.8%, respectively. The increase of the rejection at the beginning was attributed to the denser layer created by the higher ED. However, when the ED is too high, the surface of the membrane becomes rough, which can be seen from the SEM image of membrane sample a4 and c4. In these two pictures, furrows and defects can be spotted.

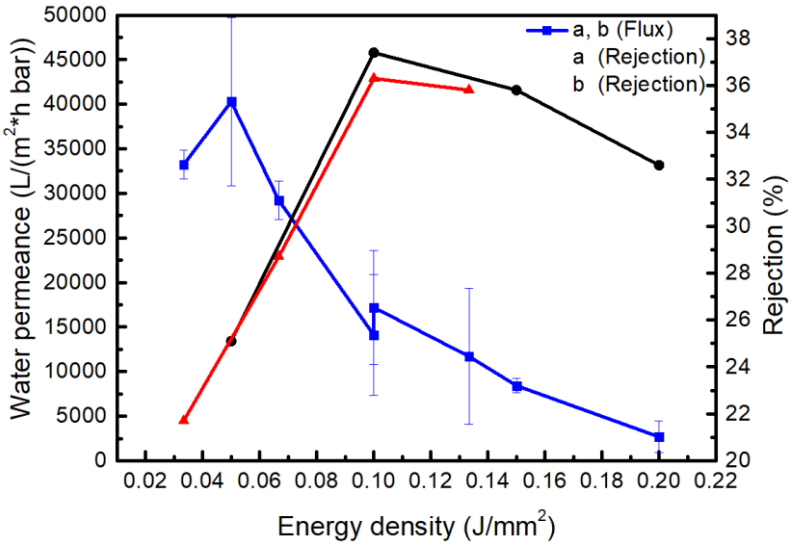


Fig. 3.5 The effect of ED on membrane rejection and water permeance

From the above experiments, it is obvious that the energy input greatly affects the performance of SLS made membranes. it can also be seen that with the increase of ED, the water permeance decreases dramatically. When the ED is 0.1 J/mm², the membrane has a good rejection. Below this value, a much more porous membrane structure is obtained due to the imperfect sintering of particles. For an ED higher than 0.1, a non-uniform or rough surface is obtained.

3.2.3 Mechanical strength

Microfiltration membranes are widely used as support to make ultrafiltration and nanofiltration membranes. Hence, as a support, the mechanical strength of the microfiltration membrane is of high importance during application. In Fig. 3.6, the tensile strength of the different membranes is shown. It can be seen the tensile strength of the sintered membranes ranged from 4.2 to 28 MPa. Most of the samples have a tensile strength over 10 MPa, which is significantly higher than most traditional membranes [134]. The latter is not surprising since the laser sintered membranes have a much lower porosity than traditional membranes made by NIPS. The tensile strength is greatly affected by the energy input. Membranes made with lower energy input have a higher porosity, hence much more defects which leads to a lower tensile strength.

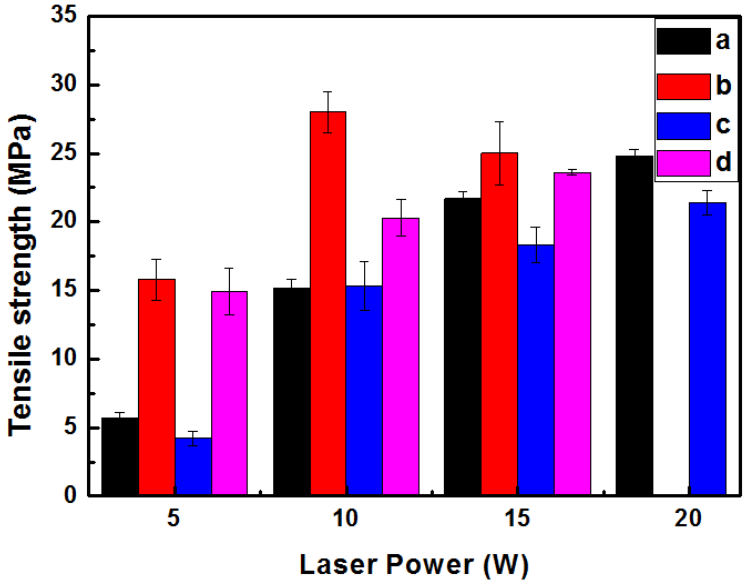


Fig. 3.6 The tensile strength of polyamide membranes

3.3 Conclusion and outlook

In this work, polyamide microfiltration membranes were fabricated by selective laser sintering for the first time. It was concluded that processing parameters have a great influence on the structure of the resulting membranes. A detailed investigation on laser power, hatch spacing and laser scan count demonstrated that the ED was directly linked to the membrane structure, pure water permeance and rejection. A membrane fabricated with processing parameters of higher ED, like a larger laser power, smaller hatch space and 2 counts, would have a denser membrane structure and a lower water permeance. For rejection, the ED of 0.1 J/mm² results in polyamide membranes with relatively high rejection. These results allow to optimize the membrane performance in future work by adjusting the size of polymeric particles and the size distribution. The approach may also be extended from polyamide to other polymers, and from experimental production to small batch production.

Chapter 4

Super-hydrophobic 3D printed polysulfone membrane with a switchable wettability by self-assembled candle soot for efficient gravity-driven oil/water separation

Adapted from: Shushan Yuan, Dieter Strobbe, Jean-Pierre Kruth, Peter Van Puyvelde, Bart Van der Bruggen, Super-hydrophobic 3D printed polysulfone membranes with a switchable wettability by self-assembled candle soot for efficient gravity-driven oil/water separation, Journal of Materials Chemistry A, (2017)25401-25409.

4.1 Introduction

Oil/ water separation has become a worldwide issue in the chemical industry and in environmental protection, because of the increasing pressure on industrial oily wastewater and frequent oil spill accidents [135-137]. Many porous materials, including mesh-based materials, fabrics, sponge-based materials, foam-based materials and membranes, have been developed to be applied in oil/water separation [138]. Among these, membranes were found to have a very high separation efficiency in oil/water separation [139-141]. However, the traditional membrane fabrication methods, like nonsolvent-induced phase separation (NIPS), thermally induced phase separation (TIPS) and vapor induced separation, consume a large amount of solvent, resulting in a large waste stream, leading to air and water pollution [20, 131]. Besides, the shapes of membranes synthesized by these methods are difficult to be designed freely according to the various oil/water separation modules. Therefore, solvent free membrane fabrication with the ability to control the membrane structure and pore size is urgently needed.

As mentioned in Chapter 1, Section 1.5, additive manufacturing methods are

promising for the fabrication of objects with complicated structure, and to produce an assembly in a single-step process compared to the traditional manufacturing [120]. This solvent free method could possibly revolutionize the current synthesis of porous membranes, and allow to fabricate an oil/water separation porous membrane according to the different shapes of membrane modules with reduced energy consumption and usage of chemicals. It is even possible to fabricate an oil/water separation module with a microfiltration membrane inside in a single-step process. However, although 3D printing technology has been applied to fabricate membrane modules and membrane spacers [120, 142, 143], only limited studies have focused on the fabrication of a porous membrane by 3D printing. In the Chapter 2, a 3D printed microfiltration membrane was developed by selective laser sintering of semi-crystalline polyamide. The processing parameters of selective laser sintering have a great effect on the structure and performance of the prepared membranes. This chapter showed a successful membrane fabrication by 3D printing. However, to fully explore the possibility of 3D printing in porous membrane fabrication, much more efforts should be made in this field. Selective laser sintering as 3D printing technique has a resolution range in the micrometer scale, so that membranes fabricated by this method tend to have pore sizes in the micrometer scale, which is suitable to be used in oil/water separation application. To the best of our knowledge, membrane fabrication by selective laser sintering for the oil/water separation has not been studied yet.

Apart from the porosity, the surface wettability of a membrane surface plays a critical role on the separation speed and efficiency of oil/water mixture. The ideal oil removing materials shows super-hydrophobic and super-oleophilic properties, which makes the oil phase spread easily and penetrate through the membrane while the water phase is repelled, separating the oil from the oil and water mixture [144, 145]. Inspired by a special wettable material discovered by Jiang et al. in 2004 [146], many methods have been reported to make membrane

surfaces super-hydrophobic, such as plasma treatment [147], surface grafting [148] and nanoparticle deposition [149-152]. The deposition of hydrophobic nanoparticles on the membrane surface is the most common way in the hydrophobic modification of a membrane surface [153]. Ding et al. reported a waterproof membrane fabricated by blade coating of SiO_2 nanoparticles onto an amino-silicone oil coated electrospun polyacrylonitrile membrane [154]. Using the same nanoparticles, a super-hydrophobic surface was fabricated by spraying polystyrene/SiO_2 core/shell nanoparticles [155]. Recently, candle soot, which is generated from incomplete combustion of candles, has attracted much attention in the fabrication of super-hydrophobic surfaces because of its hydrophobic properties, cost-effectiveness and production scalability. Several studies reported its application in oil/water separation. Li and co-workers fabricated a super-hydrophobic metal mesh through the deposition of candle soot on a metal mesh surface by putting the mesh on the flame of a candle [121]. However, with this method, it was difficult to deposit candle soot on polymeric porous materials because of the high temperature in the candle flame. To solve this, researchers coated the candle soot by spraying the candle soot/acetone solution on the surface of the material [156]. Nevertheless, spraying is difficult or impossible to be achieved on internal surfaces of porous materials. Therefore, it is important to develop a more efficient and general method for the coating of candle soot to enlarge the application of candle soot on other materials.

In this chapter, the fabrication of a super-hydrophobic 3D printed polysulfone (PSU) membrane with switchable wettability by the self-assembly of candle soot on its surface is reported. Specifically, amorphous PSU was used to fabricate 3D printed membranes because of its excellent thermal and chemical resistance. The optimal 3D printed PSU membrane was fabricated by varying processing parameters of the selective laser sintering process. The effect of processing parameters on the structure and performance of the PSU membrane was studied. In order to obtain a super-hydrophobic surface, the hydrophobic candle soot was

coated on the rough PSU membrane surface by a simple immersion in hexane. The optimal candle soot coated 3D printed membrane was employed to perform the oil/water separation.

4.2 Results and discussion

4.2.1 Morphology of 3D printed PSU membranes

The top surface, bottom surface and cross-section morphology of 3D printed PSU membranes were analyzed by SEM. As shown in Fig. 4.1, the membranes fabricated by selective laser sintering consist of a top dense sintered layer and a porous sublayer composed of not fully sintered PSU powders. The top surface morphology and membrane cross-section structure of these membranes were greatly altered by varying the processing parameters. More specifically, when the scanning count of M1 and M3 increased from 1 to 2, the number of pores on top surface was reduced, the surface became smoother and the thickness of the top layer increased from 137 μm to 201 μm and from 296 μm to 355 μm, respectively, which was attributed to the improved coalescence of PSU powder by the second laser scanning. Compared to the scanning count, hatch space played a much more important role in the formation of membrane pores. As shown in the SEM images of M1 and M3, when the hatch space was narrowed from 1.5 mm to 0.8 mm, the number of membrane pores was reduced dramatically, and the thickness of the membrane top layer was increased greatly by 116% from 137 μm to 296 μm, indicating that a higher energy input in the laser scanning could lead to a better PSU powder coalescence and a deeper melting of PSU powers in the powder bed. However, although scanning count and hatch space resulted in a decreased number of pores on the surface, the size of the large pores was not greatly changed, which was mainly due to the fixed size of the PSU powder. Besides, the morphology of the bottom surface was also not influenced by these two processing parameters. When the laser was working, the deeper in the powder

bed, the less energy had the laser. Therefore, the energy in the laser at the bottom surface had the lowest energy that can soften the PSU particles and make them merge, which means that the bottom surface of all the PSU membranes was formed by the same amount of energy, thus resulting in the same bottom surface morphology for PSU membranes fabricated with different parameters.

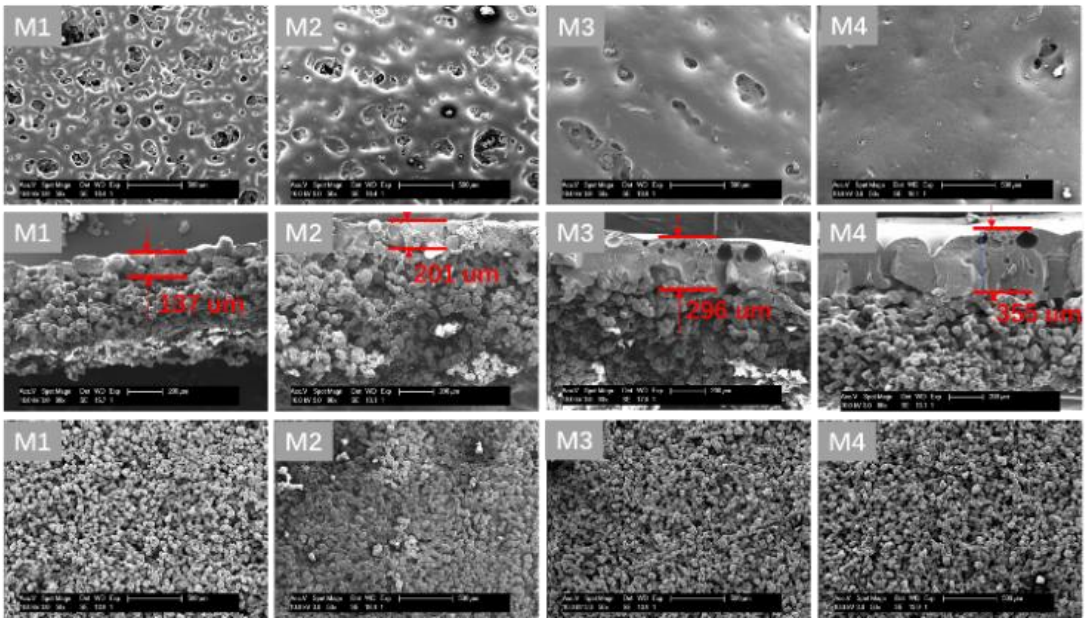


Fig. 4.1 SEM top surface, cross-section and bottom surface morphology of 3D printed PSU membranes (M1, M2, M3 and M4).

4.2.2 Performance of 3D printed PSU membranes

The performance and physical properties of 3D printed PSU membranes are shown in Fig. 4.2. The pore size of a membrane is a key factor that defines its application. Therefore, the pore size of M1 was analyzed. The pore size distribution is displayed in Fig. 4.2a. M1 has a pore size distribution ranging from 12 μm to 114 μm and an average pore size of 51.8 μm which is similar to the size of PSU particles. As to a membrane fabricated by selective laser sintering, pores were created by the incomplete coalescence between polymer particles. Hence, the better the coalescence of polymer particles, the denser a membrane can be created. Compared to the 3D printed polyamide-12 membranes [157], PSU 3D

printed membranes fabricated in this chapter had a larger pore size than that of 3D printed polyamide-12 membranes although these membranes were fabricated under similar processing parameters by using polymer particles with similar size. This is because the viscosity of the soft amorphous PSU particles is larger than that of molten semi-crystalline polyamide-12 particles, leading to a worse coalescence and larger voids.

The water filtration results of these 3D printed membranes are shown in Fig. 4. 2b. It was found that the water permeability decreased greatly with the decrease of hatch space and increase of scanning count. When the hatch space and laser scanning count were 1.5 mm and 1, the PSU membranes exhibited the largest water permeability of 24600 L/(m^2.h.bar), while the M4 membrane fabricated with a hatch space of 0.8 mm and 2 counts had a low water permeability of 4800 L/(m^2.h.bar) which was 19% of M1. Besides, the gravity driven water flux had a similar trend to the water permeability. However, the flux change between membranes was more dramatical. For example, M1 had a gravity driven flux of 16200 L/(m^2.h.bar) which is around 67 times that of M4. These significant changes were mainly attributed to the membrane structure, including pore numbers, pore size and the overall porosity of membranes, which contributed significantly to the water permeability and flux. The overall porosity of these membranes is presented in Fig. 4.2c. By decreasing the hatch space and increasing laser scanning count, the PSU membranes showed a less porous structure, i.e., the membranes became denser. This result was consistent with the cross-section morphology of these membranes in Fig. 4.1. Although the water permeability and gravity driven flux had a direct relation to the membrane structure, the original reason for the change of the permeability and flux were the membrane fabrication parameters, like hatch space and laser scanning count.

In a separation process, the membrane is exposed to mechanical stress and works under pressure. Accordingly, an adequate mechanical strength is an important

property for a membrane. The mechanical strength of these 3D printed PSU membranes was measured by a Mini-Tensile setup. As presented in Fig. 4.2c, by decreasing the hatch space and increasing laser scanning count, the tensile strength of the PSU membrane was greatly enhanced by 3.3 times from 5.2 MPa to 17.3 MPa, showing an opposite trend to the membrane porosity. The porous structure of a membrane can be regarded as mechanical defects in a polymer film. A membrane with higher porosity has more mechanical defects, leading to a weaker tensile strength [158].

The wettability of the top surface and bottom surface of the PSU membrane is reflected by the water contact angle results in Fig. 4.2d. The contact angle of the top surface of the 3D printed membrane showed a decrease from 89°to 71° with decreasing the hatch space and increasing laser scanning count, indicating an improved hydrophilicity of these membranes. On the contrary, the contact angle of the bottom surface remained constant at around 124°, implying a hydrophobic bottom surface. Interestingly, although the surface chemistry on both surfaces is the same, the water contact angle of the bottom surface was much larger than that of top surface. The Wenzel model and the Cassie-Baxter model are commonly used to describe the wettability of a surface. The Wenzel model was mainly used to describe the homogeneous wetting regime [159].

$$\cos(\theta) = r\cos(\theta_0) \qquad (4.1)$$

in which θ, θ_0 are the contact angle of a rough and smooth surface. r is the roughness factor which is defined as the ratio of actual surface area to the projected surface area.

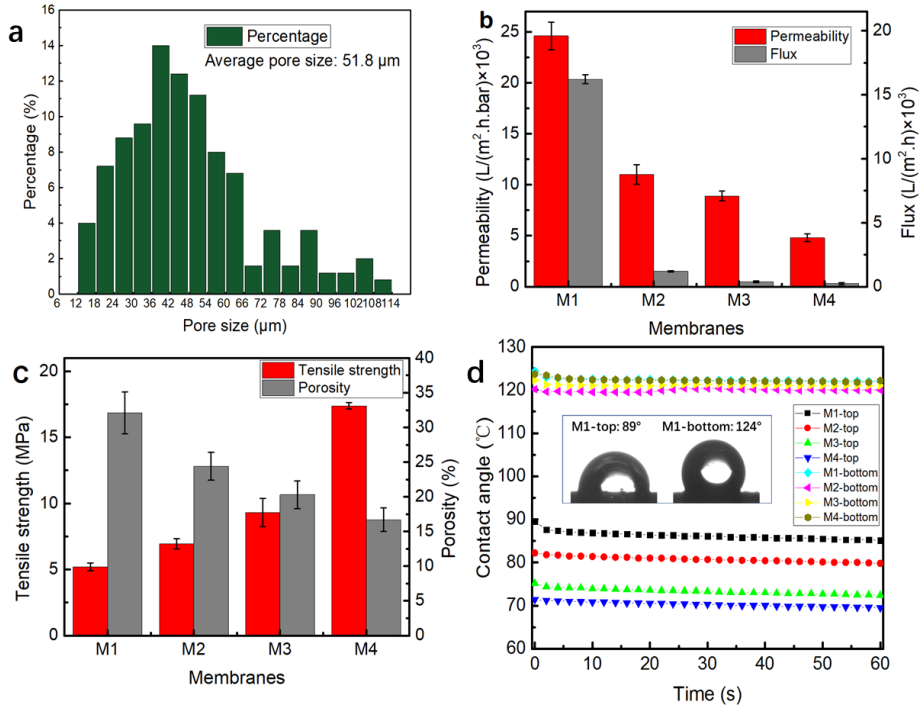


Fig. 4.2 The performance and physical properties of 3D printed PSU membranes. (a) the pore size distribution of M1; The water permeability and gravity driven flux (b), mechanical strength and porosity (c), and water contact angle (d) of prepared 3D printed PSU membranes.

According to the Wenzel model, the wettability of a smooth surface (when r is 1) is mainly determined by the chemistry of the materials itself, while the roughness factors amplifies the natural wettability of the surface, which means that a hydrophobic surface becomes more hydrophobic and a hydrophilic surface become more hydrophilic when micro-structured. However, when γ increases to a critical level, the liquid cannot penetrate into the surface cavities, leading to the formation of air pockets between liquid and solid surface. The formed solid-liquid-air heterogeneous interface dramatically decreases the contact angle hysteresis and improves the contact angle [160]. On basis of this, the Cassie-Baxter model [161] was proposed as follows:

$$\cos(\theta) = rf\cos(\theta_0) + f - 1 \qquad (4.2)$$

where f is the fraction of solid surface area wet by the liquid.

As shown in the scheme in Fig. 4.3, both the top surface and bottom surface were generated by the coalescence of PSU particles. However, since the bottom surface has a farther distance to the laser compared to the top surface, most energy in the laser was absorbed by the surface layer, resulting in a relatively smooth top surface composed by well coalesced PSU particles and a roughness bottom layer consisted of incomplete coalesced PSU particles in microscale scale. When a drop of water fell on this roughness surface, air was trapped in the surface cavities, creating a macroscale solid-water-air interface and an improved water contact angle. Based on these two models, it can be concluded that increasing the hydrophobicity of the material itself and the surface roughness of a surface are the two main methods to fabricate a super-hydrophobic surface.

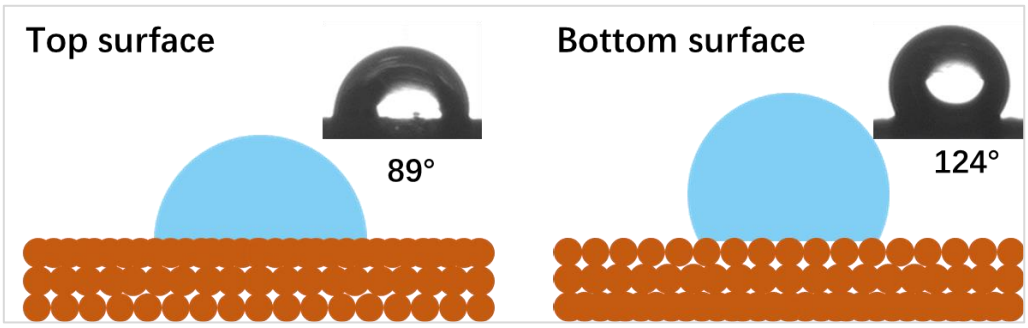


Fig. 4.3 Scheme of water contact angle on bottom and top surface

4.2.3 Coating of candle soot on PSU membrane surface

As the M1 membrane exhibits a better performance, including a larger water permeability and gravity driven water flux, as well as a higher porosity compared to the other 3D printed PSU membranes, it was chosen as the membrane to perform the super-hydrophobic modification. In addition, unlike the traditional membranes fabricated by phase inversion, the bottom layer rather than the top layer of M1 acts as the separating layer in the water and oil separation process because of the high roughness of the surface.

In order to find the optimal time for the modification of 3D printed membranes, the effect of immersion time on the membrane performance was investigated. Candle soot particles in nanoscale, which can be seen in Fig. 4.4a, were used to modify the 3D printed PSU membranes. Eight candle soot coated PSU membrane samples were prepared by immersing them in candle soot/hexane solution for 4 mins, 8 mins, 12 mins, 16 mins, 20 mins, 24 mins, 28 mins and 40 mins respectively under sonication. The surface morphology of unmodified and candle soot coated PSU membranes is shown in Fig. 4.4. It can be seen that the pristine PSU membrane showed a very smooth surface without any candle soot. On the contrary, after modification, a large amount of candle soot particles was deposited on the membrane surface, creating a rough membrane surface. Moreover, with increasing the immersion time, the amount of candle soot particles on the membrane surface was increased dramatically. More specifically, after 20 mins immersion in candle soot/hexane mixture, the PSU membrane surface was completely covered by the candle soot particles. Further extending the immersion time enhanced the coating of candle soot on the PSU membrane surface, leading to a thicker layer of candle soot on the membrane surface. When the immersion time increased to 28 minutes, an interesting loose network was formed on the membrane surface, which can be seen in a magnified SEM image in Fig. 4.4b. The 2D and 3D morphology of this candle soot coated surface with loose network structure is also shown in Fig. 4.5. According to the sectional analysis of the height in AFM graph in Fig. 4.6, the hole depth of the loose network structure is around 0.8 μm. This loose network structure endows the membrane with an average roughness 0.135 μm and a maximum vertical roughness of 1.04 μm. This well-arranged loose network was formed by the self-assembly of candle soot during the hexane evaporation process. When the 3D printed PSU membranes were taken out from the immersion solution, they were covered by a layer of candle soot/hexane solution. After they were placed in the oven, with the evaporation of the hexane, the concentration of candle soot in

candle soot/hexane layer was greatly increased, inducing the aggregation and self-assembly of candle soot particles into a loose network structure to lower their free energy. This nanoparticles self-assembling phenomenon during solvent evaporation was also observed and studied by other researchers [162, 163]. Murphy and co-workers reported the self-assembly of cetyltrimethylammonium bromide-coated gold particles into various shapes patterns during solvent evaporation [163].

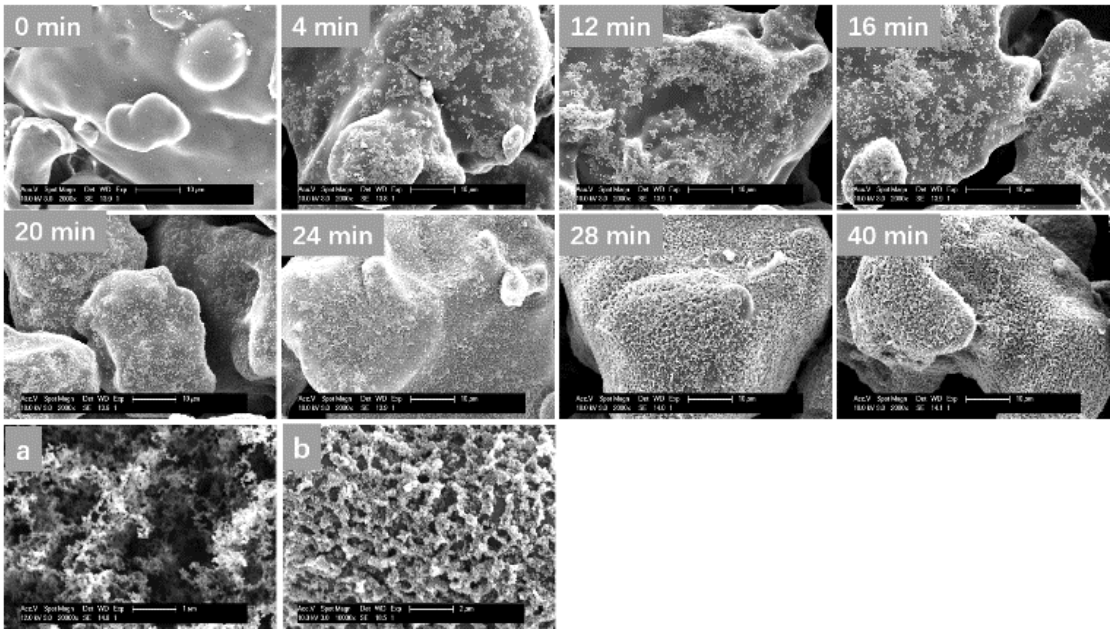


Fig. 4.4 Bottom surface morphology of candle soot coated 3D printed PSU membranes prepared with different immersion times; (a), SEM image of candle soot particles; (b) magnified image of the loose network on the membrane surface.

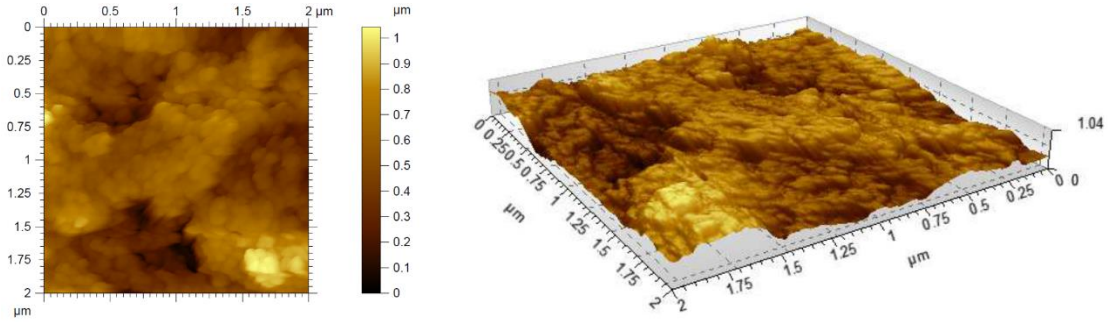


Fig. 4.5 2D and 3D surface morphology of the candle soot coated PSU membrane.

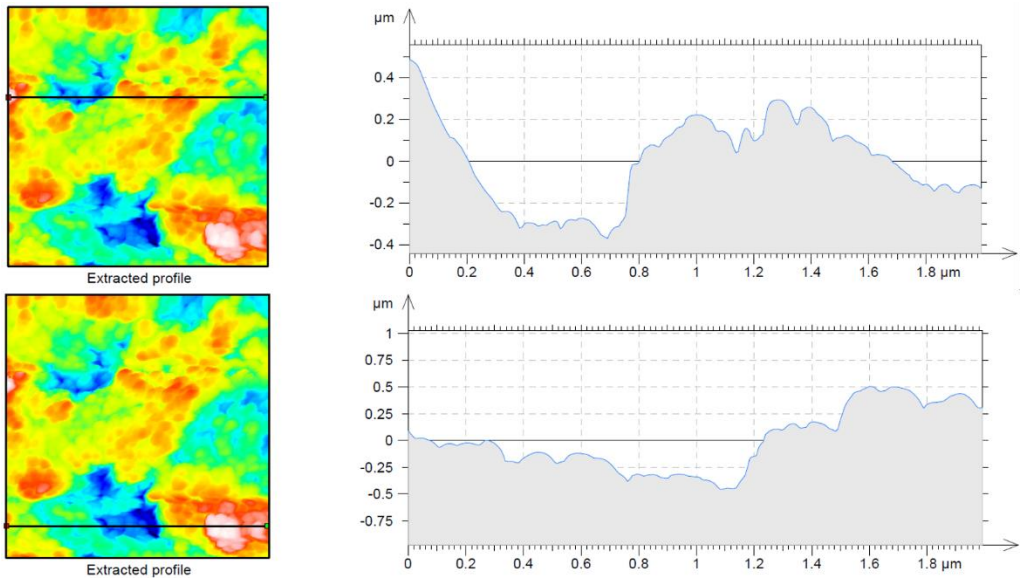


Fig. 4.6 Sectional analysis of the height along the line in the lift AFM graph.

The exact amount of candle soot particles deposited on the PSU membrane surface was calculated based on the mass of 8 membrane samples modified before and after. As shown in Fig. 4.7a, the amount of deposited candle soot particles on the membrane surface was greatly increased from 0 to 7.5 mg/g when the immersion time was increased from 0 to 28 mins, indicating a fast absorption of candle soot particles on the surface. Further extending the immersion time to 40 min could not make a significant difference, because the candle soot absorption was close to saturation of the adsorption capacity when the immersion time was 28 mins.

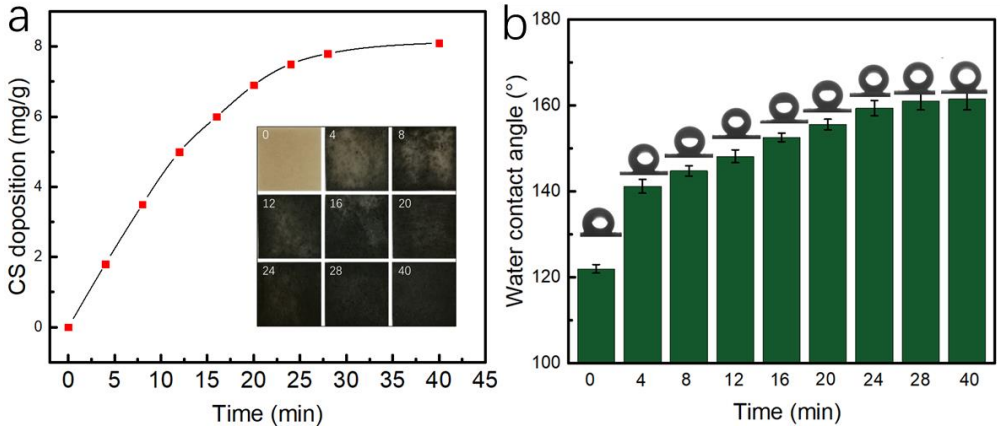


Fig. 4. 7 Water contact angle (a) and amount of candle soot particles deposited (b) on modified PSU membranes with different immersion time.

The hydrophobicity of these membrane samples was investigated by the water contact angle, as shown in Fig. 4.7b. The water contact angle showed a similar trend to the amount of candle soot particles coated on PSU membrane in Fig. 4.7a. When the PSU membrane was immersed in a candle soot/hexane solution for only 4 mins, the water contact angle of this membrane was dramatically increased to 141°, proving that candle soot had a substantial enhancement to the membrane surface hydrophobicity. Furthermore, when the immersion time increased to over 20 mins, these as prepared membranes exhibited a super-hydrophobic surface with a contact angle over 155°.

The obtained super-hydrophobic property of PSU membranes was mainly attributed to two factors, the hydrophobic nature of the surface imparted from the candle soot and the large roughness factor obtained by the loose network structure. Because of this network structure, when a drop of water contacts with the PSU membrane surface, air in the hole of the network would be trapped in the interface as shown in the Fig. 4.8, resulting in a nanoscale solid-water-air interface and a super-hydrophobic surface.

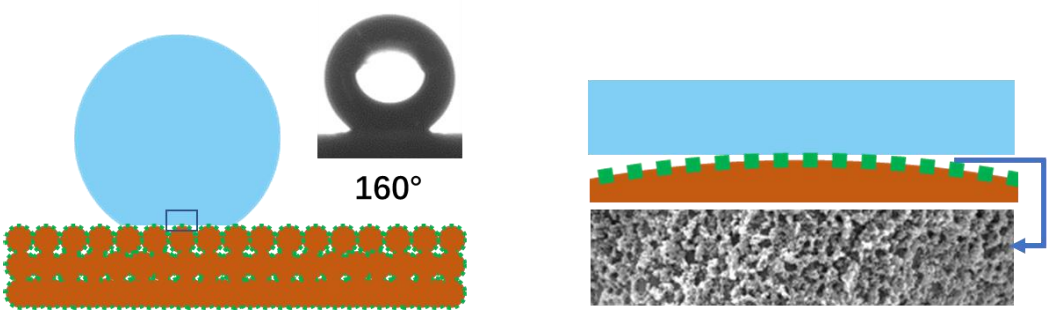


Fig. 4.8 Schematic representation of water contact angle on candle soot coated PSU membrane.

Taking all these analyses, including the SEM, contact angle and candle soot particle deposition, into consideration, an immersion time of around half an hour was found optimal to fabricate super-hydrophobic 3D printed membranes.

4.2.4 Super-hydrophobicity, super-oleophilicity and stability of 3D printed PSU membrane

The prepared 3D printed PSU membrane showed not only super-hydrophobic properties with a water contact angle as high as 161° and a sliding angle of 5° (Fig. 4.9a), but also super-oleophilicity. As presented in Fig. 4.9b, when an oil drop contacted the membrane, it spread along the surface and permeated in the membrane within 1.5s, implying a super-oleophilic surface.

The super-oleophilicity and super-hydrophobicity of the PSU membranes greatly depended on the candle soot and the loose network structure. Therefore, the stability of the loose network on membrane was critical to its long-term performance. Furthermore, the detachment of candle soot from membrane during separation could contaminate the feed and permeate solution. Hence, the stability of the loose network was evaluated by immersing the membrane in hexane under sonication for 30 mins. The images of the hexane before and after sonication are shown in Fig. 4.9c. The color of the hexane was not changed to black after the treatment, indicating that the candle soot was firmly attached on the membrane

surface and difficult to detach from the membrane. The loose network structure could also keep its structure after sonication, which was confirmed by the SEM image in Fig. 4.9f.

The chemical stability of the candle soot coated 3D PSU printing membrane in 1 M HCl, 1 M NaOH, 1 M NaCl and hot water was assessed by immersing in these liquids for 12 hours. Subsequently, membranes were washed with water and dried. The contact angle of these membranes was measured. As shown in Fig. 4.9d, the water droplets on the candle soot coated PSU membranes exhibited a stable super-hydrophobicity with a contact angle still above 155° after being immersed in corresponding corrosive solutions for 12 h, demonstrating that candle soot particles and PSU 3D printed membranes were chemical stable in these harsh environments. In addition, the candle soot coated PSU membranes were not only stable in these solutions, but also showed a super-hydrophobic property toward the droplets of these solutions. As shown in Fig. 4.9e, these droplets exhibited perfect spherical shapes on the PSU membranes.

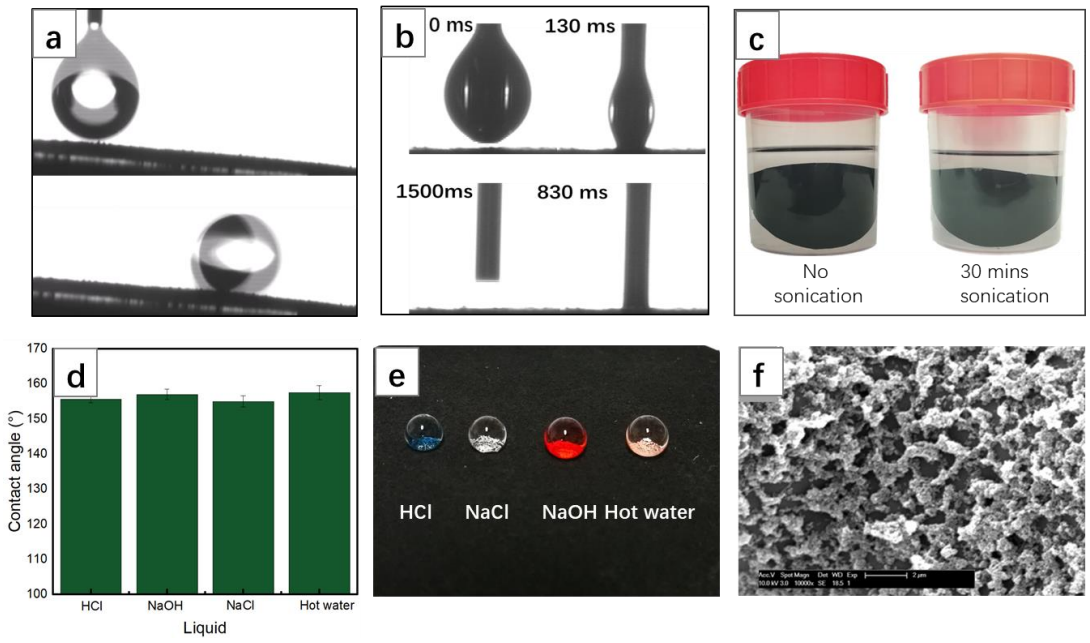


Fig. 4.9 (a) Water SA angle images of PSU membrane; (b) oil CA images of PSU membrane; (c) photographs of the candle soot coated PSU membrane in hexane before and after a sonication of 30 mins; (d) the water CA of PSU membranes treated by 1 M HCl, 1 M NaOH, 1 M NaCl and hot water for 12 hours; (e) photographs of 1 M HCl, 1 M NaOH, 1 M NaCl and hot water drops on the PSU membrane; (f) loose network structure of candle soot coated PSU membrane after 30 mins of sonication.

From what has been discussed above, it was concluded that the candle soot coated 3D printed PSU membranes exhibited super-hydrophobic and super-oleophilic properties and a strong mechanical stability under sonication and high chemical stability in 1 M HCl, 1 M NaOH, 1 M NaCl and hot water. Besides, the tensile strength of PSU membrane after these stability tests was not affected (Fig. 4.10). This is mainly because the bulk mechanical strength of the membrane is determined by the polysulfone, which has good chemical resistance and mechanical properties.

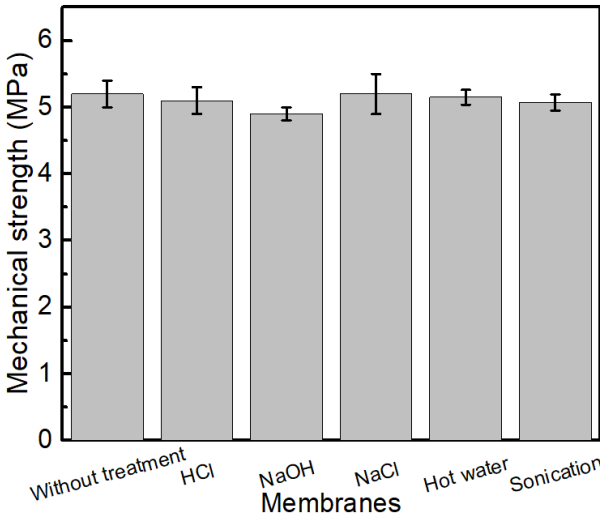


Fig. 4.10 Mechanical strength of the membranes after the stability test (immersion in 1 M HCl, 1 M NaOH, 1 M NaCl and hot water; sonication for 30 minutes).

4.2.5 Oil/water separation

The separation of oil/water mixtures was performed as shown in Fig. 4.11a. It can be seen that the red water was retained above the membrane while the oil quickly permeated through it and dropped in a plastic container, suggesting that the oil was successfully separated from the oil/water mixtures by the candle soot PSU membrane. When the oil/water mixtures touched the hydrophobic surface, the water was repelled while the oil spread and permeated into the loose network. In the end, all of the holes in loose network would be fully filled with oil, creating a candle soot/oil layer on the PSU membrane surface. This self-formed candle soot/oil layer would enhance the water repellent properties of the membrane and maintain the separation of oil from the oil/water mixtures until the end.

A variety of oil/water mixtures have been successfully separated, such as hexane, petroleum ether, heptane and mineral oil. In order to evaluate the performance of the prepared membrane in oil/water separation, the separation efficiency and gravity driven flux of different oil were measured. As shown in Fig. 4.11b, a gravity driven flux of around 19000 L/(m^2.h) and a separation efficiency over 99% were obtained for all of these oils.

As mentioned above, this super-hydrophobic and super-oleophilic candle soot coated surface provided the selectivity of oil from oil/water mixtures at the beginning of oil/water separation, afterwards, the oil/water separation was maintained by the self-formed candle soot/oil layer. In this case, if an artificial candle soot/water layer could be obtained by the filling of water in the loose network structure, this membrane could be used for the separation of water from oil/water mixtures. Therefore, the dry super-hydrophobic PSU membrane was first immersed in ethanol; then, it was immersed in water. After this solvent exchange process, an artificial candle soot/water layer on the PSU membrane was obtained. This PSU membrane was used for the separation of water from the oil/water mixture.

As can be seen in Fig. 4.11c, the water (marked by red dye) was successfully separated from the oil/water mixtures by the water prewetted membrane. When the oil/water mixtures dropped on the surface of this membrane, the oil was repelled by the water filled loose network layer because of the immiscibility between oil and water, while the water merged into the water layer. Therefore, this membrane showed a switchable wettability from super-hydrophobicity to super-oleophobicity after being prewetted with water as shown in Fig. 4.11e.

The switchable wettability was further measured by 10 cycles of hexane/water separation. In each cycle, the dry membrane was firstly used for separation of hexane from a hexane/water mixture. Then, it was dried in an oven to evaporate the hexane on its surface. Afterwards, the membrane was rinsed sequentially by ethanol and water to be prewetted by water. Then, it was employed to conduct a separation of water from hexane/water mixtures. After the separation, the membrane was dried for the next cycle. The separation efficiency of water and hexane in each cycle was measured. As shown in Fig. 4.11d, both water and hexane separation efficiency were over 99%. After 10 cycles of hexane/water separation, the separation efficiency was still higher than 99%, indicating a high

oil/water separation stability of dry candle soot coated PSU membrane and water prewetted candle soot coated PSU membrane.

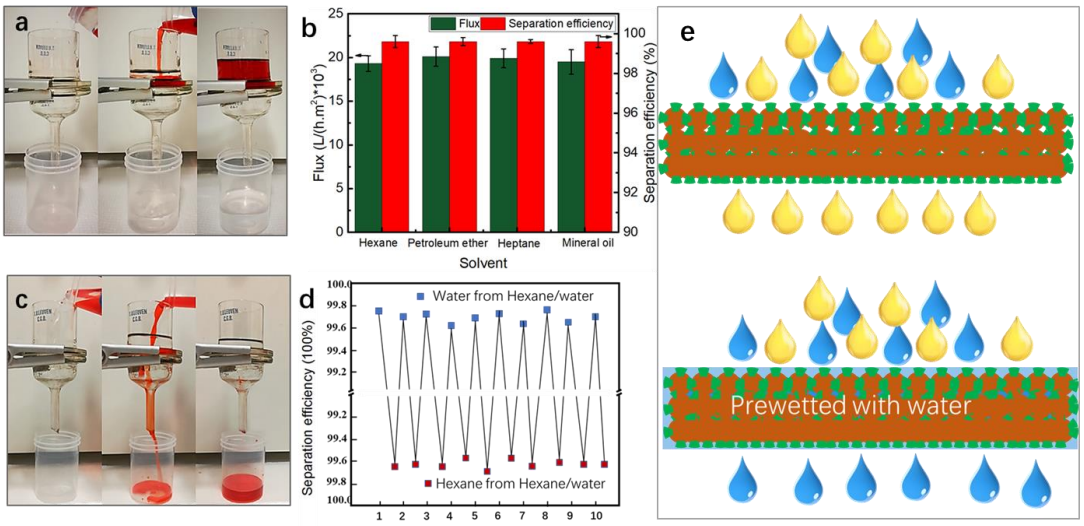


Fig. 4.11 a, Separation of hexane from hexane/water mixtures (water was marked with red dye); (b) Separation efficiency and gravity driven flux of different oils; (c) separation of water from hexane/water mixtures; (d) Separation efficiency of water from hexane/water mixtures and hexane from hexane/water mixtures in 10 cycles. (e) Switchable separation of oil/water mixtures.

To further study the separation ability of the candle soot coated membrane, the intrusion liquid pressure was measured, which indicates the maximum height (h_{max}) of liquid that the membrane can support. The intrusion pressures of various oils were measured by pouring oil onto the water prewetted membrane to achieve the maximum height (Fig. 4.12a). Similarly, the intrusion pressures of water were obtained by pouring water onto virous oils prewetted membrane to have a maximum height. The experimental intrusion pressure (ΔP) values were calculated by the following equation [164]:

$$\Delta P = \rho g h_{max} \quad (4.3)$$

In which ρ is the density of the oil or water, g is the gravitational acceleration constant, h_{max} is the maximum height of the oil or water. As shown in Fig. 4.12b, the intrusion pressure of the oils for the water prewetted membrane is around 3.2 kPa, while all of the oil prewetted candle soot coated membranes exhibited a lower intrusion pressure of water. This trend is consistent with the reported results by Li and co-workers [164].

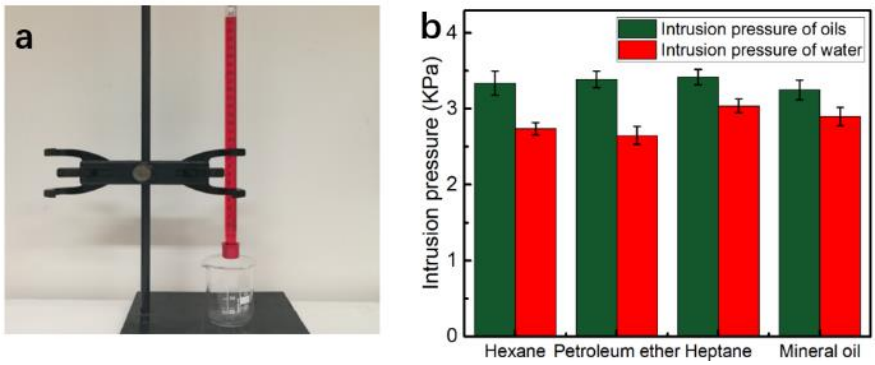


Fig. 4.12 (a) The intrusion pressure of water for the hexane prewetted membrane; (b) The experimental values of intrusion pressures for a series of oils and water.

4.3 Conclusions

In conclusion, super-hydrophobic and super-oleophilic 3D printed PSU membranes were fabricated in this chapter. The optimal 3D printed PSU membrane was fabricated with a laser power of 15 W, a hatch space of 0.15 mm and a laser scanning of 1 count. The as prepared printed membrane had a hydrophobic bottom surface with a contact of 124° and a top surface with a contact angle of 89°. After 40 mins of immersion in candle soot/hexane solution and subsequently solvent evaporation, an ordered loose network was formed on the PSU membrane surface, endowing the membrane with a super-hydrophobic and super-oleophilic property. When it was applied to the oil/water separation, this membrane exhibited a high separation efficiency of oil from oil/water

mixture. After it was rinsed by water, this membrane showed a super-oleophobic property and could separate water from an oil/water mixture. The stability of the switchable wettability was measured by 10 cycles of switchable oil/water separation. This candle soot coated 3D printed PSU membrane showed a separation efficiency over 99% for all of hexane/water separation in the 10 cycles.

Chapter 5

Surface architecture of 3D printed membrane via designing micro/nano-structural ZIF-L for efficient oil/water separation

Adapted form: Shushan Yuan, Junyong Zhu, Yi Li, Dieter Strobbe, Jian Li, Peter Van Puyvelde, Surface architecture of 3D printed membrane via designing micro/nano-structural ZIF-L for efficient oil/water separation

5.1 Introduction

The oil spill of the Sanchi oil tanker collision occurring on 6 January 2018 formed a slick layer, 13 kilometers by 11 kilometers in size on the sea surface, resulting in extensive damage to marine and wildlife habitats, the fishing industry, as well as public health. In addition to such oil spill accidents, an increasing volume of waste streams caused by frequent industrial chemical leakage and direct discharge of oily sewage poses a major threat to the environment [137, 165]. Addressing this challenge calls for new synthetic multifunctional materials with superhydrophobicity that can effectively separate oil and water. Inspired by nature (e.g., lotus leaves, gecko feet and rose petals), a variety of superhydrophobic materials for oil/water separation have been recently designed and fabricated through the control of surface roughness and surface energy of the coatings [166, 167]. Since nearly all smooth surfaces fail in exhibiting superhydrophobicity even with a low-energy coating layer, controlled fabrication of microstructures with high roughness is of critical importance to achieve superhydrophobicity [168]. Numerous attempts have been made to construct a rough architecture on a porous substrate, including the sol-gel process, chemical vapor deposition, hydrothermal treatment, dip-coating, and electrospinning [169-171]. Nevertheless, the majority of these techniques is tedious and complicated. More importantly, few methods achieve a multiscale

architecture of the surface and precisely tailor the roughness [172]. In contrast to single-scale structures either on microscale or on nanoscale, a multiscale structure enabled by integration of microscale and nanoscale architectures could drastically increase the water contact angle and decrease the sliding angle, which is presumably attributed to the presence of abundant air pockets in these well-designed structures [173]. These air pockets are capable of impeding the transition from the Cassie–Bexter state to the Wenzel state and thus give rise to an extreme superhydrophobicity, which cannot be attained by a single-scale structure. Therefore, it is important, yet challenging, to fabricate such well-defined and especially hierarchical micro/nano-structures on three-dimensional substrates, aiming at extreme superhydrophobic surface and highly efficient oil/water separation [174] [175].

Additionally, porous substrates, serving as robust supporting layers, play a significant role in the roughness and superhydropobicity of the functional materials [176]. Normally, 3-dimensional (3D) porous substrates have an intrinsically rough, microlevel porous structure and longer size along the z-direction than 2D substrates, endowing them with a longer service life and a higher separation efficacy in the field of oil/water separation. A growing number of 3D porous materials, including fabrics, sponge-based materials, foam-based materials and membranes have been developed to be applied in oil/water separation. Among these porous materials, membranes were found to have a very high separation efficiency in oil/water separation [139, 141]. However, a polymeric membrane substrate made via conventional methods typically has a relatively smooth surface, which negatively affects the microstructures of the coating layer and thus fails to achieve superhydrophobicity. Recently, additive manufacturing, popularly known as rapid prototyping or 3D printing, has aroused widespread interests in both industry and academia as a rapidly developing technology that has revolutionized the manufacturing sector [157, 177]. This software-controlled additive manufacturing technology evinces advantageous over traditional manufacturing particularly in the design of targets with complicated structures, maximizing the possibility of developing a porous 3D membrane with controlled microstructure for oil/water separation [178]. However, to the best of our knowledge, few

studies focus on the fabrication of 3D printed membranes for oil/water separation.

Metal-organic frameworks (MOFs) are a new class of porous materials of hybrid organic/inorganic nature and have attracted tremendous attention in the field of gas separation [179, 180]. Zeolitic imidazolate frameworks (ZIFs) are a sub-class of MOFs, composed of tetrahedral metal ions and imidazolate ligands [181]. Previously, it was found that a homogeneous ZIF-L layer could readily and homogeneously grow on the surface of a porous alumina disc to from rough ZIF-L membranes for gas separation [182]. Inspired by this, we hypothesize that if this ZIF-L layer could be transferred on a 3D porous substrate, a superhydrophobic surface can be attained for both practical applications and theoretical analysis. More importantly, the roughness of ZIF-L layers could be tailored by controlling the growth conditions, offering the probability of constructing hierarchical micro/nano-structures on 3D substrates. Nonetheless, in the above-mentioned study, the leaf-shaped ZIF-L compacted closely and could not assemble the rougher surface that exhibits superhydrophobic after further modification. Furthermore, the formed dense singe microscale ZIF-L layers would dramatically decline the permeability of the eventually obtained membrane materials. In this regard, designing a new layer of ZIF-L with rough and porous surface is crucial in our hypothesis.

Herein, we describe a superhydrophobic functionalized 3D printed membrane based on designing of a micro/nano-structural ZIF-L layer. This membrane shows extreme superhydrophobicity with a sliding water contact angle as low as 1.56 ^{o} and a static water contact angle as high as 158.6 ^{o}. Such high superhydrophobicity is mainly derived from the hierarchical micro/nano structures assembled by two-step growth of ZIF-L onto a rough 3D printed membrane. In specific, taking advantage of selective laser sintering, porous polyamide membranes with three-dimensional structure and rough surface were fabricated. Then, a single microscale ZIF-L with leaf-crossed structure was firstly designed by greatly increasing the concentration of the reactant aqueous system. The growth of such leaf-crossed ZIF-L on the 3D printed membrane enabled a

layer of vertically oriented ZIF-L with microscale roughness. In addition, another new ZIF-L with micro/nano structure was designed by a second growth of nanoscale flat rod-shape and needle-like ZIF-Ls on the leaf-crossed ZIF-L. The deposition of this multiscale ZIF-L on a 3D printed membrane yielded a hierarchically structural surface on the 3D membrane. After being coated with PDMS, this multiscale ZIF-L coated PA membranes exhibited extreme superhydrophobic properties. It is believed that this chapter would provide a new approach to fabricated superhydrophobic membrane for oil/water separation via 3D printing technique and designing micro/nano-structural ZIF-Ls.

5.2 Results and discussion

5.2.1 Construction of superhydrophobic single micro-structural ZIF-L layer

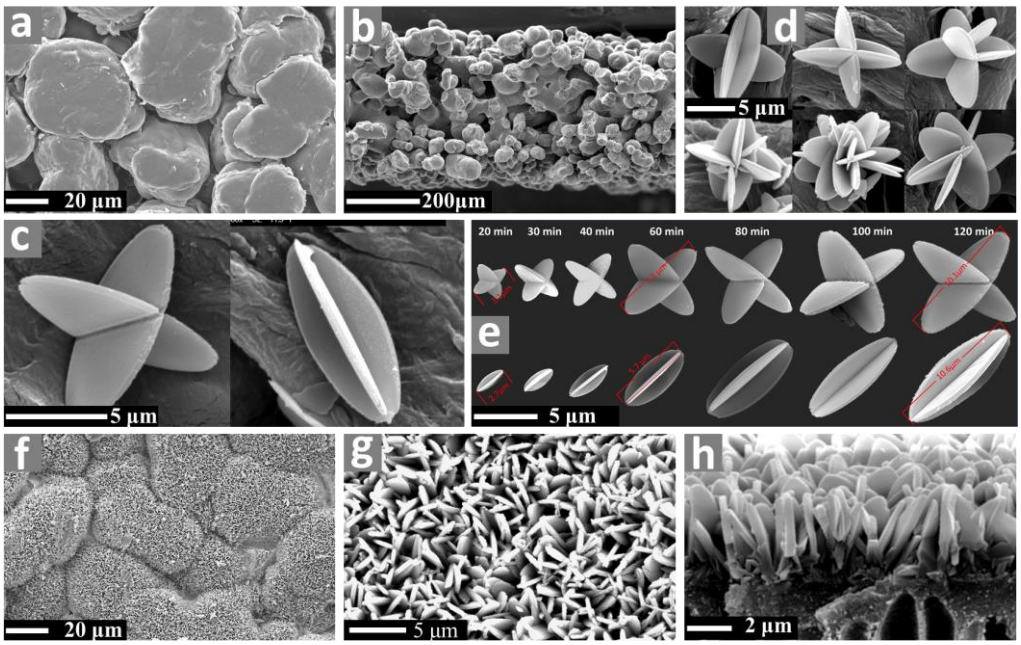


Fig. 5.1 Surface (a) and cross-section (b) morphology of 3D PA membrane; leaf-crossed ZIF-L (c) and flower-like ZIF-L (d); Growth of leaf-crossed ZIF-L with reaction time (e); surface morphology (f), magnified surface morphology (g) and cross-section morphology (h) of ZIF-L layer on support membrane (reaction time, 60 min).

Polyamide particles with an average size around 58 μm are typical materials for selective laser sintering. These particles are coalesced by a laser during the sintering process, forming a porous and rough PA support membrane (Fig. 5.1a, Fig. 5.1b). Unlike the traditional flat membrane, the surface of this 3D printed membrane is composed of many incompletely sintered parties and voids, and is thus much rougher, providing a perfect surface for further superhydrophobic modification by ZIF-L and PDMS.

Generally, ZIF-L crystals have a two-dimensional leaf-shaped morphology and are synthesized in an aqueous system with a Hmim to zinc ions molar ratio of 8 [183]. This flat two-dimensional ZIF-L is difficult to form a rough surface when growing on the surface of a substrate because of the highly compacted density. Here, by greatly increasing the concentration of Hmim and zinc ions to 0.267 mol/L and 0.033 mol/L, ZIF-L with three-dimensional structure was synthesized. As demonstrated in Fig. 5.2, various ZIF-Ls with new structures were obtained. Among them, two kinds of ZIF-L with a structure composing two symmetrically and vertically crossed leaves are the predominant types (Fig. 5.1c). The main difference between these two leaf-crossed ZIF-L is the ratio of width to length, mainly ascribed to the way how the two leaves crossed. In addition, many other ZIF-L crystals consisting more than 2 leaves, with a beautiful flower like asymmetric structures, are spotted (Fig. 5.1d). These three-dimensional ZIF-Ls would form a large number of voids when they compacted with each other on the 3D printed membrane, expected to give a rough and porous surface. To obtain a ZIF-L with proper size, the growth of these 3D leaf-crossed ZIF-Ls was studied. As shown in Fig. 5.1e, the size of leaf-crossed ZIF-Ls increases with the reaction time. In specific, when the reaction time increased from 20 min to 120 min, the size of ZIF-Ls was remarkably enlarged from 3.1 μm to 7.2 μm and from 2.7 μm to 5.7 μm respectively, indicating a rapid growth. However, when the reaction time was over 80 min, the growth of these ZIF-Ls became slow. This is mainly because of the reduction of reactant concentration due to consumption of zinc nitrate and Hmim.

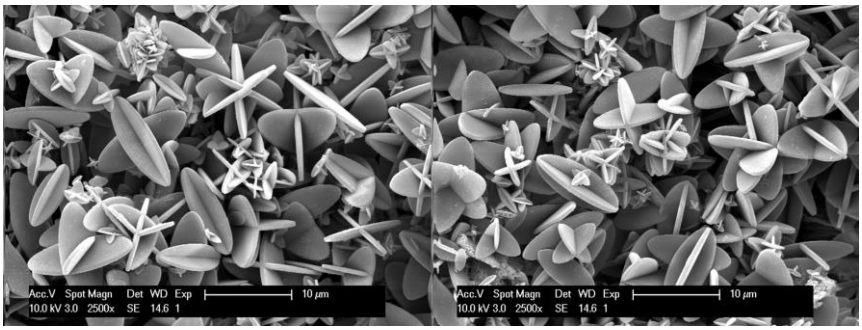


Fig. 5.2 Free ZIF-Ls on support membrane

To construct a rough surface by using these leaf-crossed ZIF-Ls, the 3D printed membrane was immersed in the reaction solution, inducing the growth of ZIF-Ls on its surface. As shown in Fig. 5.1f, after reaction for 60 min, as predicted, a rough and porous ZIF-L layer composed of vertically oriented ZIF-Ls (Fig. 5.1g, Fig. 5.1h) was synthesized on this support membrane. More specifically, the effect of immersion time on ZIF-Ls was studied. As shown in Fig. 5.3, after reaction for 5 min, small ZIF-Ls with a size of around 20 nm were randomly deposited on the PA membrane surface. With the increase of immersion time to 20 min, a complete ZIF-L layer covering the PA membrane surface was formed. Further prolonging the reaction time from 20 to 60 min resulted in a rougher porous surface composed of vertically oriented lager ZIF-L crystals. However, when the reaction further increased from 80 min to 120 min, plenty of new small ZIF-L crystals grew between larger crystals, forming a relatively dense surface.

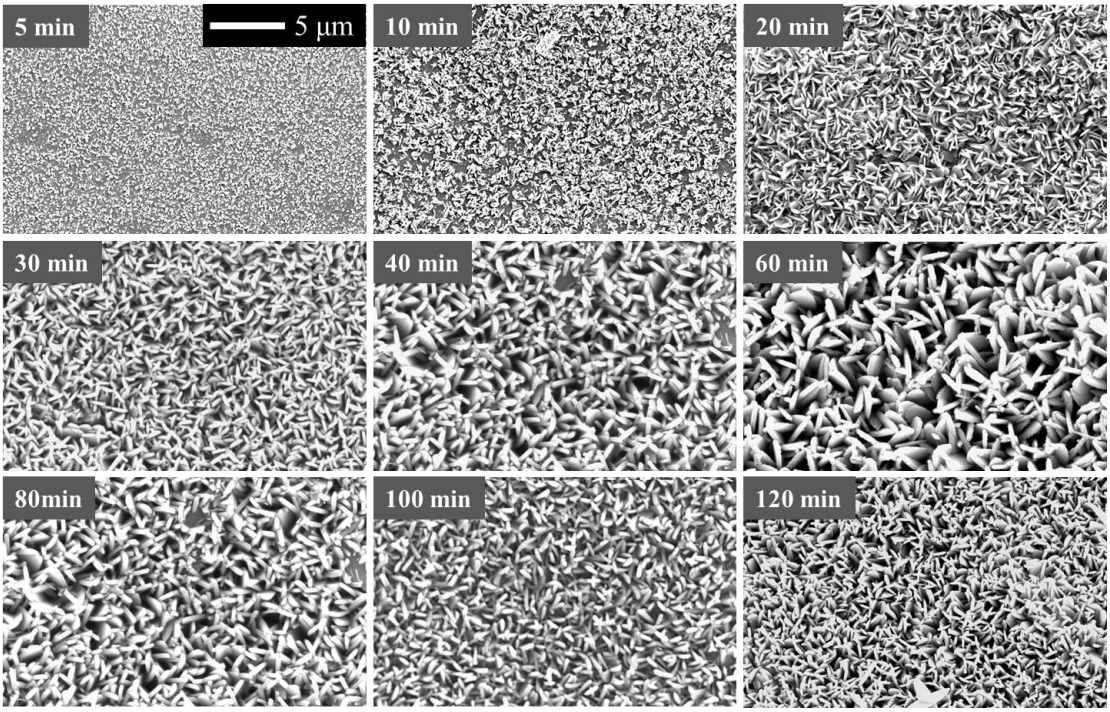


Fig. 5.3 surface morphology of ZIF-L layer after reaction with different time (5, 10, 20, 30, 40, 60, 80, 100, 120 min) on PA porous membrane.

In addition, the change of ZIF-L layer thickness was also investigated. As shown in Fig. 5.4, the thickness of this ZIF-L layer increased rapidly from 0.15 μm to 2.01 μm during the first 60 min reaction time (Table 5.1). Further prolonging the reaction time to 120 mins resulted in a slow increase of ZIF-L layer thickness to 3.02 μm, demonstrating a decreased reaction rate. This is mainly due to the reduction of Hmim and $Zn(NO_3)_2 \cdot 6H_2O$ in the reaction solution resulting from the consumption of these two chemicals. In the end, based on the above images and discussion, a rough and porous surface was constructed by deposition of 3D leaf-crossed ZIF-Ls on the 3D printed PA membrane.

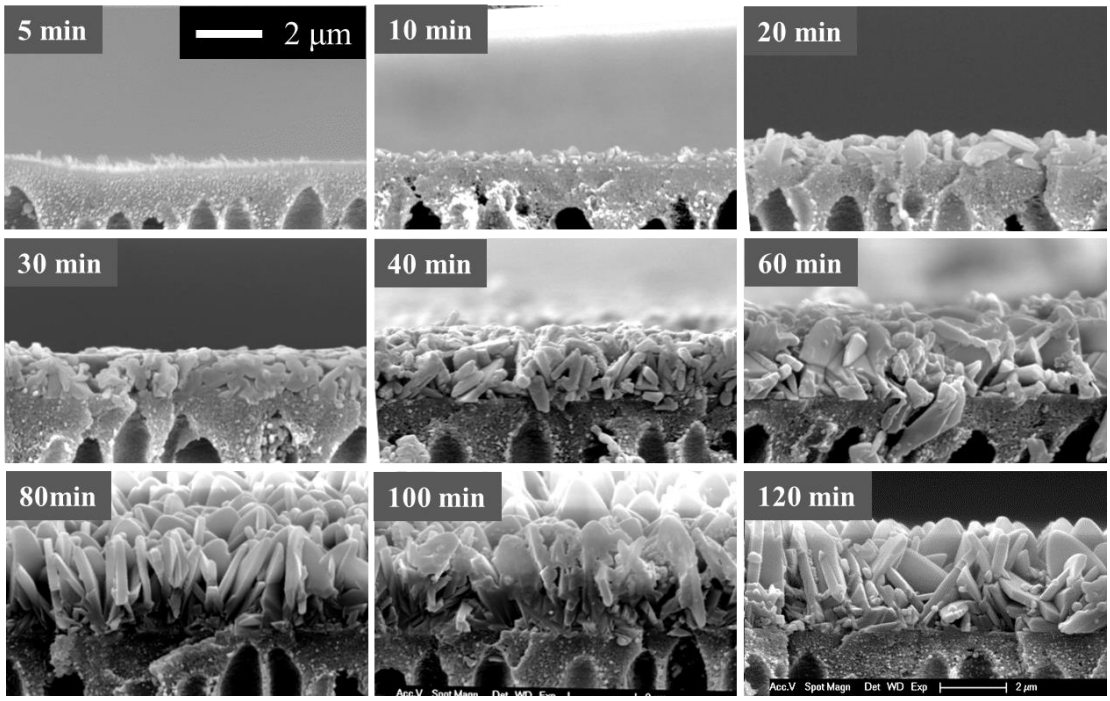


Fig. 5.4 Thickness of ZIF-L after reaction with different time (5, 10, 20, 30, 40, 60, 80, 100, 120 min) on substrate.

Table 5.1 Thickness of ZIF-L layer on PA membrane after reaction with different time

Time (min)	5	10	20	30	40	60	80	100	120
Thickness (μm)	0.15	0.32	0.85	1.14	1.43	2.01	2.32	2.62	2.77

The X-ray diffraction (XRD) pattern of leaf-crossed ZIF-L and the simulated normal ZIF-L are compared in Fig. 5.5a. These two types ZIF-Ls display exactly the same XRD pattern, indicating the same crystal even with different structures. In order to obtain a possible superhydrophobic surface from ZIF-L layer, PDMS was coated on the surface of ZIF-L layer to endow this layer with hydrophobic chemistry. As indicated by the element Si in energy dispersive X-ray (EDX) spectrum in Fig. 5.6, PDMS was successfully deposited on the surface of the ZIF-L layer. The static water contact angles of PDMS-ZIF-PA membranes obtained from different reaction times were measured. As shown in Fig. 5.5b, once a ZIF-L layer was formed on the surface of the PA membrane, the water contact angle dramatically increased to 139° due to the large increase in roughness. When the growth time increased from 20 min to 60 min, the

water contact angle increased to 153°, demonstrating superhydrophobicity. This is because the growth of ZIF-L leads to an enlargement of their size, resulting in a larger roughness. Further increasing the growth time to 120 min leads to a slight decrease of the water contact angle to 146 °, which is attributed to the growth of smalls crystals between larger ZIF-Ls. Obviously, the ZIF-L layer synthesized after 60 min exhibited superhydrophobic properties. This is mainly attributed to the hydrophobic nature of the PDMS and the rough surface constructed by the three-dimensional leaf-crossed ZIF-Ls. Compared to the normal 2-dimentional leaf-shaped ZIF-Ls, the designed new 3-dimensional ZIF-Ls could provide a larger number of voids when they compacted with each other on a 3D membrane. These voids would act as air pockets when the water contact the surface of this ZIF-L layer, which largely improves the water contact angle.

Static water contact angles of PA, PDMS-PA, ZIF-PA and PDMS-ZIF-PA membranes during 60 sec were measured to evaluate the hydrophobic performance of these membranes (Fig. 5.5c). For the porous 3D printed polyamide membrane, the water contact angle decreased from 109° to 76° during 60 sec, indicating a relatively low contact angle stability. After depositing a ZIF-L layer on the surface of this 3D printed membrane, the water contact angle dramatically reduces from 119 ° to 0 ° during 25 sec, which is greatly attributed to the capillary effect derived from the large number of pores in ZIF-L and gaps between ZIF-Ls. After being coated with PDMS, the stability of the hydrophobicity was greatly improved. The PDMS-PA membrane exhibits a relative stable contact angle during 60 sec. The PDMS-ZIF-PA membrane demonstrates the largest water contact angle of 153 ° with ultrahigh stability during 60 sec, evincing a superhydrophobic surface.

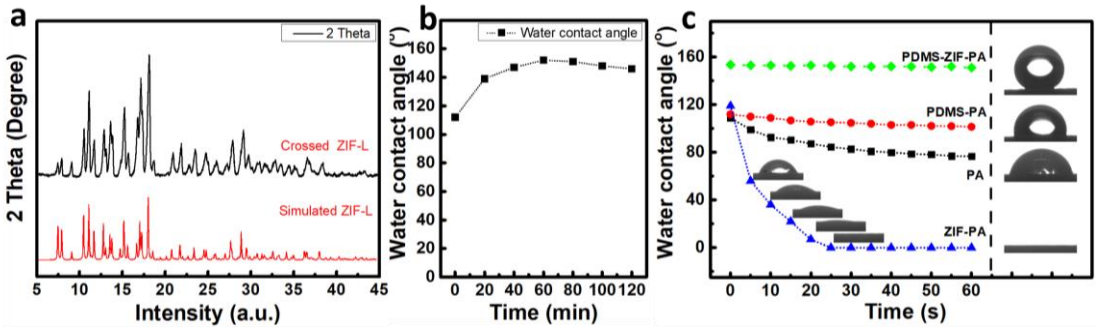


Fig. 5.5 XRD Pattern of leaf-crossed ZIF-L (a); water contact angle of PDMS-ZIF-PA membranes obtained from different reaction time (b); static water contact angles of PA, PDMS-PA, ZIF-PA and PDMS-ZIF-PA membranes during 60 sec (c).

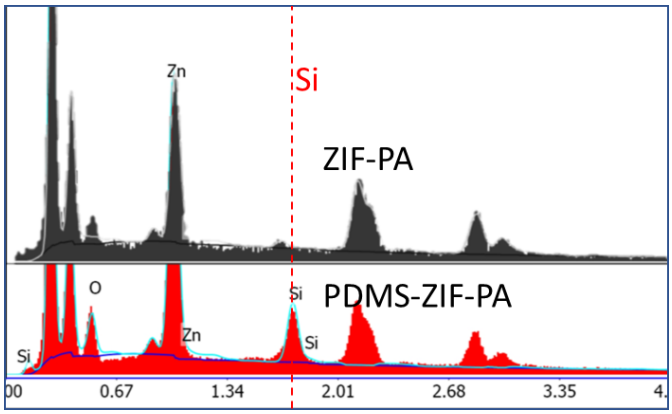


Fig. 5.6 EDX spectrum of membrane ZIF-PA and PDMS-ZIF-PA

5.2.2 Construction of superhydrophobic micro/nano structural ZIF-L layer

Generally, multiscale structures with microscale and nanoscale architectures, can provide superhydrophobicity by provoking larger water contact angle and smaller sliding angle due to a large amount of air pockets in these structures. These air pockets impede the transition from the Cassie–Bexter state to the Wenzel state, resulting in an extreme superhydrophobicity rather than a single-scale roughness. Therefore, to surpass the hydrophobicity limitation of the single micro-scale ZIF-L layer, constructing ZIF-Ls with multiscale structure would be helpful. A ZIF-L with multiscale structure was

designed by a simple second growth of small flat rod-shape ZIF-Ls on the larger leaf-crossed ZIF-Ls (Fig. 5.7a). In specific, as shown in Fig. 5.7c, most of such flat rod-shape ZIF-Ls are orderly vertically grown on the edge of large leaf-crossed ZIF-Ls, while many horizontally oriented needle-like ZIF-Ls (Fig. 5.7b) are orderly grown on the surface near the center. These flat rod-shape and needle-like ZIF-Ls on nanoscale and the leaf-crossed ZIF-Ls on microscale together constitute ZIF-L with hierarchical micro/nano-structure. Moreover, via deposition of such micro/nano scale ZIF-Ls on a 3D printed PA membrane surface, various homogeneous hierarchical structural surfaces (Fig. 5.7d, 5.7e and 5.7f) were obtained by a simple immersion of the leaf-crossed ZIF-Ls coated PA membranes in Hmim/$Zn(NO_3)_2 \cdot 6H_2O$ aqueous solution for a second growth of 5 min, 15 min and 30 min. These hierarchical structural surfaces are composed of microscale leaf-crossed ZIF-Ls and the nanoscale flat rod-shape ZIF-Ls. As shown in Fig. 5.7g, 3h and 3i, the size of small ZIF-Ls increased from 130 nm to 670 nm with increasing second growth time from 5 min to 30 min. Most importantly, a large number of air pockets was created in the hierarchical structure, which would greatly improve the superhydrophobicity of the obtained membranes.

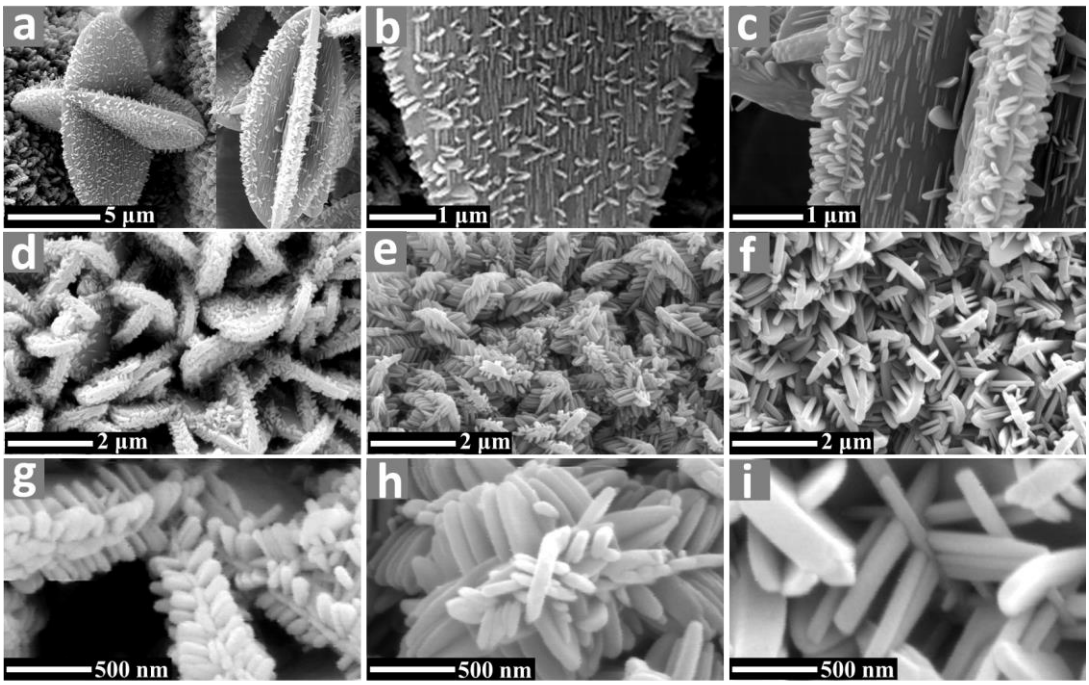


Fig. 5.7 (a) micro/nano structural ZIF-Ls with; (b) horizontally oriented needle-like ZIF-Ls; c flatly rod-shaped ZIF-Ls on the edge of larger crossed ZIF-Ls; surface of multiscale ZIF-L layer synthesized after a second growth of 5 min (d), 15 min (e) and 30 min (f); Magnified surface morphology of multiscale ZIF-L layer synthesized after a second growth of 5 min (g), 15 min (h) and 30 min (i).

After being coated with PDMS, the superhydrophobicity of these multiscale surfaces was measured by static water contact angles. As shown in Fig. 5.8a, compared to the other surfaces, especially the single micro-scale ZIF-L layer, the multiscale surface obtained after a second growth of 15 mins exhibits the largest water contact angle, as high as 159 º, demonstrating a significant improvement of superhydrophobicity. In addition, the sliding angle of this multiscale ZIF-L layer is as low as 1.56 º, which is significantly lower than that of a single micro-scale ZIF-L layer (6.6 º) (Fig. 5.8b). Based on these water contact angle results, it is safe to conclude that the superhydrophobicity of ZIF-L layer was greatly improved after designing a multiscale structure. Moreover, the micro/nano scale ZIF-L layer also exhibited a super-oleophilicity. When an oil drop contacts the surface of this layer, it spreads immediately

along the surface and permeates in the membrane with 0.34 s, implying a super-oleophilic surface (Fig. 5.8c). This functional superhydrophobic and superoleophilic ZIF-L coated membrane is a perfect material for oil/water separation.

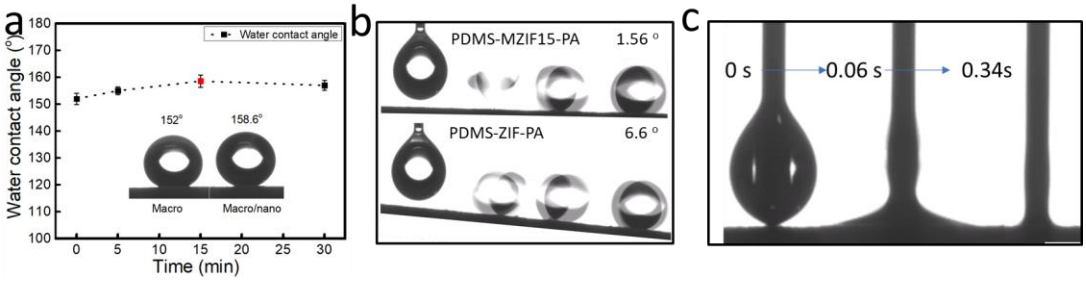


Fig. 5.8 (a) Water contact angle of the PDMS-MZIF5-PA, PDMS-MZIF15-PA and PDMS-MZIF30-PA; (b) Sliding water contact angle of PDMS-MZIF15-PA and PDMS-ZIF-PA; (c) oil (hexane) contact angle of PDMS-MZIF15-PA.

The highly superhydrophobic properties of PDMS-MZIF15-PA is mainly derived from the hierarchical structure constructed via 3D printing, structure designing of ZIF-L and deposition. In specific, as shown in Fig. 5.9, the 3D printing technique endows the surface of the obtained PA membrane with roughness on microscale. Then, the growth of leaf-crossed ZIF-L with size around 2 μm to 10 μm enabled this rough PA membrane to have a roughness in minor microscale. In the end, second growth of nanoscale ZIF-Ls on this ZIF-L layer yielded a ZIF-L layer with roughness on nanoscale. These combined microscale-minor microscale-nanoscale structures create a large number of voids or air pockets, endowing this micro/nano-structural ZIF-L layer with extreme superhydrophobicity.

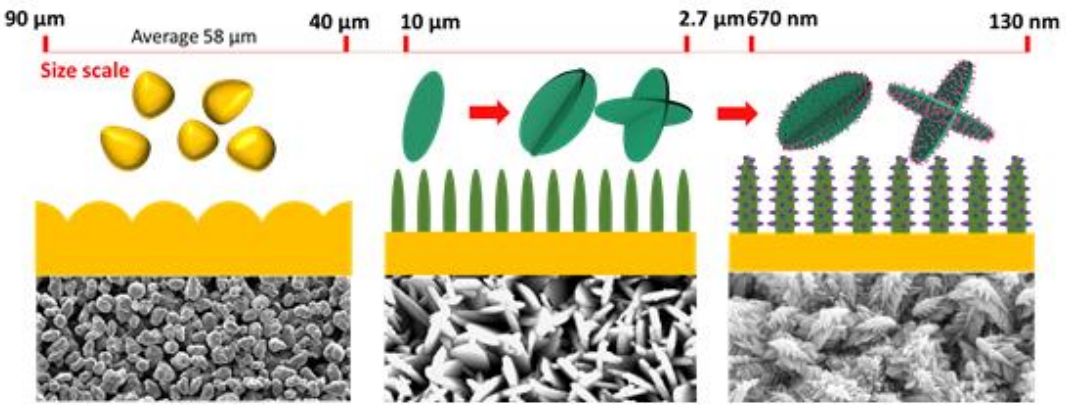


Fig. 5.9 Construction of hierarchical micro/nano structure surface on 3D printed membrane.

5.2.3 Oil/water separation performance of PDMS-MZIF15-PA

The oil/water separation was carried out by oil absorption and oil/water mixture filtration experiments. As presented in Fig. 5.10a, the colorless oil drop (hexane) was totally absorbed when this superhydrophobic and superoleophilic PDMS-MZIF15-PA membrane contacted the oil drop in the red water, suggesting a perfect separation of oil from water by absorption. In addition, oil/water mixture filtration experiments were conducted as shown in Fig. 5.10b. The functional membrane was placed between the two glass vessels. When an oil/water mixture was poured in the upper glass vessel, the red water was repelled while the oil permeated through the membrane. In the end, red water was rejected in the upper glass vessel while the oil was collected in a plastic container, demonstrating a successful oil/water separation. Most importantly, this oil/water separation was completed under the driven of gravity without applying pressure.

To evaluate the performance of this functional superhydrophobic and superoleophilic PDMS-MZIF15-PA membrane in oil/water filtration, the gravity driven flux and rejection of different oils including hexane, petroleum ether, heptane and mineral oil were measured. As shown in Fig. 5.10c and Fig. 5.10d, for all of these oils, this

membrane exhibited a gravity driven flux above 24,000 L/(m² h) and rejection of over 99%.

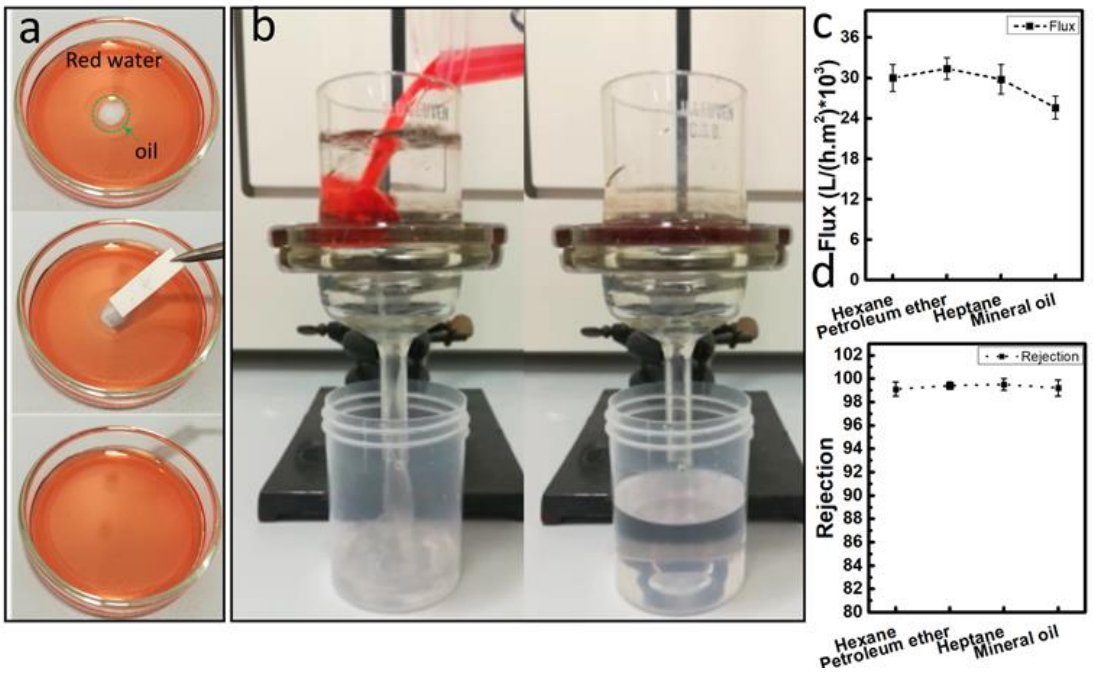


Fig. 5.10 a Absorption of oil drop in water; b Separation of oil from water; c Flux of different oil; d Rejection of different oil during oil/water separation.

5.3 Conclusions

In summary, a superhydrophobic micro/nano-structural 3D printed membrane with a sliding water contact angle as low as 1.56° and a static water contact angle as high as 158.6° was fabricated. Different from normal 2-dimensional leaf-shaped ZIF-Ls, 3-dimensional microscale ZIF-L with leaf-crossed structure was synthesized. Moreover, through a second growth, new micro/nano-structural ZIF-L with small flat rod-shape and needle-like ZIF-Ls was designed. The deposition of such multiscale ZIF-L on a rough 3D printed PA membrane yields a multiscale micro/nano-structural ZIF-L layer. After being coated with PDMS, this membrane exhibits an extreme superhydrophobicity and an efficient oil/water separation. The present development provides a highly efficient and facile strategy to construct multiscale micro/nano-

structures. It is expected to provide inspiration for the fabrication of membranes by 3D printing and the construction of multiscale micro/nano-structures by designing ZIF-L with new multiscale structures.

Chapter 6

New promising polymer for organic solvent nanofiltration: Oxidized poly (arylene sulfide sulfone)

Adapted from: Shushan Yuan, Juan Wang, Xin Li, Junyong Zhu, Alexander Volodine, Xiaojun Wang, Jie Yang, Peter Van Puyvelde, Bart Van der Bruggen, New promising polymer for organic solvent nanofiltration: Oxidized poly (arylene sulfide sulfone), Journal of Membrane Science, 549 (2018) 438-445.

6.1. Introduction

Solvent-resistant nanofiltration or organic solvent nanofiltration (OSN) is a promising pressure-driven membrane process for separations in organic media. Because of its high efficiency, low energy consumption and operational stability, OSN has been applied in catalyst and solvent recovery and pharmaceutical purification [1, 184]. Compared to a conventional nanofiltration membrane, an OSN membrane should be chemically stable and robust to endure continuous contact with organic solvents.

Inorganic membranes can be good candidate due to their intrinsic excellent chemical durability [185]. However, fabrication of ceramic nanofiltration membranes is challenging, thus they are expensive. A variety of polymers is extensively used in membrane synthesis with superior advantages in scaling up, which evinces an interesting alternative for OSN application. Among these polymers, (polyimide) PI [26], (polydimethylsiloxane) PDMS [27], (polyacrylonitrile) PAN [28], (polyether ether ketone) PEEK [29] and (polybenzimidazole) PBI [30, 31] have been utilized for synthesis of solvent stable membranes. Nevertheless, problems such as swelling and dissolution of these polymers in aggressive solvents, which inevitably result in a loss of membrane selectivity, still impede practical applications. Therefore, the exploration

of new polymers and advanced modification methods to improve the chemical resistance of existing polymeric membranes is a research trend in the field of OSN.

Poly (arylene sulfide sulfone) (PASS), a type of newly developed high-performance engineering plastics, is structurally modified from polyphenylene sulfide (PPS) [186]. Fig. 6.1 shows the synthesis route and the chemical structure of PASS. The phenylene groups are connected by alternating sulfone groups and thioether linkages. The glass transition temperature (T_g) of PASS is ca. 218 °C, and almost 130 °C higher than that of PPS, which indicates its high thermal stability. Furthermore, the favorable chemical stability and relatively low cost of PASS make it an attractive material to prepare solvent resistant membranes. Pan and coworkers have reported that PASS membranes have a good solvent resistance in n-hexane, ethyl acetate, methanol, diethyl ether and toluene [187]. However, these solvents are not very aggressive; the solvent resistance of PASS is not strong enough to be used in polar aprotic solvents like dimethylformamide (DMF) and n-methyl-2-pyrrolidone (NMP).

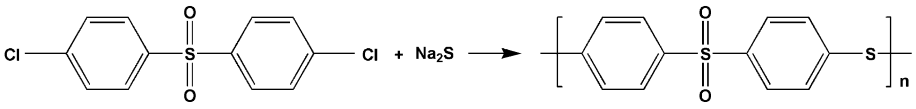


Fig. 6.1. Synthesis route of poly (arylene sulfide sulfone) (PASS).

Many different strategies can be implemented to optimize OSN membranes to improve their chemical durability, including cross-linking, wet or dry annealing and incorporating inorganic nanoparticles [188]. However, little research has been done to enhance the membrane stability by changing or modifying the polymer chain at molecular level. The reverse of polymer solvent resistance is polymer dissolution. Solvent diffusion and polymer chain disentanglement are two crucial processes in polymer dissolution. A loose packing and weak intermolecular interactions of polymer chains give rise to a weak chemical stability. This is mainly because the solvent molecules relatively easily break the intermolecular interaction, diffuse into polymer chains and cause dissolution [189]. On the contrary, chemical stability of polymer

would be increased by improving the polymer chain rigidity, intermolecular interaction and packing density of polymer chains. Some existing polymers are solvent resistant because of their special polymer chain structure. Polypropylene can be used as nonwoven in the fabrication of OSN membranes; its solvent resistance is due to the highly orderly packed polymer chains in the crystalline region, which prevent the solvent from penetrating into the polymer chains, let alone dissolve them. As to the intermolecular interaction, solvent resistant cellulose can be a very good example [190]. The intramolecular hydrogen bonding, from one unit to the next, is preferred and create insoluble structures, which make the solvent difficult to dissolve callouses. More examples can be found, including polytetrafluoroethylene, polyethylene and polyethylene terephthalate. The high intermolecular interaction, packing density and chain rigidity make the polymer difficult to dissolve; this is a general principle in polymer science [191]. However, these general principles have not been used intentionally in promoting the solvent resistance of a polymer in the fabrication of OSN membranes.

PASS is a newly developed high-performance polymer; at molecular level it is built up by thioether groups (-S-), sulphone (-SO_2-) and benzene rings. The C–S bond has a bond length of 180 pm and a bond angle of 90°, which is relatively large and gives more freedom for the PASS chain to move. The -SO_2- units is a polar group, which will reinforce the intermolecular interaction of polymer chains. This gives an opportunity to intentionally improve the solvent resistance of PASS by increasing the packing density, intermolecular interaction of PASS chain via the transfer -S- to -SO_2- in the PASS chain. It was reported that the -S- group can be oxidized into -SO_2- by using hydrogen peroxide (H_2O_2), concentrated nitric acid or their mixtures with other solvents [192-194]. Compared with other oxidization agents, H_2O_2 is green and the most versatile, economical and reproducible [195].

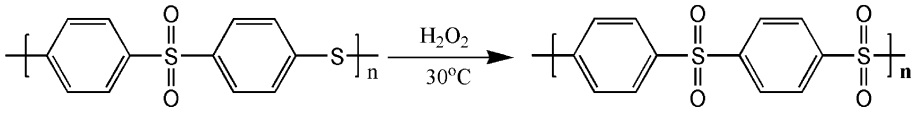


Fig. 6.2. Oxidation reaction of PASS.

In this chapter, the strategy of improving polymer chain intermolecular interaction, packing density and chain rigidity at molecular level was intentionally employed to increase the PASS solvent resistance and fabricating OSN membrane via a simple oxidization process. Hydrogen peroxide (H_2O_2) was used to oxidize –S- into -SO_2- to modify the structure of PASS chains, and improve its chemically stability. The chemical reaction during oxidization is shown in Fig. 6.2. Porous PASS membranes were prepared via phase-inversion and then oxidized by H_2O_2 in acetic acid. Fourier transform infrared spectroscopy (FT-IR) analysis and X-ray photoelectron spectroscopy (XPS) were carried out to confirm the chemical structure changes during the oxidization process. The performance and stability of these pristine and oxidized PASS membranes were measured after three days of exposure to several solvents. OSN was performed to investigate the performance of oxidized PASS membranes.

6.2. Results and Discussion

6.2.1 Chemical changes of PASS membrane during oxidization

FT-IR analysis of oxidized PASS

The oxidation was indicated by a change of the membrane color, from light brown to white, suggesting that chemical reaction took place during the oxidation process. ATR-FTIR analysis was carried out to study the chemical changes during the oxidation reaction. As shown in Fig. 6.3a, the intensity of the peaks at 1073 cm^{-1} and 763 cm^{-1} attributed to the sulfide (-S-) group decreased after oxidation, which demonstrates that the number of sulfide groups in the modified PASS chain was reduced compared to that in pristine PASS chain. Although there is no obvious difference in the peaks at 1320

cm^{-1} and 1156 cm^{-1} which correspond to the characteristic peak of sulfone (-SO_2-), the peak at 1180 cm^{-1} assigned to the asymmetric stretching of -SO_2- increased, which suggests that the density of -SO_2- units increased in the oxidized PASS chain. Due to the increase of polar -SO_2- units in the PASS chains, the intermolecular interactions are dramatically increased, which restricts the stretching vibration of C-C in benzene rings. For this reason, the peaks at 1573 cm^{-1}**,** 1475 cm^{-1} attributed to the symmetric benzene ring stretching peak disappeared or decreased after oxidation.

XPS analysis on the membrane surface

The reaction was further confirmed by using X-ray photoelectron spectroscopy (XPS) spectra. Fig. 6.3b shows the S2p X-ray photoelectron spectroscopy (XPS) spectra of the pristine PASS and the oxidized PASS. The pristine PASS exhibits two sulfur peaks, which reveals that the S atom occurs in the polymer backbone mainly as sulfone (-SO_2-, at 166.7 eV) and thioether (-S-, at 162.5 eV) [196]. The modified PASS has only one sulfur peak (168.0 eV) and the intensity of this peak is almost equal to the sum of the two peaks in the spectra of pristine PASS. In addition, the percentage of O was increased from 13.6% to 21.0% after oxidization. Based on this information from XPS, it can be concluded that the thioether units was successfully changed into sulfone units after oxidation.

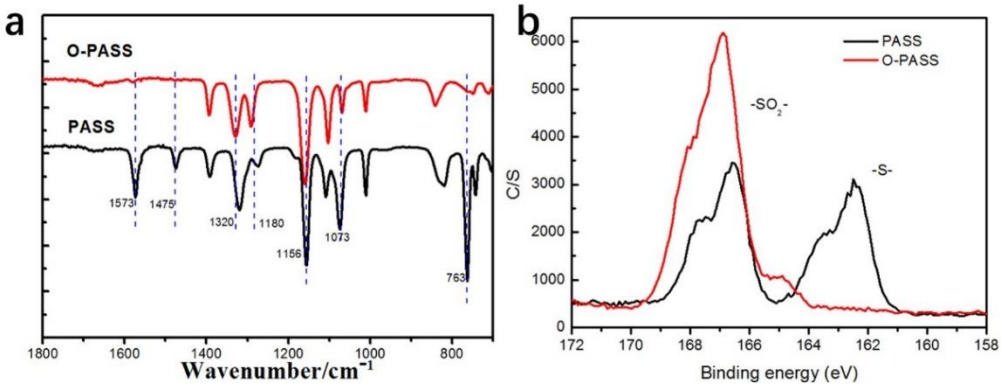


Fig. 6.3. (a) FT-IR spectrum of PASS membrane before and after oxidation (O-PASS). (b) XPS analysis of sulfur for PASS and oxidized PASS.

Based on the ATR-FTIR and XPS analysis, the conversion of thioether (-S-) in the polymer backbone to sulfone (-SO_2-) during post-oxidation by hydrogen peroxide was confirmed.

6.2.2 PASS membrane physical properties and filtration performance before and after modification

Membrane morphology and surface roughness

The morphology of the membranes' cross-section can be seen in Fig. 6.4 (a, b, c and d). Both pristine PASS and modified PASS membranes showed a similar typical asymmetric morphology with a thin skin layer upon a porous support; the porous support consisted of finger-like macrovoids structures. In addition, it can be observed that the oxidization process did not change the surface and cross-section morphology of PASS membranes. This indicates that the adopted oxidation process with H_2O_2 was mild enough to maintain the integral structure of the PASS membrane, without damage.

Information about the membrane surface morphology and roughness of pristine and oxidized PASS membrane was obtained by AFM analyses and is shown in Fig. 6.4e, Fig. 6.4f, Fig. 6.4g and Fig. 6.4h. The surface roughness values of the membranes on 1 × 1 μm^2 and 5 × 5 μm^2 scans, as represented by mean root square roughness (R_{rms}), average roughness (R_a), and the maximum vertical difference between the highest and lowest points (R_m), are listed in Table 6.1. Based on these values, it was found that the PASS membranes have a rougher surface than O-PASS, which can be confirmed by the AFM image on the scale of 5 × 5 μm^2. However, a significant surface morphology difference between PASS and O-PASS can be spotted in the AFM images of PASS and O-PASS on the scale of 1 × 1 μm^2. More specifically, it was found that the pristine PASS membrane exhibits a very smooth surface morphology but with higher average roughness (6.64 nm), while the oxidized PASS membrane shows rough peaks and valleys but with smaller average roughness (3.11 nm). During the oxidization process, the acetic acid molecules penetrate into the PASS membrane, cause swelling and

provide channels for hydrogen peroxide molecules to diffuse into the PASS membrane, finally inducing the chemical reactions. Those generated peaks and valleys on the O-PASS membrane surface at the nanometer level can be attributed to the relaxation of PASS chains during the swelling and reconfiguration of O-PASS chains arrangement.

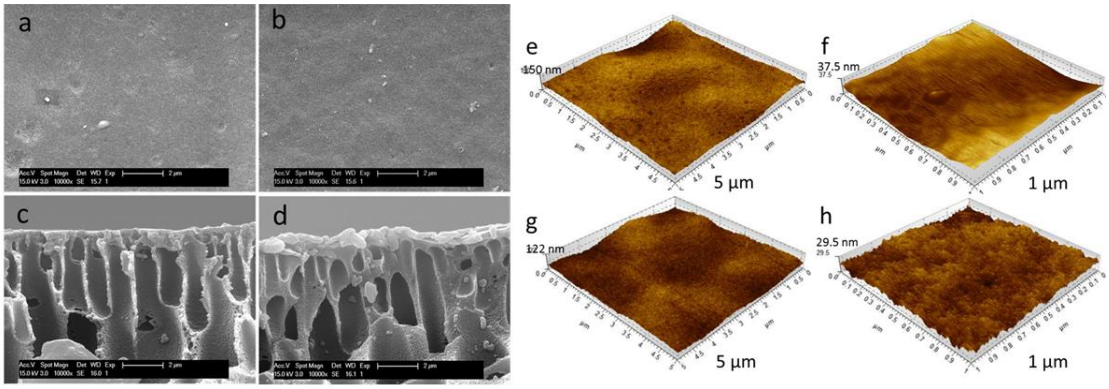


Fig. 6.4. SEM images of the PASS membranes: a, b surface of pristine PASS and oxidized PASS; c, d cross-section of pristine PASS and oxidized PASS. AFM 3D images of pristine (e, f) and oxidized PASS membranes (g, h).

Table 6.1 AFM surface roughness parameters of the pristine and modified PASS membranes: R_a (average roughness), R_{rms} (root mean square roughness), and R_m (maximum vertical difference between the highest and lowest points)

Membrane	R_a (nm) 1 µm	R_{rms} (nm)	R_m (nm)	R_a (nm) 5 µm	R_{rms} (nm)	R_m (nm)
PASS	6.64	7.96	37.8	14.3	18.2	150
O-PASS	3.11	3.87	29.6	11.4	14.0	124

Permeability and rejection

The permeation and rejection measurements of PASS and O-PASS membranes were performed at room temperature. The permeability of PASS membranes increases from 66 L/(h.m^2.bar) to 79 L/(h.m^2.bar) after oxidation; this can be seen in Fig. 6.7. Moreover,

the oxidized PASS membrane has a slightly higher RB rejection: 41% compared to 38% for a pristine membrane. The high permeability is mainly attributed to the enhanced hydrophilicity due to the increased amount of polar sulfone in the chain of O-PASS. The hydrophilicity increase was confirmed by contact angle measurements**.** The contact angle of PASS membranes decreases, from 70° to 51° after oxidization. In addition, the swelling of PASS in acetic acid could make the PASS polymer chains expand from a compacted state to a loose state. The expanding of polymer chains would squeeze the pores of PASS membrane, resulting in a membrane with smaller pores, giving the oxidized PASS membrane an enhanced rejection.

Solvent resistance

PASS and O-PASS membranes were immersed in $CHCl_3$, NMP and 98%H_2SO_4 for 3 days to evaluate their chemical stability. At the end of these 72 hours, a picture was taken (shown in Fig. 6.5). As could be expected based on the solvent stability previously reported [197], the PASS membranes dissolved almost immediately in NMP, 98% H_2SO_4 and $CHCl_3$. Surprisingly, the oxidized PASS membrane shows a corrosion resistance in NMP, 98% H_2SO_4 and $CHCl_3$ in contrast to its original counterpart. The oxidized PASS membranes were found insoluble in the three solvents.

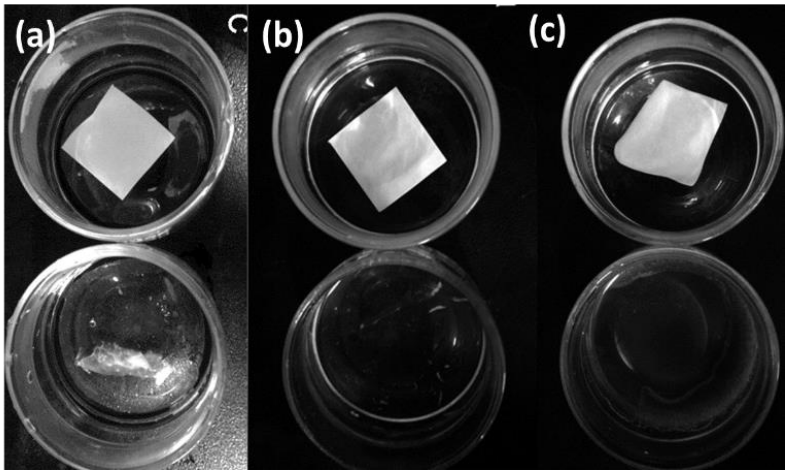


Fig. 6.5. Oxidized PASS membrane (up) and pristine PASS membrane (down) after exposure to different solvents for 72 hours: (a) $CHCl_3$ (b) NMP (c) 98%H_2SO_4.

Although oxidized membranes can keep their shape in the solvents, the microstructural changes in the membranes, which may affect the membrane performance, were still uncertain. Therefore, the microstructure of O-PASS membranes was further characterized by SEM images.

Fig. 6.6 shows the scanning electron micrographs of the sponge structure of the O-PASS membranes after soaking in different solvents ($CHCl_3$, NMP and 98% H_2SO_4). It is important to note that no significant morphological difference could be observed for $CHCl_3$ and NMP treated O-PASS membranes and the spongy part still keeps its porous structure after being immersed in NMP, which was previously used as the solvent in the membrane casting process. Similar observations were made for membranes treated with $CHCl_3$. The spongy part in oxidized PASS membranes treated by 98% H_2SO_4 exhibits some shrinkage and becomes very dense; this structural change can be also spotted in the cross-section of 98% H_2SO_4 treated O-PASS membranes. No changes of the membrane surface structure and finger structure in the cross section for this membrane were observed.

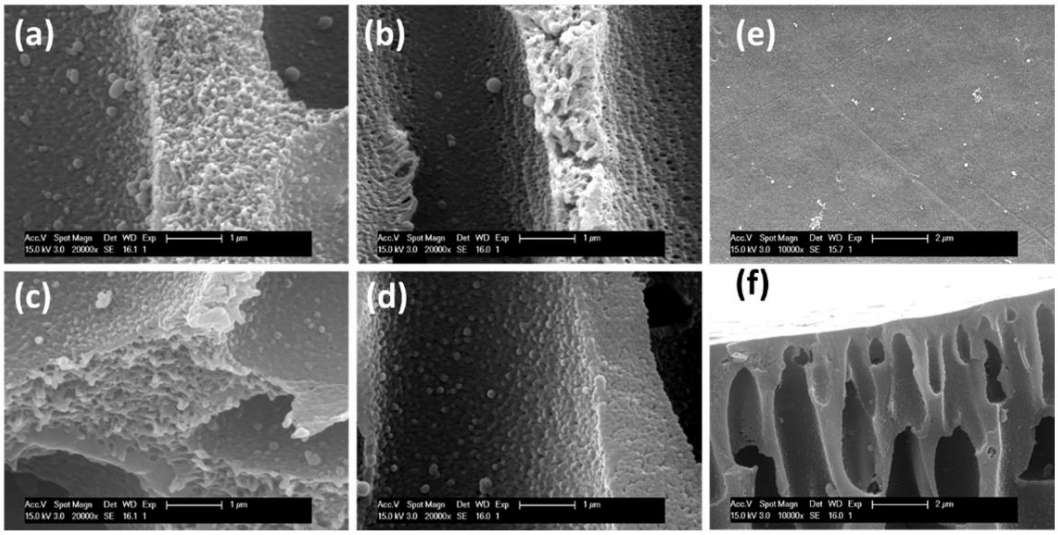


Fig. 6.6. Sponge structure in O-PASS membrane (a), $CHCl_3$ treated O-PASS membrane (b), NMP treated O-PASS membrane (c) and 98%H_2SO_4 treated O-PASS membrane (d); Surface (e) and cross-section (f) morphology of 98%H_2SO_4 treated O-PASS membrane.

Finally, membrane filtration measurements were conducted with the solvent treated O-PASS membranes to further confirm the solvent resistance of the O-PASS membrane. Results are summarized in Fig. 6.7. The permeability of the initial O-PASS membrane was 78 L h^{-1} m^{-2} bar^{-1} and the RB rejection was 41%. Interestingly, the permeability and RB rejection increased greatly after being treated by these solvents. Numerous studies reported the effect of solvents on membranes, varying from some swelling to dissolution or disintegration, typically leading to a loss in performance of membranes in filtration [198-201]. However, for oxidized PASS, the filtration performance was greatly improved by the solvent treatment. The NMP treated O-PASS membrane shows a permeability increase by 43%, and an increase of the RB rejection by 58% compared to the untreated oxidized PASS membrane; it also has the highest permeability and rejection among all solvent treated membranes. Unexpectedly, the 98% H_2SO_4 treated O-PASS membrane also shows an enhancement in permeability although this membrane has a much denser sponge structure compared to the O-PASS membranes.

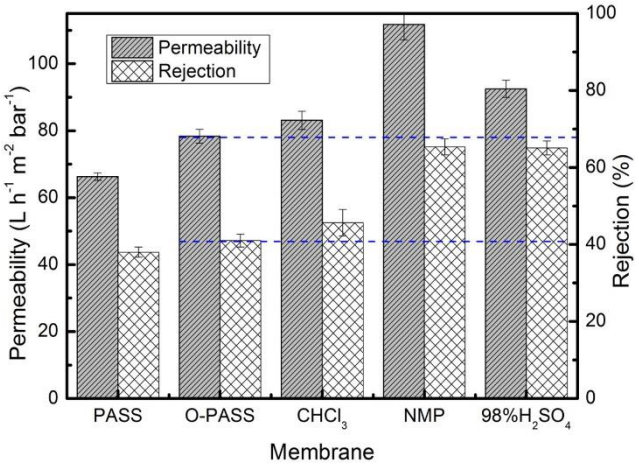


Fig. 6.7 The pure water permeability and RB rejection of PASS membranes, O-PASS membranes and solvent ($CHCl_3$, NMP and 98% H_2SO_4) treated O-PASS membranes. (PASS concentration 20 wt %)

The increase of rejection was mainly due to the slight swelling of O-PASS chains in NMP, which gives the rigid O-PASS chains a chance for relaxation. Because the

polymer solution on the glass plate is obtained by casting, this might result in the orientation of polymer chains. Then this oriented configuration was immediately fixed during the phase inversion. Just like annealing, an aggressive solvent rather than heat increases the possibility of polymer chain movement, providing a chance for these oriented polymer chains to change their configuration into a stable state. In the relaxation process, the O-PASS chains relax from an oriented state. This would lead to the expansion of PASS chains which will squeeze pores, eliminating defects. Therefore, the polymer chain relaxation process in solvent can eliminate these defects in the membrane and make the membrane more uniform, increasing the RB rejection. In addition, the solvent molecules penetrate into the PASS chains, creating more channels for water to permeate, which increases the permeability of the PASS membrane.

From the above measurements, it can be concluded that the chemical stability of PASS membranes is greatly improved by the oxidation process. The oxidized PASS membrane can endure a longtime immersion in NMP, and even in a very aggressive 98% H_2SO_4 solution. Unexpectedly, the filtration performance of oxidized PASS membranes was not deteriorated by $CHCl_3$, NMP and 98% H_2SO_4, but improved instead.

The enhancement of the chemical stability is mainly due to the changes of functional units in the PASS chain. At molecular level, PASS is built up by thioether groups, sulphone and benzene rings. The –S- bond has a bond length of 180 pm and a bond angle of 90°, which is relatively large and this gives more freedom for the PASS chain to move, while the polar sulfone units in PASS chain increase the intermolecular interaction of polymer chains. The oxidization process changes the -S- units into -SO_2- units, increasing the rigidity of polymer chains due to the elimination of -S- units and improving the intermolecular interaction of polymer chains because of the increase of -SO_2- groups. In addition, the smaller repeating unit in oxidized PASS chains creates a closer packing of polymer chains and forms an ordered aggregated structure (Fig. 6.8) [194]. These three factors make the solvent molecules difficult to attack the polymer and penetrate into the polymer, which yields a strong chemical stability.

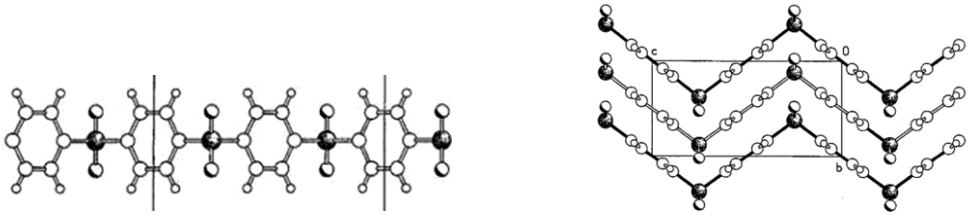


Fig. 6.8. The structure and three-dimensional simulation of the oxidized PASS molecule [194].

6.2.3 OSN performance of oxidized PASS membranes

The oxidized PASS has shown an excellent solvent resistance in the above experiments and is therefore a promising polymer to fabricate OSN membranes. Organic solvent nanofiltration using O-PASS membranes was performed. The PASS membranes were synthesized by using a PASS concentration of 24 wt%.

Solvent permeability and dye rejection

Table 3 illustrates the organic solvent fluxes of O-PASS membranes. Methanol, n-heptane, THF, toluene, DMF, NMP and IPA were chosen as the solvents to be tested because they have been extensively used in the pharmaceutical industry. The solvent transport mechanism in OSN has been extensively studied and debated in the last decades [202, 203] as the OSN process is more intricate than aqueous nanofiltration. The solvent flux strongly depends on the solvent viscosity, and molar volume. From the results in Table 6.2, it can be seen that O-PASS membranes have a relatively high methanol and THF permeability due to the low viscosity of these two solvents. Although n-heptane has the lowest viscosity, the permeability is not the highest because of its large molar volume. Similarly, toluene has almost the same viscosity as methanol and THF, but the permeability is much lower than for these two solvents due to its large molar volume. IPA has the highest viscosity and the lowest permeability. According to the prediction and modeling by Bhanushali et al. [202], the solvent flux is proportional to the ratio of the molar volume to solvent viscosity, as indicated in Fig. 6.9. However,

the permeability of n-heptane, methanol and toluene does not fit this modeling, because the interactions between the solvents and membranes are not included in this modeling. It is well accepted that the interactions between the solvents and membranes also play an important role in solvent transport process. Methanol with a viscosity of $0.54x10^{-3}$ Pa.S and solubility parameter due to dipole force (δ_p) of 12.3 $MPa^{½}$) exhibits the second highest permeability of 5.88 L h^{-1} m^{-2} bar^{-1}, while the relatively nonpolar heptane and toluene show a low permeability.

Table 6.2 Physico-chemical properties of solvents used and the O-PASS membrane permeability of these solvents.

Solvent	Viscosity (cP)	V_{vdW} [a] (A^3)[204]	V_m [a]/Viscosity (cm^3 mol^{-1} cP^{-1})	Solubility parameter (δp $MPa^{½}$)	Permeability (L h^{-1} m^{-2} bar^{-1})
n-heptane	0.39	129.6	377.9	0	2.36
Methanol	0.54	34.6	75.4	12.3	5.88
THF	0.55	74.2	148.5	5.7	5.97
Toluene	0.56	98.4	190.7	1.4	2.64
DMF	0.82	77.6	93.9	13.7	2.67
NMP	1.67	99.8	57.8	12.3	0.97
IPA	2	69.2	38.4	6.1	0.79

[a] van der **Waals volume**

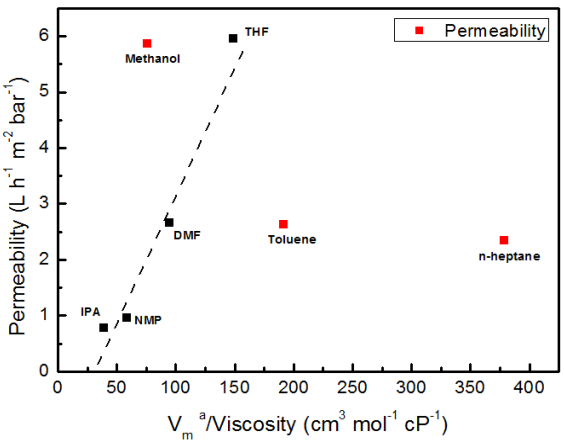


Fig. 6.9. Plot of solvent permeances against the combined solvent property (viscosity, Molar volume) for O-PASS membrane.

The O-PASS membranes not only show high stability in these solvents, but also have a high DMF permeability. As shown in Table 6.3, compared to the recently published results, the O-PASS membrane has a much larger DMF permeability, which may due to the unique chemical structure. In addition, the rejection of O-PASS membrane was measured by using six different dyes, of which the chemical structure and properties are listed in Table 2.5. The dye rejection results are presented in Fig. 6.10a, in which it can be seen that the O-PASS membrane has a high rejection (above 95%) for RB, EB, RO16 and SBB.

Table 6.3 Comparison of various OSN membranes in DMF.

Membrane type	Permeability ($L\ m^{-2}\ h^{-1}\ bar^{-1}$)	Marker	Marker MW ($g\ mol^{-1}$)	Rejection (%)	Ref
O-PASS	2.67	Sudan black B	456.54	98%	This study
PAH/PAA	0.55	Rose Bengal	1017	97%	[205]
Cross-linked PAI	0.9	Rose Bengal	1017	98.6%	[26]
PM-C	0.7	Styrene oligomer	600	90%	[206]
AEMA-10 μm	0.3	Rose Bengal	1017	97%	[207]
TFC-MPD-NP	1.54	styrene oligomer	around 300	99%	[208]
MMM membranes	0.20	styrene oligomer	236	90%	[209]

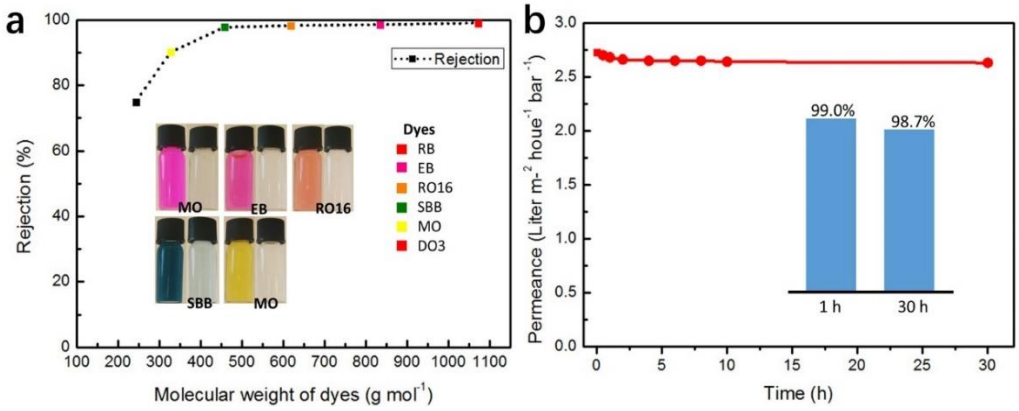


Fig. 6.10. (a) Rejection of O-PASS membrane in dye DMF solution. (b) Permeability of DMF as a function of time. (Operation pressure, 6 bars; Temperature, 25°).

30 hours stability

In order to evaluate the solvent stability of oxidized PASS membranes for a relatively long time in an aggressive solvent, filtration of pure DMF was studied for an extended period of time (about 30 h). From Fig. 6.10b, it can be concluded that the permeability decreased significantly in the first hour of filtration, indicating the strong interaction between the membrane and DMF. The compaction due to the high pressure also contributed to the loss of permeability. After the first hour of filtration, the membrane shows a stable performance. In addition, the RB rejection of oxidized PASS also kept stable. These results indicate that the oxidized PASSS membrane exhibit a very good stability in DMF in 30 hours.

6.3. Conclusion

In summary, an approach different than crosslinking to improve the chemical stability of polymer was demonstrated, by increasing the intermolecular interaction of polymer chains, polymer chain rigidity and chain packing density PASS via a simple oxidization process. More specifically, after oxidization, the -S- units in PASS polymer chain were changed into -SO_2- units, giving the O-PASS polymer chain a higher intermolecular interaction and become more rigid. The chemical reaction during the oxidization process was analyzed by FT-IR and XPS and the change of -S- into –SO_2- in PASS chain was confirmed. Moreover, the pure water permeability, RB rejection and hydrophilicity of O-PASS membranes was improved. Most importantly, the O-PASS membrane shows an excellent chemical stability in aggressive organic solvents and even in 98% H_2SO_4. During organic solvent filtration, O-PASS membranes exhibited a high rejection of RB, EB, RO16 and SBB, a high DMF permeability compared to other reported membranes and a good 30 hours stability in organic solvent filtration. These good performances will make the O-PASS become a promising polymer in organic solvent nanofiltration.

Chapter 7

Facile synthesis of Kevlar nanofibrous membranes via regeneration of hydrogen bonds for organic solvent nanofiltration

Adapted from: Shushan Yuan, Jasper Swartenbroekx, Yi Li, Junyong Zhu, Frederik Ceyssens, Ruijun Zhang, Alexander Volodine, Jian Li, Peter Van Puyvelde, Bart Van der Bruggen, Facile synthesis of Kevlar nanofibrous membranes via regeneration of hydrogen bonds for organic solvent nanofiltration.

7.1 Introduction

With the growing demand for medicines to cure new or unsolved diseases, high-tech electronic products and low-cost energy resources, an increasing amount of various solvents is consumed every year in the pharmaceutical industry, in electronics and in the petrochemical industry. This generates a large amount of waste solvents, posing a great threat to the environment [210]. Membrane science, specifically organic solvent nanofiltration (OSN), is a green process in terms of its high efficiency, low energy consumption and operational stability, and thus has played an important role in the purification and reuse of solvents [88, 94, 211, 212]. OSN membranes are applied to separate organics from solvents with a molecular weight cut-off ranging from 200 to 1000 Da, and pore sizes in the range of 0.5 to 2.0 nm [88-90]. It is emerging as an efficient separation technology in chemical processes such as catalyst recovery, solvent recycling and organics extraction [213-217].

Polymeric OSN membranes are of interest because of their relatively low cost and ease of scaling up. A polymeric OSN membrane is “green” in terms of the OSN process,

however, its fabrication process is complex and often based on the use of toxic and volatile solvents, which are not "green" [218, 219]. Generally, polymers applied to synthesize OSN membranes should be solvent resistant [220]. The most commonly used strategies to improve the solvent resistance of a polymeric membrane is crosslinking. Interfacial polymerization combined with a crosslinking reaction is a prominent method to fabricate OSN membranes. This method involves the fabrication and crosslinking of ultrafiltration membrane for supporting, and interfacial polymerization of a highly crosslinked polyamide separation layer for permselectivity [1]. This complicated process consumes a large amount of solvent and various crosslinking chemicals, leading to the growth of fabrication cost and environmental problems. Fabrication of OSN membranes from cross-linkable polymers including PI, P84, PEEK, PBI and PASS [221] is another strategy. However, the large amount of toxic and aggressive solvents like n-methyl-2-pyrrolidone (NMP), dimethylacetamide (DMAC), dimethylformamide (DMF) and H_2SO_4 for the preparation of the dope solution and various cross-linking agents to improve the solvent resistance properties, would also result in a relatively high fabrication cost, and associated environmental and toxicological problems [222]. Therefore, in order to lower the membrane fabrication cost and the negative environmental impact, it is of importance to synthesize OSN membranes via an easier way and a simpler process by using greener solvents.

Kevlar threads or poly(p-phenylene terephthalamide) are well-known for their application in body armors and ultra-strong para-aramid synthetic macroscale fibers with a high tensile strength-to-weight ratio [223-225]. On the one hand, Kevlar has an excellent chemical resistance in harsh environments and a high resistance to the most commonly used solvents because of the large amount of intermolecular hydrogen bonds, and can only be dissolved in concentrated H_2SO_4, which makes it a perfect polymer for the fabrication of solvent resistant membranes. On the other hand, the use of aggressive concentrated H_2SO_4 as solvent to prepare dope solutions greatly hinders the application of Kevlar in the field of membrane technology. For example, the first study about solvent resistant Kevlar membranes was reported in 1980, when Zschocke et al.

fabricated solvent resistant Kevlar ultrafiltration membranes by dissolving Kevlar in concentrated H_2SO_4 [226]. After this, there was no further study about solvent resistant Kevlar membranes reported for around 35 years until 2015. The study reported in this year investigated the influence of SiO_2 nanoparticles on the performance of Kevlar ultrafiltration membranes by using H_2SO_4 again as solvent [227]. The use of strongly corrosive H_2SO_4 as solvent in the membrane fabrication not only makes the membrane fabrication process not "green", but also entails a high safety risk, hindering the application of Kevlar in the field of membrane technology. Therefore, the synthesis of solvent resistant Kevlar membranes by using a greener and noncorrosive solvent would be a substantial improvement in the development of Kevlar into membranes.

Recent research found that Kevlar threads can be split into nanoscale fibers through the weakening of hydrogen bonds combined with a strengthening of the electrostatic repulsion between the polymer chains in DMSO with KOH [228, 229]. Although the Kevlar threads cannot be dissolved on molecular scale and exist as nanofibers rather than polymer chains in the DMSO solution, this method provides a possible way to obtain a homogeneous Kevlar dope solution by using DMSO as a greener solvent, compared to concentrated H_2SO_4, and other toxic and aggressive solvent like NMP, DMAC, DMF. This would greatly lower the negative environmental impact and safety risk of preparing Kevlar homogeneous dope solutions. It is believed that the application of this method to prepare a dope solution for membrane fabrication, compared to the use of concentrated H_2SO_4, would greatly improve the development of Kevlar into membranes.

Kevlar dope solutions containing nanofibers rather than polymer chains are uncommon compared to the traditional membrane fabrication process, but this might give the obtained membrane additional value. Recently, nanofibers have attracted much attention in the field of membrane fabrication. Ultrathin nonporous ultrafiltration membranes fabricated through filtration of cellulose nanofiber dispersion on an alumina support were reported [230]. These membranes were found to have a very high flux

compared to other traditional membranes. When these nanofiber membranes were used as the support membrane to perform interfacial polymerization, the nanofiltration membrane obtained also showed a high permeation [231]. These studies proved that high performance membranes can be fabricated by applying nanofibers in membrane fabrication. Kevlar nanofibers have already been obtained in the literature, as mentioned before [228, 229]; however, the fabrication of membranes from Kevlar nanofibers has not yet been reported. Besides, nanofiber porous membranes are normally fabricated by filtration of nanofibers on a support membrane. Synthesis of nanofiber membranes from nanofibers solution via the formation of a nanofiber hydrogel during phase inversion remains unknown. Therefore, the fabrication of Kevlar membranes from Kevlar nanofibers solution by the formation of hydrogel during phase inversion would be new and interesting in the field of membrane technology.

Solvent resistant Kevlar membranes were already fabricated albeit with using aggressive concentrated H_2SO_4. However, the reported solvent resistant Kevlar membrane is in the range of ultrafiltration and generally organic solvent nanofiltration is the most common application for solvent resistant membranes. In this case, the synthesis of nanofiltration Kevlar membranes is crucial for the application of Kevlar in membrane technology. However, Kevlar nanofiltration membranes have not yet been reported. Many strategies can be used to fabricate an OSN nanofiltration membrane: interfacial polymerization, increasing the concentration of polymer dope solution and layer by layer assembly. Nevertheless, these relatively complicated processes would increase the cost of membrane fabrication by using a large amount of solvents and various reactive chemicals. Furthermore, none of them can transform an ultrafiltration membrane into a nanofiltration membrane without using additional chemicals.

In this chapter, Kevlar hydrogel ultrafiltration membranes were fabricated from Kevlar nanofiber solution using greener DMSO-KOH/water mixture compared to the aggressive concentrated H_2SO_4. Then, by a simple thermal treatment to induce the regeneration of hydrogen bonds between nanofibers, thin OSN Kevlar membranes were

obtained from Kevlar hydrogel ultrafiltration membranes without consuming additional chemicals. To achieve the best membrane performance in OSN, the influence of the Kevlar concentration and thickness on the performance of Kevlar OSN membranes was investigated. This chapter is expected to open a new window in the fabrication of Kevlar membranes by using a greener solvent, especially compared to concentrated H_2SO_4. This will greatly lower the negative environmental impact and safety risk of preparing Kevlar dope solutions. In addition, the application of a Kevlar dope solution containing nanofibers rather than polymer chains to synthesize a membrane remains unknown and should be interesting in the field of membrane technology. Most importantly, this facile and green way of transforming a Kevlar ultrafiltration membrane into a Kevlar nanofiltration membrane without consuming additional chemicals is expected to greatly lower the membrane fabrication cost.

7.2 Results and discussion

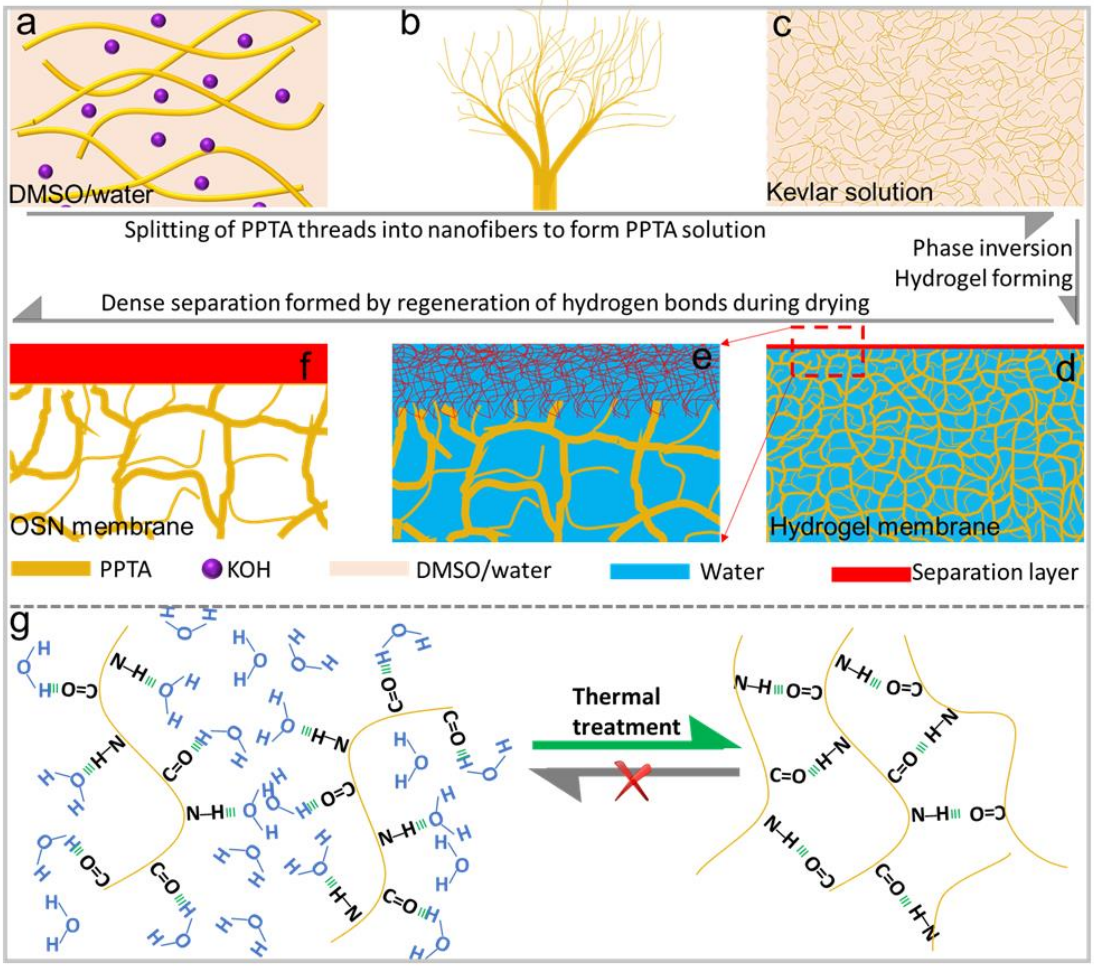


Fig. 7.1 Schematic illustration of Kevlar OSN membrane synthesis: (a) Kevlar threads in DMSO-KOH/water (40:1); (b) The splitting of Kevlar threads into nanofibers by breaking the hydrogen bonds via KOH and DMSO/water; (c) The formation of Kevlar dope solution containing Kevlar nanofibers; (d) hydrogel membranes formed by the phase inversion; (e) The nanofibers in the separation layer of hydrogel membranes; (f) Kevlar membranes formed by the regeneration of hydrogen bonds during the thermal treatment; (g)The formation of hydrogen bonds during thermal treatment

7.2.1 Kevlar Nanofiber, Kevlar hydrogel membrane

Fig. 7.1 is the schematic illustration of the Kevlar OSN membrane fabrication process and the mechanism involved. Kevlar threads were immersed in a DMSO-KOH/H_2O (Fig. 7.1a) solution with KOH for the splitting of threads into nanofibers (Fig. 7.1b) by

breaking the hydrogens bonds, thus forming a homogeneous Kevlar solution containing nanofibers (Fig. 7.1c). The KOH in the mixtures is likely to abstract the mobile hydrogen from >NH groups, substantial reduce of the strength of hydrogen bonds between the polymer chains, improving the splitting of PPTA into nanofibers [228, 232]. The water would promote the dispersion of KOH in the solvent [232]. Then, the Kevlar dope solution was casted on a glass plate with a given thickness to form a solution film. The thin film was then immersed in deionized water to induce the phase inversion. At the same time, the intermediate immersion with water is expected to regenerate the H+ on the aramid macromolecules (removed by KOH) via seizing protons from water [228, 229], forming hydrogel membrane (Fig. 7.1d and Fig. 7.1e). This process is accompanied by a color change from dark red to translucent**.** A photograph of a Kevlar hydrogel membrane is presented in Fig. 7.4a. It was found that this hydrogel membrane is soft and translucent. In order to preserve the macro-structure of the Kevlar hydrogel membrane during the drying process, supercritical CO_2 drying was applied. As shown in Fig. 7.4b, 7.4c, 7.4d and 7.4e, these hydrogel membranes consisted of a dense hydrogel dense layer and a relatively porous supporting layer composed of branched Kevlar nanofiber networks. A large number of nanofibers could be spotted in the bottom surface of the Kevlar hydrogel membrane, indicating the presence of Kevlar nanofibers. However, the top surface is very dense. This dense hydrogen top layer was formed immediately by the solidification of small nanofibers with water when the Kevlar solution contacted the water. Once the dense hydrogel separation layer was formed, the phase inversion of the dope solution under this layer became slow because the penetration of water through this separation layer was more difficult. This gives the nanofibers more time to aggregate to form larger branched nanofiber networks during the phase inversion before the solidification of the dope solution, finally resulting a nanofibrous supporting layer. After a careful observation of the nanofiber networks (Fig.7.2) in different positions of the membrane cross-section, it was found that the diameter of fibers in the top, middle and bottom (M2%-200) are almost the same (32 nm) (Fig. 7.4f). However, the diameter of Kevlar fibers in the network can be influenced

by the concentration of Kevlar in the dope solution. Based on the morphology of nanofibers in the cross-section of Kevlar membranes (Fig. 7.3), the diameter of these fibers was obtained. As shown in SEM Fig. 7.4g, when the concentration of the Kevlar in the dope solution was lowered from 2% to 1%, the diameter of the fibers decreased from 33.5 nm to 23.3 nm. This is because a higher concentration could lead to more aggregation of nanofibers during the phase inversion.

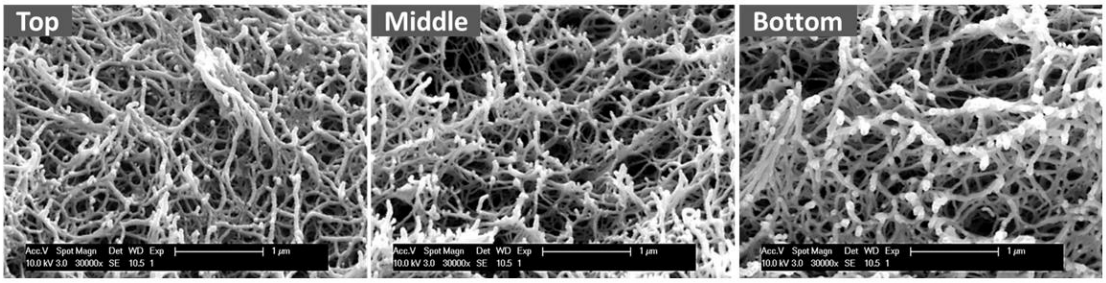


Fig. 7.2 Kevlar nanofiber networks in the top, middle and bottom of the hydrogel membrane (2%-200).

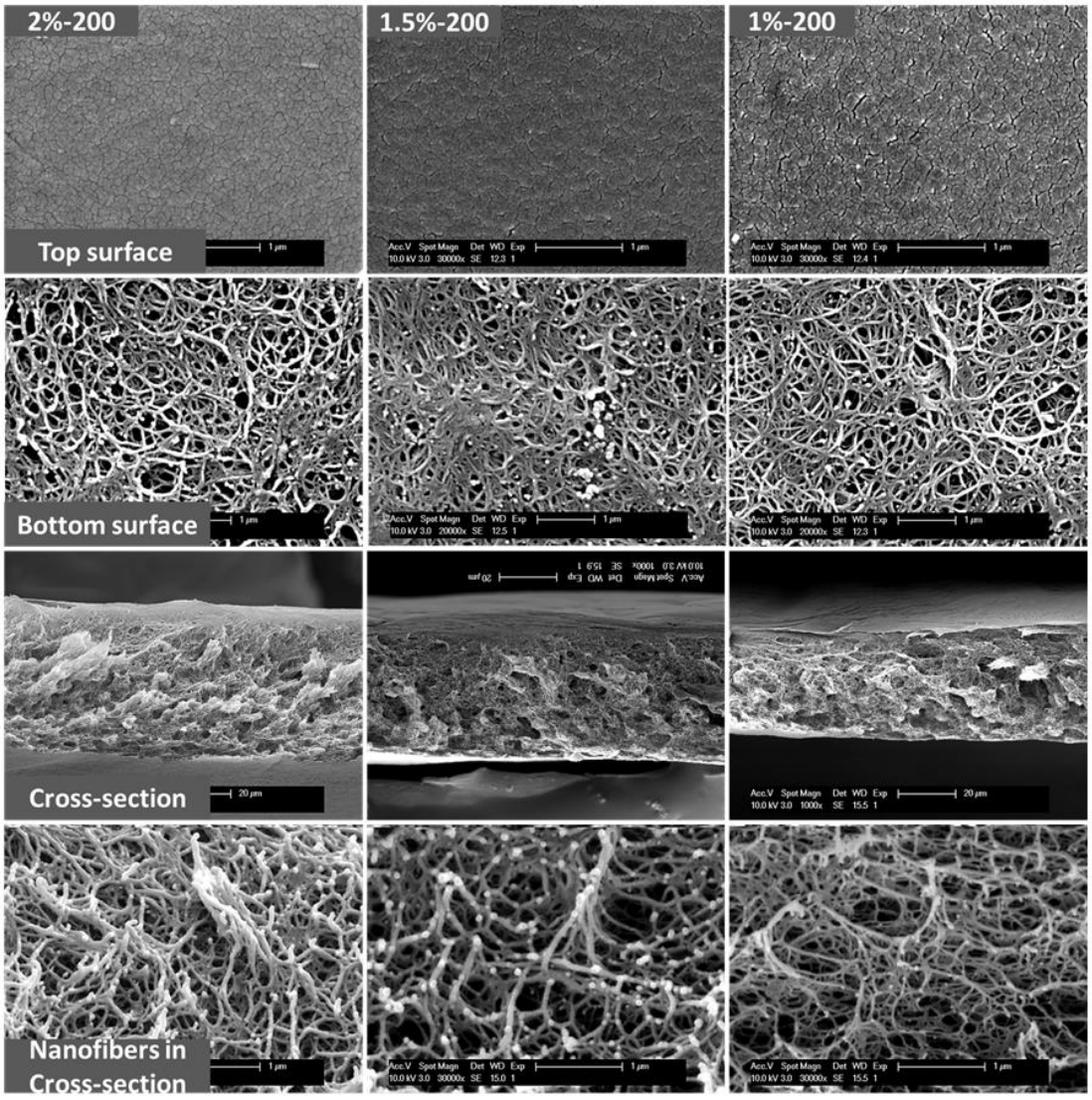


Fig. 7.3 Top surface, bottom surface, cross-section and nanofibers morphology of hydrogel membrane 1%-200, 1.5%-200 and 2%-200.

As a kind of hydrogel membrane, related properties like water content, swelling ratio and water permeation, were measured. As shown in Fig. 7.4h, the hydrogel membranes have a water content over 96% and a swelling ratio of over 30, indicating the high porosity of these membranes. More specifically, when the concentration of Kevlar decreased from 2% to 1%, the water content rose from 96.8% to 98.3% and the swelling ratio increased from 30 to 56. In addition, when the concentration of Kevlar increased from 1% to 2%, the pure water permeation decreased from 709 L/ (m^2 h bar) to 453 L/ (m^2 h bar) while the rejection of BSA was still over 99%, suggesting that these hydrogel membranes are in the range of ultrafiltration (fig. 7.4i).

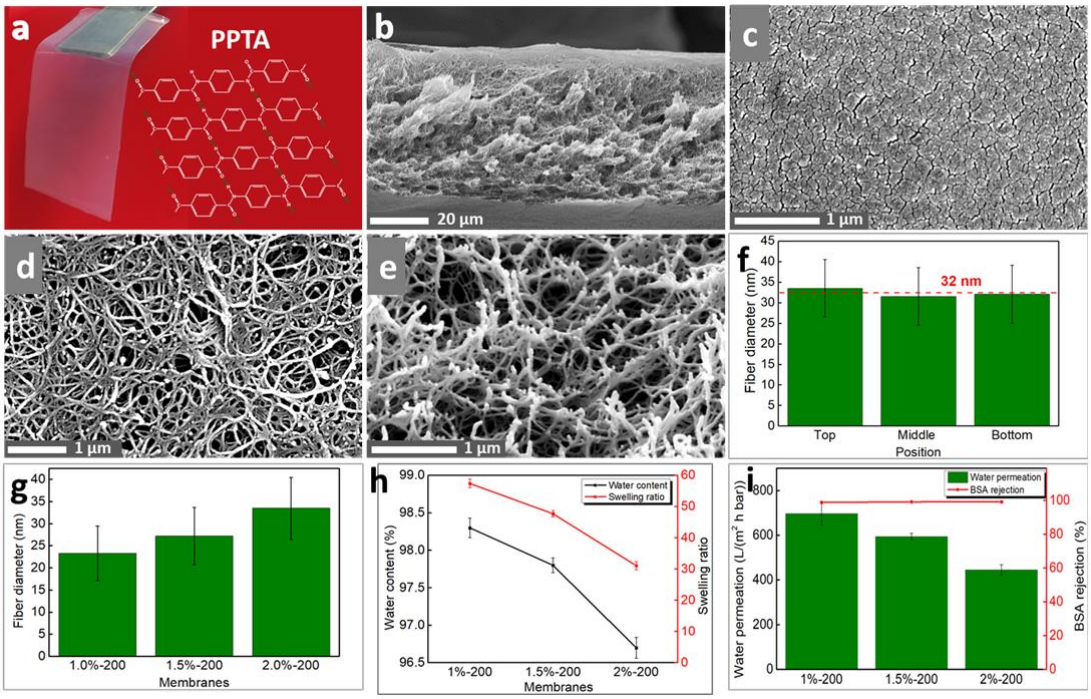


Fig. 7.4 (a) photograph of Kevlar hydrogel membrane; Cross-section (b), top surface (c) and bottom surface (d) morphology of hydrogel membrane; (e) Kevlar nanofiber networks in hydrogel membrane; (f) Diameter of nanofibers in top, middle and bottom of M2%-200 hydrogel membrane based on SEM in Fig. 7.2; (g) Mean diameter of nanofibers in hydrogel membranes M1%-200, M1.5%-200 and M2%-200 based on the cross-section images in Fig. 7.3; (h) Water content and swelling ratio of hydrogel membranes M1%-200, M1.5%-200 and M2%-200; (i) Water permeation and BSA rejection of hydrogel membranes M1%-200, M1.5%-200 and M2%-200

7.2.2 Morphology of Kevlar OSN membranes

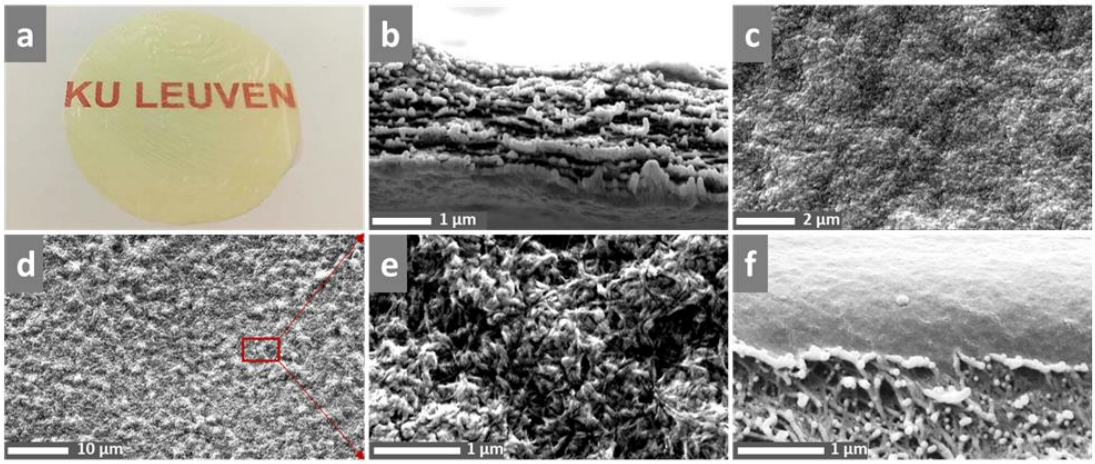


Fig. 7.5 (a) Photograph of Kevlar membrane; Cross-section (b), top surface (c) and bottom surface (d) morphology of Kevlar membranes; (e) Magnified surface morphology of the bottom layer; (f) Thin separation layer of Kevlar membrane.

Transparent light brown solvent resistance Kevlar membranes (Fig. 7.5a) were fabricated through a simple thermal treatment in an oven at 60 ºC for 12 h (Fig. 7.1f). During thermal treatment, the large amount of free water in the supporting hydrogel layer was evaporated and formed a relatively porous supporting layer consisting of many layers of nanofibers (Fig. 7.5b). The bottom surface (Fig. 7.5d) of this supporting layer is rough and composed of many obvious embossments. A magnified image (Fig. 7.5e) shows that theses embossments result from the aggregation of Kevlar nanofibers. For the top hydrogel layer of hydrogel membrane, the distances between small nanofibers are small, as the top layer is dense. Then when the water interacted with the surface of small nanofibers by hydrogen bonds and the free water between small nanofibers was evaporated, a large amount of carbonyl groups and N-H centers on the surface of Kevlar small nanofibers was exposed to each other, while the distance between carbonyl groups and N-H centers was narrowed due to the evaporation of water in between. These two factors greatly promoted the regeneration of hydrogen bonds between small nanofibers, leading to the coalescence of small nanofibers into one dense separation layer (Fig. 7.5c). This separation layer has a thickness as low as 80 nm (Fig. 7.5f), which would greatly lower the resistance when water goes through. In addition,

the thin Kevlar membrane cannot change back to a hydrogel membrane when it is immersed in water because the regenerated hydrogen bonds cannot be broken by water, indicating that this process is irreversible. Most importantly, the regenerated hydrogen bonds cannot be broken by most commonly used solvents, endowing the obtain Kevlar nanofiltration membrane with solvent resistant properties.

The influence of the dope solution concentration and thickness of the hydrogel membrane on the morphology of Kevlar membranes was investigated. As shown in Fig. 7.6, with the increase of the dope solution concentration from 1% to 2% and increasing the thickness of the hydrogel membrane from 20 μm to 200 μm, the thickness of the Kevlar membranes increased from 0.84 μm to 1.78 μm and from 0.3 μm to 1.78 μm, respectively. At the same time, the top surface of these membranes becomes rougher, which was confirmed by the AFM measurements. In the AFM images (Fig. 7.7), all of these membranes exhibited a very rough surface with peaks and valleys. The surface roughness values of the membranes on 5 × 5 μm^2 scans, such as, mean root square roughness (R_{rms}), average roughness (R_a), and the maximum vertical difference between the highest and lowest points (R_m), are listed in Table 7.1. As demonstrated by the roughness values, the average roughness value increased from 18.9 nm to 51.4 nm when the concentration of Kevlar increased from 1% to 2% and augmented from 10.5 to 51.4 nm when the thickness of the hydrogel membranes increased from 60 μm to 200 μm.

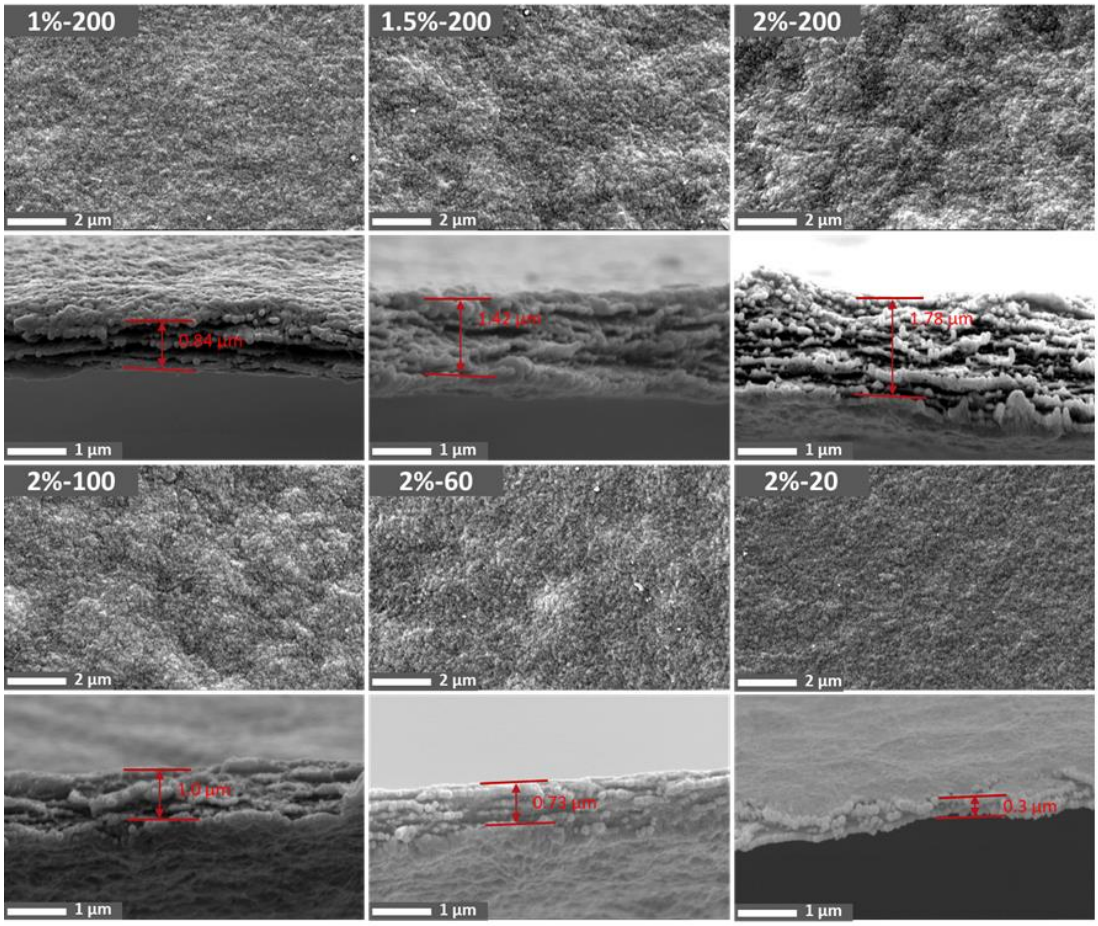


Fig. 7.6 Top surface and cross-section morphology of membranes (M1%-200, M1.5%-200, M2%-200, M2%-100, M2%-60, M2%-20).

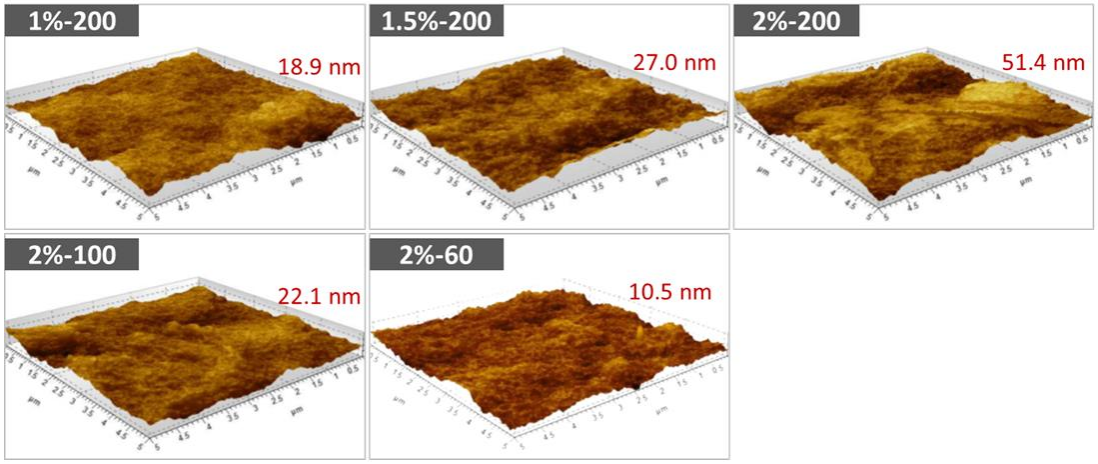


Fig. 7.7 AFM top surface morphology of Kevlar membranes (M1%-200, M1.5%-200, M2%-200, M2%-100, M2%-60, M2%-20).

Table 7.1 AFM surface roughness of Kevlar membranes: average roughness (Ra), root mean square roughness (Rrms), and maximum vertical difference between the highest and lowest points (Rm).

Membrane	R_a (nm)	R_{rms} (nm)	R_m (nm)
1%-200	18.9	24.5	216
1.5%-200	27.0	34.2	251
2%-200	51.4	63.8	368
2%-100	22.1	27.6	214
2%-60	10.5	13.4	133

7.2.3 Performance of nanofiltration membranes

The performance of these dry Kevlar membranes was evaluated by the filtration of dye/ethanol solutions in a cross-flow setup. As shown in Fig. 7.8a and Fig. 7.8b, membrane M2%-200 has the highest rejection of Rose Bengal (95.4%) among these membranes with an ethanol permeation of 2.9 L/(m^2 bar h) (methanol, 7.6 L $m^{-2}bar^{-1}h^{-1}$; isopropanol, 3.1 $m^{-2}bar^{-1}h^{-1}$) which is far lower than its hydrogel membrane, indicating that the separation layer became much denser and the pore size was greatly narrowed after thermal treatment of the hydrogel membrane. Compared to OSN membranes fabricated by other polymers without further modification including Polyaniline (PANI), polyphenylsulfone (PPSU), crosslinked PI, (Table 7.2) the Kevlar membrane exhibited a better flux; only PBI membrane surpasses, which gives the Kevlar membrane a higher baseline for further modification to increase the performance. This relatively high flux could be attributed its nanofibrous structure. It was also found that this Kevlar nanofiltration membrane cannot swell in ethanol and maintains a relatively constant rejection of Rose Bengal and permeation of ethanol for 6 h (Fig. 7.8d), suggesting that a large amount of hydrogen bonds was generated in the separation layer when the water between small nanofibers was evaporated. These regenerated

hydrogen bonds endow these Kevlar membranes with a good solvent resistance, which can be further confirmed by the rejection changes after treatment of the membrane M2%-200 in different solvents for 7 days. As demonstrated in Table 7.3, membrane M2%-200 can still retain a good rejection of Rose Bengal over 94% after being treated by methanol, ethanol, IPA, hexane and CCl_4 for 7 days. In addition, the effect of the concentration of the dope solution and the thickness of the gel membranes on the rejection and the permeation of the dye solution was investigated. More specifically, the reduction of the concentration in the dope solution from 2% to 1% and the hydrogel membrane thickness from 200 μm to 20 μm would lead to a decline of Rose Bengal rejection from 95.4% to 90.7% and from 95.5% to 64.8% respectively, while the permeation of the dye solution increased from 2.9 L/(m^2 h bar) to 5.5 L/(m^2 h bar) and from 2.9 L/(m^2 h bar) to 39.7 L/(m^2 h bar), respectively. This is because the decrease of dope solution and hydrogel thickness would yield a less dense separation layer and cause many defects in the separation layer. In addition, dyes with molecular weight ranging from 327 g mol^{-1} to 1018 g mol^{-1} were applied to investigate the rejection of membrane M2%-200. It was observed that this membrane has a relatively good rejection of RB, EB and EY (over 90%), while PBVF and MO could not be rejected (Fig. 7.8c). Based on these filtration results, it is safe to conclude that Kevlar organic solvent nanofiltration membranes were fabricated through the regeneration of hydrogen bonds between nanofibers by using DMSO as a greener solvent.

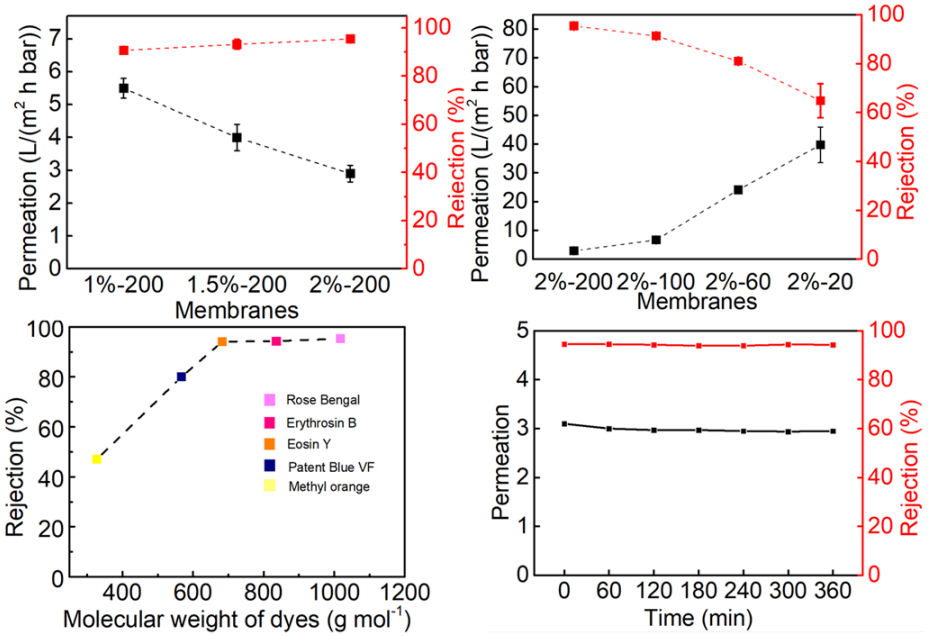


Fig. 7.8 (a) Rose Bengal rejection and ethanol permeation of Kevlar membranes fabricated from different concentration; (b) Rose Bengal rejection and ethanol permeation of Kevlar membranes fabricated from hydrogel membranes with different thickness; (c) Rejection of different dyes in ethanol for membrane M2%-200; (d) The Rose Bengal rejection and ethanol permeation of membrane M2%-200 during 6h.

Table 7.2 Performance of OSN membranes fabricated by various polymers through phase inversion without modification.

Membrane	Solvent	Permeance ($L\ m^{-2}h^{-1}bar^{-1}$)	Marker	Marker MW ($g\ mol^{-1}$)	Rejection (%)	ref
Kevlar	Ethanol Methanol Isopropanol	2.9 7.6 3.1	RB	1017	95.4%	This study
Crosslinked PANI	Methanol	0.8	SO[1]	300	95	[233]
PPSU	Ethanol	0.23	RB	1017	64	[198]
cross-linked PI	Isopropanol	1.4	RB	1017	96%	[234]
PBI	Ethanol	3.7	BBR[2]	826	99%	[215]

1 Styrene oligomers; 2 Brilliant Blue R

Table 7.3 RB rejection of Kevlar membranes after being treated with different solvents for 7 days

Solvents	Methanol	Ethanol	IPA	Hexane	CCl_4
Rejection (%)	94.1± 1	94.4± 1.5	94.1±0.9	94.4± 0.8	94.0±1.4

7.3 Conclusions

Through a simple and green thermal treatment by using a greener solvent, thin Kevlar membranes for organic solvent nanofiltration were fabricated in this chapter. First, a homogeneous Kevlar dope solution was prepared by a greener solvent mixture of DMSO-KOH/water in place of the highly corrosive concentrated H_2SO_4. Then, Kevlar hydrogel membranes were synthesized from the dope solution containing Kevlar nanofibers. These hydrogel Kevlar membranes are in the range of ultrafiltration, and have a pure water flux over 450 L/(m^2 h bar) and a BSA rejection over 99%. Finally, a facile thermal treatment in oven at 60 ºC for 12 h was applied to transform the hydrogel ultrafiltration membrane into solvent resistant nanofiltration membrane without consuming additional solvents and crosslinking agents by the regeneration of hydrogen bonds. The influence of dope solution and thickness of hydrogel membrane on the performance of OSN membrane was studied. Results show that the increase of the Kevlar concentration and hydrogel membrane thickness would result in an increase in the dye rejection and a reduction in permeation. Thus, membrane M2%-200 has the best performance with a rejection of Rose Bengal of 95.4% and with an ethanol permeation of 2.9 L/(m^2 bar h), outperforming most other polymeric OSN membranes prepared from phase inversion. Besides, Kevlar OSN membranes exhibit an excellent solvent resistance in commonly used solvents. They maintain a relatively constant dye rejection during the filtration of dye solutions for 6 hours and retain dye rejection over 94% after being treated by different solvents for 7 days. This chapter not only describes a facile way of synthesizing Kevlar OSN membrane from a dope solution containing

nanofibers, but also enables the fabrication and application of Kevlar threads in membranes by a non-corrosive and green solvent. Therefore, this chapter may open up new insights and strategies to develop Kevlar into nanofiltration membranes.

Chapter 8

Conclusions and recommendations for future research

8.1 General conclusions

Membrane technology has attracted great attention in academic and commercial environments as one of the most promising alternatives to conventional separation processes due to its low energy consumption, high separation efficiency, low investment and environmentally friendliness. Almost all kinds of polymeric membranes have been fabricated by the combination of different polymers and various synthesis methods. However, membranes fabricated by currently used methods and polymers cannot solve all the problems encountered in industry. Novel fabrication methods with ability to control the structure and surface roughness of a membrane for oil/water separation are still demanded. New polymers with high solvent stability are also highly needed for the fabrication of OSN membranes. In this thesis, selective laser sintering was explored as a novel membrane fabrication method to synthesize a porous membrane. In addition, two high-performance polymers, PASS and Kevlar, were used to prepare OSN membranes. The obtained membranes were characterized and their performance was measured. The detailed conclusions are as follows:

1) Various porous membranes were fabricated from PA and PSU powder by selective laser sintering. Processing parameters have an effective control over the structure of these membranes. A membrane fabricated with higher ED, like a larger laser power, a smaller hatch space and 2 counts, would have a denser structure and a lower water flux. On the contrary, a porous membrane could be obtained by a lower laser power, a larger hatch space and 1 laser scanning count. Membranes synthesized with 2 scanning count and a laser power higher than 5 W are relatively dense and have no water flux.

2) Two superhydrophobic modification methods, candle soot coating and ZIF-L

deposition, were applied on these 3D printed membranes. In the first method, through an immersion of a 3D printed PSU membrane in candle soot/hexane solution for 40 mins, an ordered loose network was formed on the PSU membrane surface, endowing the membrane with superhydrophobic and superoleophilic properties. In the second method, by constructing a micro/nano-structural ZIF-L layer on a 3D printed porous PA membrane and the following PDMS coating, a superhydrophobic and super-oleophilic membrane was fabricated. This membrane exhibited a sliding water contact angle as low as 1.56 º and a static water contact angle as high as 159 º. Two types of 3-dimensional ZIF-L were synthesized in this process. The first one is a macroscale ZIF-L with leaf-crossed structure obtained by increasing the concentration of reactant. The second one is a micro/nano-structural ZIF-L designed by a second growth of nanoscale flat rod-shape and needle-like ZIF-Ls on the leaf-crossed ZIF-L.

3) The two obtained superhydrophobic membranes demonstrated an excellent performance in oil/water separation. As to the superhydrophobic PSU membrane, when it was applied to the oil/water separation, this membrane was found to have a high separation efficiency for oil from an oil/water mixture. In addition, after it was rinsed by water, this membrane showed a superoleophobic property and could separate water from an oil/water mixture. This candle soot coated membrane showed a separation efficiency over 99% for all of hexane/water separation in the 10 cycles. The superhydrophobic PA porous membrane exhibits a high oil rejection (over 99%) and a high oil flux (over 24000 L/ (m^2 h)) when it was applied in oil/water separation.

4) An oxidized PASS membrane with high solvent resistance was obtained by a post oxidation treatment. This membrane showed an excellent chemical stability in aggressive organic solvents even in 98% H_2SO_4 due to the significantly improved intermolecular interactions. During organic solvent filtration, O-PASS membranes exhibited a high rejection of RB, EB, RO16 and SBB, a high DMF permeability

compared to other reported membranes and a good 30 hours stability in organic solvent filtration.

5) A hydrogel-based Kevlar nanofiltration membrane was synthesized. Through a simple thermal treatment, an OSN Kevlar membrane was fabricated from a Kevlar hydrogel ultrafiltration membrane via the regeneration of hydrogen bonds. This membrane exhibited a rejection of Rose Bengal of 95.4% and an ethanol permeation of 2.9 L/ (m^2 bar h), outperforming most other polymeric OSN membranes prepared from phase inversion. Furthermore, the Kevlar OSN membrane exhibited an excellent solvent resistance in commonly used solvents. It maintained a relatively constant dye rejection during the filtration of dye solutions for 6 hours and retains a dye rejection of over 94% after being treated by different solvents for 7 days.

8.2 Recommendations for future research

In consideration of the experiments and conclusions in this thesis, several recommendations can be made for future research.

1) In this thesis, selective laser sintering was explored as a novel membrane fabrication method. However, the printed membranes normally have a relatively large pore size due to the low resolution of this technique, limiting the obtained membranes to few applications. Therefore, the exploration of membrane fabrication methods by using high resolution 3D printing techniques like two-photon polymerization would be meaningful.

2) The obtained superhydrophobic membranes in this thesis can only be used to separate an oil/water mixture rather than an emulsion, because of the large pore size. Therefore, fabrication of a superhydrophobic membrane with relatively small pore size to separate the oil/water emulsion is worthy to explore in the future.

3) Chapter 6 describes the fabrication of a PASS OSN membrane without nonwoven

support. Thus, the mechanical strength of this membrane is not very high. Therefore, the fabrication of a solvent resistant PASS on nonwoven in pilot scale would be useful for its further application in industry.

4) In Chapter 7, Kevlar threads were developed into an OSN nanofiltration membrane by using a greener solvent instead of the concentrated H_2SO_4. This study is a starting point but needs further elaboration. Much more work needs to be done in the future to improve its performance.

Reference

[1] P. Marchetti, M.F. Jimenez Solomon, G. Szekely, A.G. Livingston, Molecular separation with organic solvent nanofiltration: a critical review, Chem Rev, 114 (2014) 10735-10806.

[2] S.P. Nunes, K.-V. Peinemann, Membrane technology: in the chemical industry, John Wiley & Sons, 2006.

[3] J.F. Jenck, F. Agterberg, M.J. Droescher, Products and processes for a sustainable chemical industry: a review of achievements and prospects, Green Chemistry, 6 (2004) 544-556.

[4] J.A. Veil, Produced water management options and technologies, in: Produced Water, Springer, 2011, pp. 537-571.

[5] A. Anglada, A. Urtiaga, I. Ortiz, Contributions of electrochemical oxidation to waste-water treatment: fundamentals and review of applications, Journal of Chemical Technology & Biotechnology, 84 (2009) 1747-1755.

[6] M. Cheryan, N. Rajagopalan, Membrane processing of oily streams. Wastewater treatment and waste reduction, J. Membr. Sci., 151 (1998) 13-28.

[7] A. Hounslow, Water quality data: analysis and interpretation, CRC press, 2018.

[8] P.M. Gschwend, Environmental organic chemistry, John Wiley & Sons, 2016.

[9] H. Zhu, D. Chen, N. Li, Q. Xu, H. Li, J. He, J. Lu, Graphene foam with switchable oil wettability for oil and organic solvents recovery, Adv. Funct. Mater., 25 (2015) 597-605.

[10] J.M. Dickhout, J. Moreno, P. Biesheuvel, L. Boels, R.G. Lammertink, W.M. de Vos, Produced water treatment by membranes: a review from a colloidal perspective, J. Colloid Interface Sci., 487 (2017) 523-534.

[11] M. Ardi, M. Aroua, N.A. Hashim, Progress, prospect and challenges in glycerol

purification process: a review, Renewable and Sustainable Energy Reviews, 42 (2015) 1164-1173.

[12] S. Alzahrani, A.W. Mohammad, Challenges and trends in membrane technology implementation for produced water treatment: A review, Journal of Water Process Engineering, 4 (2014) 107-133.

[13] S.S. Shenvi, A.M. Isloor, A. Ismail, A review on RO membrane technology: developments and challenges, Desalination, 368 (2015) 10-26.

[14] V.K. Thakur, S.I. Voicu, Recent advances in cellulose and chitosan based membranes for water purification: a concise review, Carbohydr. Polym., 146 (2016) 148-165.

[15] I. Wenten, Reverse osmosis applications: prospect and challenges, Desalination, 391 (2016) 112-125.

[16] A. Giwa, N. Akther, A. Al Housani, S. Haris, S.W. Hasan, Recent advances in humidification dehumidification (HDH) desalination processes: improved designs and productivity, Renewable and Sustainable Energy Reviews, 57 (2016) 929-944.

[17] B. Belaissaoui, J. Claveria-Baro, A. Lorenzo-Hernando, D.A. Zaidiza, E. Chabanon, C. Castel, S. Rode, D. Roizard, E. Favre, Potentialities of a dense skin hollow fiber membrane contactor for biogas purification by pressurized water absorption, J. Membr. Sci., 513 (2016) 236-249.

[18] M. Fernández, R. Wagterveld, S. Ahualli, F. Liu, A. Delgado, H. Hamelers, Polyelectrolyte-versus membrane-coated electrodes for energy production by capmix salinity exchange methods, J. Power Sources, 302 (2016) 387-393.

[19] S. Prasertkulsak, C. Chiemchaisri, W. Chiemchaisri, T. Itonaga, K. Yamamoto, Removals of pharmaceutical compounds from hospital wastewater in membrane bioreactor operated under short hydraulic retention time, Chemosphere, 150 (2016) 624-631.

[20] B.S. Lalia, V. Kochkodan, R. Hashaikeh, N. Hilal, A review on membrane fabrication: Structure, properties and performance relationship, Desalination, 326 (2013) 77-95.

[21] K.P. Lee, T.C. Arnot, D. Mattia, A review of reverse osmosis membrane materials for desalination—development to date and future potential, J. Membr. Sci., 370 (2011) 1-22.

[22] P. Wang, J. Ma, F. Shi, Y. Ma, Z. Wang, X. Zhao, Behaviors and effects of differing dimensional nanomaterials in water filtration membranes through the classical phase inversion process: a review, Industrial & Engineering Chemistry Research, 52 (2013) 10355-10363.

[23] L.Y. Ng, A.W. Mohammad, C.P. Leo, N. Hilal, Polymeric membranes incorporated with metal/metal oxide nanoparticles: a comprehensive review, Desalination, 308 (2013) 15-33.

[24] N. Peng, N. Widjojo, P. Sukitpaneenit, M.M. Teoh, G.G. Lipscomb, T.-S. Chung, J.-Y. Lai, Evolution of polymeric hollow fibers as sustainable technologies: past, present, and future, Progress in Polymer Science, 37 (2012) 1401-1424.

[25] Q.H. Nguyen, M. Ali, S. Nasir, W. Ensinger, Transport properties of track-etched membranes having variable effective pore-lengths, Nanotechnology, 26 (2015) 485502.

[26] S.K. Lim, L. Setiawan, T.H. Bae, R. Wang, Polyamide-imide hollow fiber membranes crosslinked with amine-appended inorganic networks for application in solvent-resistant nanofiltration under low operating pressure, J. Membr. Sci., 501 (2016) 152-160.

[27] L.E.M. Gevers, I.F.J. Vankelecom, P.A. Jacobs, Solvent-resistant nanofiltration with filled polydimethylsiloxane (PDMS) membranes, J. Membr. Sci., 278 (2006) 199-204.

[28] L.S. Wan, Z.K. Xu, X.J. Huang, A.F. Che, Z.G. Wang, A novel process for the post-treatment of polyacrylonitrile-based membranes: Performance improvement and

possible mechanism, J. Membr. Sci., 277 (2006) 157-164.

[29] M. Dalwani, G. Bargeman, S.S. Hosseiny, M. Boerrigter, M. Wessling, N.E. Benes, Sulfonated poly(ether ether ketone) based composite membranes for nanofiltration of acidic and alkaline media, J. Membr. Sci., 381 (2011) 81-89.

[30] I.B. Valtcheva, S.C. Kumbharkar, J.F. Kim, Y. Bhole, A.G. Livingston, Beyond polyimide: Crosslinked polybenzimidazole membranes for organic solvent nanofiltration (OSN) in harsh environments, J. Membr. Sci., 457 (2014) 62-72.

[31] D.Y. Xing, S.Y. Chan, T.S. Chung, The ionic liquid [EMIM]OAc as a solvent to fabricate stable polybenzimidazole membranes for organic solvent nanofiltration, Green Chemistry, 16 (2014) 1383-1392.

[32] R.W. Baker, U.b. Staff, Membrane technology, Kirk-Othmer Encyclopedia of Chemical Technology, (2000).

[33] P.M. Bungay, Transport principles-porous membranes, in: Synthetic Membranes: Science, Engineering and Applications, Springer, 1986, pp. 109-153.

[34] A.F. Ismail, L.P. Yean, Review on the development of defect-free and ultrathin-skinned asymmetric membranes for gas separation through manipulation of phase inversion and rheological factors, J. Appl. Polym. Sci., 88 (2003) 442-451.

[35] P. Radovanovic, S.W. Thiel, S.-T. Hwang, Formation of asymmetric polysulfone membranes by immersion precipitation. Part I. Modelling mass transport during gelation, J. Membr. Sci., 65 (1992) 213-229.

[36] D.R. Lloyd, K.E. Kinzer, H. Tseng, Microporous membrane formation via thermally induced phase separation. I. Solid-liquid phase separation, J. Membr. Sci., 52 (1990) 239-261.

[37] J. Zhao, G. Luo, J. Wu, H. Xia, Preparation of microporous silicone rubber membrane with tunable pore size via solvent evaporation-induced phase separation, ACS Appl. Mater. Interfaces, 5 (2013) 2040-2046.

[38] C.-L. Li, D.-M. Wang, A. Deratani, D. Quémener, D. Bouyer, J.-Y. Lai, Insight into the preparation of poly (vinylidene fluoride) membranes by vapor-induced phase separation, J. Membr. Sci., 361 (2010) 154-166.

[39] I. Pinnau, B. Freeman, Formation and modification of polymeric membranes: overview, Membrane Formation and Modification, 744 (2000) 1-22.

[40] F. Liu, N.A. Hashim, Y. Liu, M.M. Abed, K. Li, Progress in the production and modification of PVDF membranes, J. Membr. Sci., 375 (2011) 1-27.

[41] H. Strathmann, K. Kock, P. Amar, R. Baker, The formation mechanism of asymmetric membranes, Desalination, 16 (1975) 179-203.

[42] C. Smolders, A. Reuvers, R. Boom, I. Wienk, Microstructures in phase-inversion membranes. Part 1. Formation of macrovoids, J. Membr. Sci., 73 (1992) 259-275.

[43] M. Ulbricht, Advanced functional polymer membranes, Polymer, 47 (2006) 2217-2262.

[44] I.C. Kim, H.G. Yoon, K.H. Lee, Formation of integrally skinned asymmetric polyetherimide nanofiltration membranes by phase inversion process, J. Appl. Polym. Sci., 84 (2002) 1300-1307.

[45] H. Kim, R. Tyagi, A. Fouda, K. Ionasson, The kinetic study for asymmetric membrane formation via phase-inversion process, J. Appl. Polym. Sci., 62 (1996) 621-629.

[46] Q.-Z. Zheng, P. Wang, Y.-N. Yang, D.-J. Cui, The relationship between porosity and kinetics parameter of membrane formation in PSF ultrafiltration membrane, J. Membr. Sci., 286 (2006) 7-11.

[47] M. Amirilargani, E. Saljoughi, T. Mohammadi, M. Moghbeli, Effects of coagulation bath temperature and polyvinylpyrrolidone content on flat sheet asymmetric polyethersulfone membranes, Polym. Eng. Sci., 50 (2010) 885-893.

[48] S.X. Liu, J.-T. Kim, Characterization of surface modification of polyethersulfone

membrane, J. Adhes. Sci. Technol., 25 (2011) 193-212.

[49] A.S. More, S.K. Pasale, P.P. Wadgaonkar, Synthesis and characterization of polyamides containing pendant pentadecyl chains, Eur. Polym. J., 46 (2010) 557-567.

[50] P. Buch, D.J. Mohan, A. Reddy, Preparation, characterization and chlorine stability of aromatic–cycloaliphatic polyamide thin film composite membranes, J. Membr. Sci., 309 (2008) 36-44.

[51] J. Mulder, Basic principles of membrane technology, Springer Science & Business Media, 2012.

[52] G.R. Guillen, Y. Pan, M. Li, E.M. Hoek, Preparation and characterization of membranes formed by nonsolvent induced phase separation: a review, Industrial & Engineering Chemistry Research, 50 (2011) 3798-3817.

[53] T.A. Otitoju, A.L. Ahmad, B.S. Ooi, Recent advances in hydrophilic modification and performance of polyethersulfone (PES) membrane via additive blending, RSC Advances, 8 (2018) 22710-22728.

[54] L. Shi, R. Wang, Y. Cao, D.T. Liang, J.H. Tay, Effect of additives on the fabrication of poly (vinylidene fluoride-co-hexafluropropylene)(PVDF-HFP) asymmetric microporous hollow fiber membranes, J. Membr. Sci., 315 (2008) 195-204.

[55] E. Fontananova, J.C. Jansen, A. Cristiano, E. Curcio, E. Drioli, Effect of additives in the casting solution on the formation of PVDF membranes, Desalination, 192 (2006) 190-197.

[56] H.J. Lee, J. Won, H. Lee, Y.S. Kang, Solution properties of poly (amic acid)–NMP containing LiCl and their effects on membrane morphologies, J. Membr. Sci., 196 (2002) 267-277.

[57] J.-H. Kim, K.-H. Lee, Effect of PEG additive on membrane formation by phase inversion, J. Membr. Sci., 138 (1998) 153-163.

[58] Y. Liu, G. Koops, H. Strathmann, Characterization of morphology controlled

polyethersulfone hollow fiber membranes by the addition of polyethylene glycol to the dope and bore liquid solution, J. Membr. Sci., 223 (2003) 187-199.

[59] S.-H. Chen, R.-M. Liou, J.-Y. Lai, C.-L. Lai, Effect of the polarity of additional solvent on membrane formation in polysulfone/N-methyl-2-pyrrolidone/water ternary system, Eur. Polym. J., 43 (2007) 3997-4007.

[60] B. Jung, J.K. Yoon, B. Kim, H.-W. Rhee, Effect of molecular weight of polymeric additives on formation, permeation properties and hypochlorite treatment of asymmetric polyacrylonitrile membranes, J. Membr. Sci., 243 (2004) 45-57.

[61] I. Wienk, R. Boom, M. Beerlage, A. Bulte, C. Smolders, H. Strathmann, Recent advances in the formation of phase inversion membranes made from amorphous or semi-crystalline polymers, J. Membr. Sci., 113 (1996) 361-371.

[62] L.S. Wan, Z.K. Xu, Z.G. Wang, Leaching of PVP from polyacrylonitrile/PVP blending membranes: a comparative study of asymmetric and dense membranes, J. Polym. Sci., Part B: Polym. Phys., 44 (2006) 1490-1498.

[63] J. Dechnik, J. Gascon, C.J. Doonan, C. Janiak, C.J. Sumby, Mixed-Matrix Membranes, Angew. Chem. Int. Ed., 56 (2017) 9292-9310.

[64] Z. Kang, Y. Peng, Y. Qian, D. Yuan, M.A. Addicoat, T. Heine, Z. Hu, L. Tee, Z. Guo, D. Zhao, Mixed matrix membranes (MMMs) comprising exfoliated 2D covalent organic frameworks (COFs) for efficient CO2 separation, Chem. Mater., 28 (2016) 1277-1285.

[65] M. Aroon, A. Ismail, T. Matsuura, M. Montazer-Rahmati, Performance studies of mixed matrix membranes for gas separation: a review, Separation and purification Technology, 75 (2010) 229-242.

[66] R.J. Gohari, E. Halakoo, N. Nazri, W. Lau, T. Matsuura, A. Ismail, Improving performance and antifouling capability of PES UF membranes via blending with highly hydrophilic hydrous manganese dioxide nanoparticles, Desalination, 335 (2014) 87-95.

[67] J. Cadotte, R. Petersen, R. Larson, E. Erickson, A new thin-film composite seawater reverse osmosis membrane, Desalination, 32 (1980) 25-31.

[68] J. Cadotte, R. Forester, M. Kim, R. Petersen, T. Stocker, Nanofiltration membranes broaden the use of membrane separation technology, Desalination, 70 (1988) 77-88.

[69] W. Lau, A. Ismail, N. Misdan, M. Kassim, A recent progress in thin film composite membrane: a review, Desalination, 287 (2012) 190-199.

[70] C.H. Park, Viscosity Effect of Organic Solvent on the Fabrication of Polyamide Thin Film Composite Membrane via Interfacial Polymerization, POLYMER-KOREA, 40 (2016) 954-959.

[71] L. Li, S. Zhang, X. Zhang, G. Zheng, Polyamide thin film composite membranes prepared from 3, 4′, 5-biphenyl triacyl chloride, 3, 3′, 5, 5′-biphenyl tetraacyl chloride and m-phenylenediamine, J. Membr. Sci., 289 (2007) 258-267.

[72] T. Kawaguchi, H. Tamura, Chlorine-resistant membrane for reverse osmosis. I. Correlation between chemical structures and chlorine resistance of polyamides, J. Appl. Polym. Sci., 29 (1984) 3359-3367.

[73] F. Sadeghi, A. Ajji, P.J. Carreau, Analysis of microporous membranes obtained from polypropylene films by stretching, J. Membr. Sci., 292 (2007) 62-71.

[74] F. Sadeghi, Development of microporous polypropylene by stretching, 2007.

[75] F. Sadeghi, A. Ajji, P.J. Carreau, Analysis of row nucleated lamellar morphology of polypropylene obtained from the cast film process: effect of melt rheology and process conditions, Polym. Eng. Sci., 47 (2007) 1170-1178.

[76] F. Sadeghi, A. Ajji, P.J. Carreau, Microporous membranes obtained from polypropylene blends with superior permeability properties, J. Polym. Sci., Part B: Polym. Phys., 46 (2008) 148-157.

[77] H. Noether, I. Hay, Small-angle X-ray diffraction studies and morphology of microporous materials and their'hard'elastic precursors, J. Appl. Crystallogr., 11 (1978)

546-547.

[78] S. Wu, C. Lei, Q. Cai, R. Xu, B. Hu, W. Shi, X. Peng, Study of structure and properties of polypropylene microporous membrane by hot stretching, Polym. Bull., 71 (2014) 2205-2217.

[79] R.L. Fleischer, P.B. Price, R.M. Walker, R.M. Walker, Nuclear tracks in solids: principles and applications, Univ of California Press, 1975.

[80] M.E. Toimil-Molares, Characterization and properties of micro-and nanowires of controlled size, composition, and geometry fabricated by electrodeposition and ion-track technology, Beilstein journal of nanotechnology, 3 (2012) 860.

[81] D.H. Reneker, I. Chun, Nanometre diameter fibres of polymer, produced by electrospinning, Nanotechnology, 7 (1996) 216.

[82] X. Wang, B.S. Hsiao, Electrospun nanofiber membranes, Current opinion in chemical engineering, 12 (2016) 62-81.

[83] D. Li, Y. Xia, Electrospinning of nanofibers: reinventing the wheel?, Adv. Mater., 16 (2004) 1151-1170.

[84] Z. Li, C. Wang, Effects of working parameters on electrospinning, in: One-dimensional nanostructures, Springer, 2013, pp. 15-28.

[85] L.M.M. Costa, R.E.S. Bretas, R. Gregorio, Effect of solution concentration on the electrospray/electrospinning transition and on the crystalline phase of PVDF, Materials Sciences and Applications, 1 (2010) 247.

[86] C.L. Casper, J.S. Stephens, N.G. Tassi, D.B. Chase, J.F. Rabolt, Controlling surface morphology of electrospun polystyrene fibers: effect of humidity and molecular weight in the electrospinning process, Macromolecules, 37 (2004) 573-578.

[87] M. Buonomenna, J. Bae, Organic solvent nanofiltration in pharmaceutical industry, Separation & Purification Reviews, 44 (2015) 157-182.

[88] J. Liu, D. Hua, Y. Zhang, S. Japip, T.S. Chung, Precise Molecular Sieving

Architectures with Janus Pathways for Both Polar and Nonpolar Molecules, Adv. Mater., 30 (2018) 1705933.

[89] F. Fei, L. Cseri, G. Szekely, C.F. Blanford, Robust Covalently Cross-linked Polybenzimidazole/Graphene Oxide Membranes for High-Flux Organic Solvent Nanofiltration, ACS Appl. Mater. Interfaces, 10 (2018) 16140-16147.

[90] A. Zhou, C. Shi, X. He, Y. Fu, A.W. Anjum, J. Zhang, W. Li, Polyarylester nanofiltration membrane prepared from monomers of vanillic alcohol and trimesoyl chloride, Separation and Purification Technology, 193 (2018) 58-68.

[91] A. Volkov, S. Tsarkov, M. Gokzhaev, G. Bondarenko, S. Legkov, Y.A. Kukushkina, V. Volkov, Nanofiltration and sorption of organic solvents in poly (1-trimethylsilyl-1-propyne) samples of different microstructures, Petroleum Chemistry, 52 (2012) 598-608.

[92] K. Vanherck, A. Aerts, J. Martens, I. Vankelecom, Hollow filler based mixed matrix membranes, Chem. Commun., 46 (2010) 2492-2494.

[93] K. Hendrix, M. Van Eynde, G. Koeckelberghs, I.F. Vankelecom, Crosslinking of modified poly (ether ether ketone) membranes for use in solvent resistant nanofiltration, J. Membr. Sci., 447 (2013) 212-221.

[94] S. Karan, Z. Jiang, A.G. Livingston, Sub–10 nm polyamide nanofilms with ultrafast solvent transport for molecular separation, Science, 348 (2015) 1347-1351.

[95] C. Yap, C. Chua, Z. Dong, Z. Liu, D. Zhang, L. Loh, S. Sing, Review of selective laser melting: Materials and applications, Applied physics reviews, 2 (2015) 041101.

[96] S.F.S. Shirazi, S. Gharehkhani, M. Mehrali, H. Yarmand, H.S.C. Metselaar, N.A. Kadri, N.A.A. Osman, A review on powder-based additive manufacturing for tissue engineering: selective laser sintering and inkjet 3D printing, Science and Technology of Advanced Materials, 16 (2015) 033502.

[97] C.M.B. Ho, S.H. Ng, Y.-J. Yoon, A review on 3D printed bioimplants, International

Journal of Precision Engineering and Manufacturing, 16 (2015) 1035-1046.

[98] G.N. Levy, R. Schindel, J.-P. Kruth, Rapid manufacturing and rapid tooling with layer manufacturing (LM) technologies, state of the art and future perspectives, CIRP Annals-Manufacturing Technology, 52 (2003) 589-609.

[99] J.-P. Kruth, M.-C. Leu, T. Nakagawa, Progress in additive manufacturing and rapid prototyping, Cirp Annals, 47 (1998) 525-540.

[100] K.V. Wong, A. Hernandez, A review of additive manufacturing, ISRN Mechanical Engineering, 2012 (2012).

[101] S.V. Murphy, A. Atala, 3D bioprinting of tissues and organs, Nat. Biotechnol., 32 (2014) 773.

[102] E. Ngai, K.K. Moon, F.J. Riggins, Y.Y. Candace, RFID research: An academic literature review (1995–2005) and future research directions, International Journal of Production Economics, 112 (2008) 510-520.

[103] V. Kostakis, V. Niaros, C. Giotitsas, Open source 3D printing as a means of learning: An educational experiment in two high schools in Greece, Telematics and informatics, 32 (2015) 118-128.

[104] P. Tseng, C. Murray, D. Kim, D. Di Carlo, Research highlights: printing the future of microfabrication, Lab on a Chip, 14 (2014) 1491-1495.

[105] M. Vaezi, H. Seitz, S. Yang, A review on 3D micro-additive manufacturing technologies, The International Journal of Advanced Manufacturing Technology, 67 (2013) 1721-1754.

[106] F.P. Melchels, J. Feijen, D.W. Grijpma, A review on stereolithography and its applications in biomedical engineering, Biomaterials, 31 (2010) 6121-6130.

[107] H. Bikas, P. Stavropoulos, G. Chryssolouris, Additive manufacturing methods and modelling approaches: a critical review, The International Journal of Advanced Manufacturing Technology, 83 (2016) 389-405.

[108] B. Dhariwala, E. Hunt, T. Boland, Rapid prototyping of tissue-engineering constructs, using photopolymerizable hydrogels and stereolithography, Tissue Eng., 10 (2004) 1316-1322.

[109] D. Dean, E. Mott, X. Luo, M. Busso, M.O. Wang, C. Vorwald, A. Siblani, J.P. Fisher, Multiple initiators and dyes for continuous Digital Light Processing (cDLP) additive manufacture of resorbable bone tissue engineering scaffolds: A new method and new material to fabricate resorbable scaffold for bone tissue engineering via continuous Digital Light Processing, Virtual and Physical Prototyping, 9 (2014) 3-9.

[110] J.M. Williams, A. Adewunmi, R.M. Schek, C.L. Flanagan, P.H. Krebsbach, S.E. Feinberg, S.J. Hollister, S. Das, Bone tissue engineering using polycaprolactone scaffolds fabricated via selective laser sintering, Biomaterials, 26 (2005) 4817-4827.

[111] M. Khaing, J. Fuh, L. Lu, Direct metal laser sintering for rapid tooling: processing and characterisation of EOS parts, J. Mater. Process. Technol., 113 (2001) 269-272.

[112] A.K. Sood, R.K. Ohdar, S.S. Mahapatra, Parametric appraisal of mechanical property of fused deposition modelling processed parts, Materials & Design, 31 (2010) 287-295.

[113] A.K. Sood, R. Ohdar, S.S. Mahapatra, Improving dimensional accuracy of fused deposition modelling processed part using grey Taguchi method, Materials & Design, 30 (2009) 4243-4252.

[114] B. Mueller, Additive manufacturing technologies–Rapid prototyping to direct digital manufacturing, Assembly Automation, 32 (2012).

[115] F. Li, W. Meindersma, A. De Haan, T. Reith, Novel spacers for mass transfer enhancement in membrane separations, J. Membr. Sci., 253 (2005) 1-12.

[116] T. Femmer, A.J. Kuehne, J. Torres-Rendon, A. Walther, M. Wessling, Print your membrane: Rapid prototyping of complex 3D-PDMS membranes via a sacrificial resist, J. Membr. Sci., 478 (2015) 12-18.

[117] T. Femmer, A.J. Kuehne, M. Wessling, Print your own membrane: direct rapid prototyping of polydimethylsiloxane, Lab on a Chip, 14 (2014) 2610-2613.

[118] T. Femmer, A.J. Kuehne, M. Wessling, Estimation of the structure dependent performance of 3-D rapid prototyped membranes, Chem Eng J, 273 (2015) 438-445.

[119] S. Badalov, Y. Oren, C.J. Arnusch, Ink-jet printing assisted fabrication of patterned thin film composite membranes, J. Membr. Sci., 493 (2015) 508-514.

[120] J.-Y. Lee, W.S. Tan, J. An, C.K. Chua, C.Y. Tang, A.G. Fane, T.H. Chong, The potential to enhance membrane module design with 3D printing technology, J. Membr. Sci., 499 (2016) 480-490.

[121] J. Li, R. Kang, X. Tang, H. She, Y. Yang, F. Zha, Superhydrophobic meshes that can repel hot water and strong corrosive liquids used for efficient gravity-driven oil/water separation, Nanoscale, 8 (2016) 7638-7645.

[122] M. Long, S. Peng, W. Deng, X. Miao, N. Wen, Q. Zhou, X. Yang, W. Deng, A robust superhydrophobic PDMS@ ZnSn (OH) 6 coating with under-oil self-cleaning and flame retardancy, J. Mater. Chem. A, 5 (2017) 22761-22771.

[123] L. Francis, N. Ghaffour, A.S. Alsaadi, S.P. Nunes, G.L. Amy, Performance evaluation of the DCMD desalination process under bench scale and large scale module operating conditions, J. Membr. Sci., 455 (2014) 103-112.

[124] V. Vatanpour, S.S. Madaeni, R. Moradian, S. Zinadini, B. Astinchap, Novel antibifouling nanofiltration polyethersulfone membrane fabricated from embedding TiO2 coated multiwalled carbon nanotubes, Separation and purification technology, 90 (2012) 69-82.

[125] J. Yang, H.-D. Wang, S.-X. Xu, G.-X. Li, Y.-J. Huang, Study on polymerization conditions and structure of poly (phenylene sulfide sulfone), J. Polym. Res., 12 (2005) 317-323.

[126] D. Lin, S. Jin, F. Zhang, C. Wang, Y. Wang, C. Zhou, G.J. Cheng, 3D

stereolithography printing of graphene oxide reinforced complex architectures, Nanotechnology, 26 (2015) 434003.

[127] A. Leong-Hoï, P.C. Montgomery, B. Serio, P. Twardowski, High speed implementation of a three-dimensional shape profiler with submillimeter precision using a digital light processing device and a new efficient algorithm for absolute phase retrieval, Optical Engineering, 54 (2015) 034102.

[128] M. Van den Eynde, L. Verbelen, P. Van Puyvelde, Assessing polymer powder flow for the application of laser sintering, Powder Technology, 286 (2015) 151-155.

[129] L. Verbelen, S. Dadbakhsh, M. Van den Eynde, J.-P. Kruth, B. Goderis, P. Van Puyvelde, Characterization of polyamide powders for determination of laser sintering processability, Eur. Polym. J., 75 (2016) 163-174.

[130] G. Wang, P. Wang, Z. Zhen, W. Zhang, J. Ji, Preparation of PA12 microspheres with tunable morphology and size for use in SLS processing, Materials & Design, 87 (2015) 656-662.

[131] S. Yuan, J. Wang, X. Wang, S. Long, G. Zhang, J. Yang, Poly (arylene sulfide sulfone) hybrid ultrafiltration membrane with TiO2-g-PAA nanoparticles: Preparation and antifouling performance, Polym. Eng. Sci., 55 (2015) 2829-2837.

[132] K.A. Arul, B.S. Rashia, G. Arumaikkannu, Investigation of Porosity Relationship in Additive Manufactured Novel Bone Scaffold, in: Applied Mechanics and Materials, Trans Tech Publ, 2014, pp. 836-841.

[133] Y. Han, S. Song, Y. Lu, D. Zhu, A method to modify PVDF microfiltration membrane via ATRP with low-temperature plasma pretreatment, Appl. Surf. Sci., 379 (2016) 474-479.

[134] S.R. Panda, S. De, Role of polyethylene glycol with different solvents for tailor-made polysulfone membranes, J. Polym. Res., 20 (2013) 179.

[135] R. Du, X. Gao, Q. Feng, Q. Zhao, P. Li, S. Deng, L. Shi, J. Zhang, Microscopic

dimensions engineering: stepwise manipulation of the surface wettability on 3d substrates for oil/water separation, Adv. Mater., 28 (2016) 936-942.

[136] Z. Xue, Y. Cao, N. Liu, L. Feng, L. Jiang, Special wettable materials for oil/water separation, J. Mater. Chem. A, 2 (2014) 2445-2460.

[137] Z. Chu, Y. Feng, S. Seeger, Oil/water separation with selective superantiwetting/superwetting surface materials, Angew. Chem. Int. Ed., 54 (2015) 2328-2338.

[138] B. Wang, W. Liang, Z. Guo, W. Liu, Biomimetic super-lyophobic and super-lyophilic materials applied for oil/water separation: a new strategy beyond nature, Chem. Soc. Rev., 44 (2015) 336-361.

[139] M. Joo, J. Shin, J. Kim, J.B. You, Y. Yoo, M.J. Kwak, M.S. Oh, S.G. Im, One-Step Synthesis of Cross-Linked Ionic Polymer Thin Films in Vapor Phase and Its Application to an Oil/Water Separation Membrane, J. Am. Chem. Soc., 139 (2017) 2329-2337.

[140] G. Lai, M. Yusob, W. Lau, R.J. Gohari, D. Emadzadeh, A. Ismail, P. Goh, A. Isloor, M.R.-D. Arzhandi, Novel mixed matrix membranes incorporated with dual-nanofillers for enhanced oil-water separation, Separation and Purification Technology, 178 (2017) 113-121.

[141] B. Cheng, Z. Li, Q. Li, J. Ju, W. Kang, M. Naebe, Development of smart poly (vinylidene fluoride)-graft-poly (acrylic acid) tree-like nanofiber membrane for pH-responsive oil/water separation, J. Membr. Sci., 534 (2017) 1-8.

[142] W.S. Tan, S.R. Suwarno, J. An, C.K. Chua, A.G. Fane, T.H. Chong, Comparison of solid, liquid and powder forms of 3D printing techniques in membrane spacer fabrication, J. Membr. Sci., 537 (2017) 283-296.

[143] W.S. Tan, C.K. Chua, T.H. Chong, A.G. Fane, A. Jia, 3D printing by selective laser sintering of polypropylene feed channel spacers for spiral wound membrane modules for the water industry, Virtual and Physical Prototyping, 11 (2016) 151-158.

[144] F. Zhang, W.B. Zhang, Z. Shi, D. Wang, J. Jin, L. Jiang, Nanowire-Haired Inorganic Membranes with Superhydrophilicity and Underwater Ultralow Adhesive Superoleophobicity for High-Efficiency Oil/Water Separation, Adv. Mater., 25 (2013) 4192-4198.

[145] J. Li, L. Yan, H. Li, W. Li, F. Zha, Z. Lei, Underwater superoleophobic palygorskite coated meshes for efficient oil/water separation, J. Mater. Chem. A, 3 (2015) 14696-14702.

[146] L. Feng, Z. Zhang, Z. Mai, Y. Ma, B. Liu, L. Jiang, D. Zhu, A super-hydrophobic and super-oleophilic coating mesh film for the separation of oil and water, Angew. Chem. Int. Ed., 43 (2004) 2012-2014.

[147] L.F. Dumée, H. Alglave, T. Chaffraix, B. Lin, K. Magniez, J. Schütz, Morphology-properties relationship of gas plasma treated hydrophobic meso-porous membranes and their improved performance for desalination by membrane distillation, Appl. Surf. Sci., 363 (2016) 273-285.

[148] T. Uragami, E. Fukuyama, T. Miyata, Selective removal of dilute benzene from water by poly (methyl methacrylate)-graft-poly (dimethylsiloxane) membranes containing hydrophobic ionic liquid by pervaporation, J. Membr. Sci., 510 (2016) 131-140.

[149] H. Shi, Y. He, Y. Pan, H. Di, G. Zeng, L. Zhang, C. Zhang, A modified mussel-inspired method to fabricate TiO 2 decorated superhydrophilic PVDF membrane for oil/water separation, J. Membr. Sci., 506 (2016) 60-70.

[150] J. Dong, Q. Wang, Y. Zhang, Z. Zhu, X. Xu, J. Zhang, A. Wang, Colorful Superamphiphobic Coatings with Low Sliding Angles and High Durability Based on Natural Nanorods, ACS Appl. Mater. Interfaces, 9 (2017) 1941-1952.

[151] B. Li, J. Zhang, Z. Gao, Q. Wei, Semitransparent superoleophobic coatings with low sliding angles for hot liquids based on silica nanotubes, J. Mater. Chem. A, 4 (2016) 953-960.

[152] J. Zhang, S. Seeger, Superoleophobe Silicon-Beschichtungen mit ultrakleinen Abrollwinkeln, Angew. Chem., 123 (2011) 6782-6786.

[153] S.W. Han, K.D. Kim, H.O. Seo, I.H. Kim, C.S. Jeon, J.E. An, J.H. Kim, S. Uhm, Y.D. Kim, Oil–Water Separation Using Superhydrophobic PET Membranes Fabricated Via Simple Dip-Coating Of PDMS–SiO2 Nanoparticles, Macromolecular Materials and Engineering, (2017).

[154] J. Sheng, Y. Xu, J. Yu, B. Ding, Robust Fluorine-Free Superhydrophobic Amino-Silicone Oil/SiO2 Modification of Electrospun Polyacrylonitrile Membranes for Waterproof-Breathable Application, ACS Appl. Mater. Interfaces, 9 (2017) 15139-15147.

[155] C.-H. Xue, Z.-D. Zhang, J. Zhang, S.-T. Jia, Lasting and self-healing superhydrophobic surfaces by coating of polystyrene/SiO 2 nanoparticles and polydimethylsiloxane, J. Mater. Chem. A, 2 (2014) 15001-15007.

[156] J. Li, Z. Zhao, D. Li, H. Tian, F. Zha, H. Feng, L. Guo, Smart candle soot coated membranes for on-demand immiscible oil/water mixture and emulsion switchable separation, Nanoscale, (2017).

[157] S. Yuan, D. Strobbe, J.-P. Kruth, P. Van Puyvelde, B. Van der Bruggen, Production of polyamide-12 membranes for microfiltration through selective laser sintering, J. Membr. Sci., 525 (2017) 157-162.

[158] Y. Feng, G. Han, T.-S. Chung, M. Weber, N. Widjojo, C. Maletzko, Effects of polyethylene glycol on membrane formation and properties of hydrophilic sulfonated polyphenylenesulfone (sPPSU) membranes, J. Membr. Sci., 531 (2017) 27-35.

[159] R.N. Wenzel, Resistance of solid surfaces to wetting by water, Ind. Eng. Chem., 28 (1936) 988-994.

[160] A. Cassie, S. Baxter, Wettability of porous surfaces, Trans. Faraday Soc., 40 (1944) 546-551.

[161] W. Choi, A. Tuteja, J.M. Mabry, R.E. Cohen, G.H. McKinley, A modified Cassie–Baxter relationship to explain contact angle hysteresis and anisotropy on non-wetting textured surfaces, J. Colloid Interface Sci., 339 (2009) 208-216.

[162] S. Liu, T. Zhu, R. Hu, Z. Liu, Evaporation-induced self-assembly of gold nanoparticles into a highly organized two-dimensional array, Physical Chemistry Chemical Physics, 4 (2002) 6059-6062.

[163] T.K. Sau, C.J. Murphy, Self-assembly patterns formed upon solvent evaporation of aqueous cetyltrimethylammonium bromide-coated gold nanoparticles of various shapes, Langmuir, 21 (2005) 2923-2929.

[164] J. Li, D. Li, Y. Yang, J. Li, F. Zha, Z. Lei, A prewetting induced underwater superoleophobic or underoil (super) hydrophobic waste potato residue-coated mesh for selective efficient oil/water separation, Green Chemistry, 18 (2016) 541-549.

[165] Z. Zhu, W. Wang, D. Qi, Y. Luo, Y. Liu, Y. Xu, F. Cui, C. Wang, X. Chen, Calcinable Polymer Membrane with Revivability for Efficient Oily-Water Remediation, Adv. Mater., (2018) 1801870.

[166] K. Jayaramulu, K.K.R. Datta, C. Rösler, M. Petr, M. Otyepka, R. Zboril, R.A. Fischer, Biomimetic Superhydrophobic/Superoleophilic Highly Fluorinated Graphene Oxide and ZIF-8 Composites for Oil–Water Separation, Angew. Chem. Int. Ed., 55 (2016) 1178-1182.

[167] Z. Xu, Y. Zhao, H. Wang, X. Wang, T. Lin, A Superamphiphobic Coating with an Ammonia-Triggered Transition to Superhydrophilic and Superoleophobic for Oil–Water Separation, Angew. Chem. Int. Ed., 54 (2015) 4527-4530.

[168] R. Blossey, Self-cleaning surfaces—virtual realities, Nat. Mater., 2 (2003) 301.

[169] W. Zhang, Z. Shi, F. Zhang, X. Liu, J. Jin, L. Jiang, Superhydrophobic and superoleophilic PVDF membranes for effective separation of water-in-oil emulsions with high flux, Adv. Mater., 25 (2013) 2071-2076.

[170] A. Ahmad, S. Ismail, S. Bhatia, Optimization of coagulation− flocculation process for palm oil mill effluent using response surface methodology, Environmental science & technology, 39 (2005) 2828-2834.

[171] Y. Zhu, J. Wang, F. Zhang, S. Gao, A. Wang, W. Fang, J. Jin, Zwitterionic Nanohydrogel Grafted PVDF Membranes with Comprehensive Antifouling Property and Superior Cycle Stability for Oil-in-Water Emulsion Separation, Adv. Funct. Mater., (2018) 1804121.

[172] X. Gao, J. Zhou, R. Du, Z. Xie, S. Deng, R. Liu, Z. Liu, J. Zhang, Robust superhydrophobic foam: a graphdiyne-based hierarchical architecture for oil/water separation, Adv. Mater., 28 (2016) 168-173.

[173] Y. Li, J. Wang, Y. Kong, J. Zhou, J. Wu, G. Wang, H. Bi, X. Wu, W. Qin, Q. Li, Micro/Nano hierarchical peony-like Al doped ZnO superhydrophobic film: The guiding effect of (100) preferred seed layer, Scientific reports, 6 (2016) 19187.

[174] D.J. Lee, H.M. Kim, Y.S. Song, J.R. Youn, Water droplet bouncing and superhydrophobicity induced by multiscale hierarchical nanostructures, ACS nano, 6 (2012) 7656-7664.

[175] J.H. Kim, A. Mirzaei, H.W. Kim, S.S. Kim, Superhydrophobic and oleophilic micro-nano hierarchical Pd-decorated SiO2 layers, J. Am. Ceram. Soc., 101 (2018) 3817-3829.

[176] Y. Lu, W. Yuan, Superhydrophobic three-dimensional porous ethyl cellulose absorbent with micro/nano-scale hierarchical structures for highly efficient removal of oily contaminants from water, Carbohydr. Polym., 191 (2018) 86-94.

[177] R.D. Farahani, M. Dubé, D. Therriault, Three-dimensional printing of multifunctional nanocomposites: manufacturing techniques and applications, Adv. Mater., 28 (2016) 5794-5821.

[178] J.J. Martin, B.E. Fiore, R.M. Erb, Designing bioinspired composite reinforcement architectures via 3D magnetic printing, Nature communications, 6 (2015) 8641.

[179] O. Shekhah, J. Liu, R. Fischer, C. Wöll, MOF thin films: existing and future applications, Chem. Soc. Rev., 40 (2011) 1081-1106.

[180] X. Cao, C. Tan, M. Sindoro, H. Zhang, Hybrid micro-/nano-structures derived from metal–organic frameworks: preparation and applications in energy storage and conversion, Chem. Soc. Rev., 46 (2017) 2660-2677.

[181] B. Chen, Z. Yang, Y. Zhu, Y. Xia, Zeolitic imidazolate framework materials: recent progress in synthesis and applications, J. Mater. Chem. A, 2 (2014) 16811-16831.

[182] Z. Zhong, J. Yao, R. Chen, Z. Low, M. He, J.Z. Liu, H. Wang, Oriented two-dimensional zeolitic imidazolate framework-L membranes and their gas permeation properties, J. Mater. Chem. A, 3 (2015) 15715-15722.

[183] R. Chen, J. Yao, Q. Gu, S. Smeets, C. Baerlocher, H. Gu, D. Zhu, W. Morris, O.M. Yaghi, H. Wang, A two-dimensional zeolitic imidazolate framework with a cushion-shaped cavity for CO 2 adsorption, Chem. Commun., 49 (2013) 9500-9502.

[184] P. Gorgojo, S. Karan, H.C. Wong, M.F. Jimenez-Solomon, J.T. Cabral, A.G. Livingston, Ultrathin polymer films with intrinsic microporosity: anomalous solvent permeation and high flux membranes, Adv. Funct. Mater., 24 (2014) 4729-4737.

[185] Y. Dong, B. Lin, J.E. Zhou, X. Zhang, Y. Ling, X. Liu, G. Meng, S. Hampshire, Corrosion resistance characterization of porous alumina membrane supports, Materials Characterization, 62 (2011) 409-418.

[186] G. Zhang, H.H. Ren, D.S. Li, S.R. Long, J. Yang, Synthesis of highly refractive and transparent poly(arylene sulfide sulfone) based on 4,6-dichloropyrimidine and 3,6-dichloropyridazine, Polymer (United Kingdom), 54 (2013) 601-606.

[187] L. Liu, X. Wang, Y. Wang, L. Li, K. Pan, J. Yang, B. Cao, Preparation and characterization of asymmetric polyarylene sulfide sulfone (PASS) solvent-resistant nanofiltration membranes, Mater Lett, 132 (2014) 11-14.

[188] S. Hermans, H. Mariën, C. Van Goethem, I.F. Vankelecom, Recent developments

in thin film (nano)composite membranes for solvent resistant nanofiltration, Current Opinion in Chemical Engineering, 8 (2015) 45-54.

[189] B.A. Miller-Chou, J.L. Koenig, A review of polymer dissolution, Progress in Polymer Science (Oxford), 28 (2003) 1223-1270.

[190] B. Medronho, A. Romano, M.G. Miguel, L. Stigsson, B. Lindman, Rationalizing cellulose (in)solubility: Reviewing basic physicochemical aspects and role of hydrophobic interactions, Cellulose, 19 (2012) 581-587.

[191] D.W. Van Krevelen, K. Te Nijenhuis, Properties of Polymers, 2009.

[192] D. Zierer, H. Scheckenbach, (2000).

[193] D. Fleischer, H. Strutz, J. Kulpe, A. Schleicher, (2000).

[194] H.M. Colquhoun, P.L. Aldred, F.H. Kohnke, P.L. Herbertson, I. Baxter, D.J. Williams, Crystal and molecular structures of poly(1,4-phenylenesulfone) and its trisulfone and tetrasulfone oligomers, Macromolecules, 35 (2002) 1685-1690.

[195] R. Noyori, M. Aoki, K. Sato, Green oxidation with aqueous hydrogen peroxide, Chem. Commun., 3 (2003) 1977-1986.

[196] Y. Liu, A. Bhatnagar, Q. Ji, J.S. Riffle, J.E. McGrath, J.F. Geibel, T. Kashiwagi, Influence of polymerization conditions on the molecular structure stability and physical behavior of poly(phenylene sulfide sulfone) homopolymers, Polymer, 41 (2000) 5137-5146.

[197] J. Yang, Polyphenylene Sulfide Resin and its Application, (2006) 35.

[198] S. Darvishmanesh, F. Tasselli, J.C. Jansen, E. Tocci, F. Bazzarelli, P. Bernardo, P. Luis, J. Degrève, E. Drioli, B. Van der Bruggen, Preparation of solvent stable polyphenylsulfone hollow fiber nanofiltration membranes, J. Membr. Sci., 384 (2011) 89-96.

[199] I.F.J. Vankelecom, K. De Smet, L.E.M. Gevers, A. Livingston, D. Nair, S. Aerts, S. Kuypers, P.A. Jacobs, Physico-chemical interpretation of the SRNF transport

mechanism for solvents through dense silicone membranes, J. Membr. Sci., 231 (2004) 99-108.

[200] M.J. Bridge, K.W. Broadhead, V. Hlady, P.A. Tresco, Ethanol treatment alters the ultrastructure and permeability of PAN-PVC hollow fiber cell encapsulation membranes, J. Membr. Sci., 195 (2001) 51-64.

[201] L.P. Raman, M. Cheryan, N. Rajagopalan, Solvent recovery and partial deacidification of vegetable oils by membrane technology, Fett/Lipid, 98 (1996) 10-14.

[202] D. Bhanushali, S. Kloos, C. Kurth, D. Bhattacharyya, Performance of solvent-resistant membranes for non-aqueous systems: Solvent permeation results and modeling, J. Membr. Sci., 189 (2001) 1-21.

[203] P. Silva, S. Han, A.G. Livingston, Solvent transport in organic solvent nanofiltration membranes, J. Membr. Sci., 262 (2005) 49-59.

[204] Y.H. Zhao, M.H. Abraham, A.M. Zissimos, Fast calculation of van der Waals volume as a sum of atomic and bond contributions and its application to drug compounds, The Journal of organic chemistry, 68 (2003) 7368-7373.

[205] S. Ilyas, N. Joseph, A. Szymczyk, A. Volodin, K. Nijmeijer, W.M. de Vos, I.F.J. Vankelecom, Weak polyelectrolyte multilayers as tunable membranes for solvent resistant nanofiltration, J. Membr. Sci., 514 (2016) 322-331.

[206] J. da Silva Burgal, L.G. Peeva, S. Kumbharkar, A. Livingston, Organic solvent resistant poly(ether-ether-ketone) nanofiltration membranes, J. Membr. Sci., 479 (2015) 105-116.

[207] S. Behnke, M. Ulbricht, Thin-film composite membranes for organophilic nanofiltration based on photo-cross-linkable polyimide, Reactive and Functional Polymers, 86 (2015) 233-242.

[208] M.F. Jimenez Solomon, Y. Bhole, A.G. Livingston, High flux membranes for organic solvent nanofiltration (OSN)-Interfacial polymerization with solvent activation,

J. Membr. Sci., 423-424 (2012) 371-382.

[209] H. Siddique, E. Rundquist, Y. Bhole, L.G. Peeva, A.G. Livingston, Mixed matrix membranes for organic solvent nanofiltration, J. Membr. Sci., 452 (2014) 354-366.

[210] G. Szekely, M.F. Jimenez-Solomon, P. Marchetti, J.F. Kim, A.G. Livingston, Sustainability assessment of organic solvent nanofiltration: from fabrication to application, Green Chemistry, 16 (2014) 4440-4473.

[211] A.A. Tashvigh, T.-S. Chung, Facile fabrication of solvent resistant thin film composite membranes by interfacial crosslinking reaction between polyethylenimine and dibromo-p-xylene on polybenzimidazole substrates, J. Membr. Sci., 560 (2018) 115-124.

[212] C. Van Goethem, R. Verbeke, S. Hermans, R. Bernstein, I. Vankelecom, Controlled positioning of MOFs in interfacially polymerized thin-film nanocomposites, J. Mater. Chem. A, 4 (2016) 16368-16376.

[213] I. Soroko, Y. Bhole, A.G. Livingston, Environmentally friendly route for the preparation of solvent resistant polyimide nanofiltration membranes, Green Chemistry, 13 (2011) 162-168.

[214] T. Renouard, A. Lejeune, M. Rabiller-Baudry, Separation of solutes with an organic solvent nanofiltration cascade: Designs, simulations and systematic study of all configurations, Separation and Purification Technology, 194 (2018) 111-122.

[215] D.Y. Xing, S.Y. Chan, T.-S. Chung, The ionic liquid [EMIM] OAc as a solvent to fabricate stable polybenzimidazole membranes for organic solvent nanofiltration, Green Chemistry, 16 (2014) 1383-1392.

[216] J. Campbell, R. Davies, D.C. Braddock, A. Livingston, Improving the permeance of hybrid polymer/metal–organic framework (MOF) membranes for organic solvent nanofiltration (OSN)–development of MOF thin films via interfacial synthesis, J. Mater. Chem. A, 3 (2015) 9668-9674.

[217] J. Shen, S. Shahid, A. Sarihan, D.A. Patterson, E.A. Emanuelsson, Effect of polyacid dopants on the performance of polyaniline membranes in organic solvent nanofiltration, Separation and Purification Technology, 204 (2018) 336-344.

[218] A. Figoli, T. Marino, S. Simone, E. Di Nicolo, X.-M. Li, T. He, S. Tornaghi, E. Drioli, Towards non-toxic solvents for membrane preparation: a review, Green Chemistry, 16 (2014) 4034-4059.

[219] S. Li, F. Qin, P. Qin, M.N. Karim, T. Tan, Preparation of PDMS membrane using water as solvent for pervaporation separation of butanol–water mixture, Green Chemistry, 15 (2013) 2180-2190.

[220] A.W. Mohammad, Y. Teow, W. Ang, Y. Chung, D. Oatley-Radcliffe, N. Hilal, Nanofiltration membranes review: Recent advances and future prospects, Desalination, 356 (2015) 226-254.

[221] S. Yuan, J. Wang, X. Li, J. Zhu, A. Volodine, X. Wang, J. Yang, P. Van Puyvelde, B. Van der Bruggen, New promising polymer for organic solvent nanofiltration: Oxidized poly (arylene sulfide sulfone), J. Membr. Sci., 549 (2018) 438-445.

[222] J.H. Kim, M. Cook, S.H. Park, S.J. Moon, J.F. Kim, A.G. Livingston, Y.M. Lee, A compact and scalable fabrication method for robust thin film composite membranes, Green Chemistry, 20 (2018) 1887-1898.

[223] Z. Zhang, N. Lee, K. Patel, M. Young, J. Zhang, S. Percec, S. Ren, Poly (P-Phenylene Terephthalamide) Fibers Reinforced with Ultrathin Ceramic Coatings, Adv. Eng. Mater., (2018) 1800095.

[224] J. Lyu, X. Wang, L. Liu, Y. Kim, E.K. Tanyi, H. Chi, W. Feng, L. Xu, T. Li, M.A. Noginov, High Strength Conductive Composites with Plasmonic Nanoparticles Aligned on Aramid Nanofibers, Adv. Funct. Mater., 26 (2016) 8435-8445.

[225] L. Xu, X. Zhao, C. Xu, N.A. Kotov, Water-Rich Biomimetic Composites with Abiotic Self-Organizing Nanofiber Network, Adv. Mater., 30 (2018).

[226] P. Zschocke, H. Strathmann, Solvent resistant membranes from poly-(p-phenylene-terephthalamide), Desalination, 34 (1980) 69-75.

[227] C. Wang, C. Xiao, Q. Huang, J. Pan, A study on structure and properties of poly (p-phenylene terephthamide) hybrid porous membranes, J. Membr. Sci., 474 (2015) 132-139.

[228] M. Yang, K. Cao, L. Sui, Y. Qi, J. Zhu, A. Waas, E.M. Arruda, J. Kieffer, M. Thouless, N.A. Kotov, Dispersions of aramid nanofibers: a new nanoscale building block, ACS nano, 5 (2011) 6945-6954.

[229] J. Zhu, M. Yang, A. Emre, J.H. Bahng, L. Xu, J. Yeom, B. Yeom, Y. Kim, K. Johnson, P. Green, Branched aramid nanofibers, Angew. Chem., (2017).

[230] Q.G. Zhang, C. Deng, F. Soyekwo, Q.L. Liu, A.M. Zhu, Sub-10 nm Wide Cellulose Nanofibers for Ultrathin Nanoporous Membranes with High Organic Permeation, Adv. Funct. Mater., 26 (2016) 792-800.

[231] F. Soyekwo, Q. Zhang, R. Gao, Y. Qu, C. Lin, X. Huang, A. Zhu, Q. Liu, Cellulose nanofiber intermediary to fabricate highly-permeable ultrathin nanofiltration membranes for fast water purification, J. Membr. Sci., 524 (2017) 174-185.

[232] R.R. Burch, W. Sweeny, H.W. Schmidt, Y.H. Kim, Preparation of aromatic polyamide polyanions: a novel processing strategy for aromatic polyamides, Macromolecules, 23 (1990) 1065-1072.

[233] X. Loh, M. Sairam, A. Bismarck, J. Steinke, A. Livingston, K. Li, Crosslinked integrally skinned asymmetric polyaniline membranes for use in organic solvents, J. Membr. Sci., 326 (2009) 635-642.

[234] I. Strużyńska-Piron, J. Loccufier, L. Vanmaele, I.F. Vankelecom, Synthesis of solvent stable polymeric membranes via UV depth-curing, Chem. Commun., 49 (2013) 11494-11496.

Curriculum Vitae

SHUSHAN YUAN

Date of birth: November 4th, 1987

Nationality: Chinese

Gender: Male

CONTACT

Process Engineering for Sustainable Systems (ProcESS)

Department of Chemical Enigineering

KU Leuven Chem & Tech

Celestijnenlaan 200F

3001 Heverlee, Leuven, Belgium

Tel: (+32) 485632238

Email: shushan.yuan@kuleuven.be; shushanyuan@163.com

EDUCATION

Sept. 2015-present	Ph.D	Chemical engineering KU Leuven, Belgium
Sept. 2012-Jun. 2015	Master	College Polymer Science and Engineering, Sichuan University, China
Sept. 2008-Jun. 2012	Bachelor	College Polymer Science and Engineering Sichuan University, China

RESEARCH INTERESTS

- 3D printing of membrane and module for different application.
- Synthesis novel 2D polymers for high performance nanofiltration membrane.
- Preparation of organic solvent nanofiltration membrane from high-performance polymers.

PPUBLICATIONS

1) **Shushan Yuan**, Jian Li, Junyong Zhu, Alexander Volodine, Jiansheng Li, Gang Zhang, Peter Van Puyvelde, Bart Van der Bruggen, Hydrophilic nanofiltration membranes with reduced humic acid fouling fabricated from copolymers designed by introducing carboxyl groups in the pendant benzene ring, *Journal of Membrane Science*, 563 (2018) 655-663.

2) Junyong Zhu, Jingwei Hou, Ruijun Zhang, **Shushan Yuan***, Jian Li, Miaomiao Tian, Penghui Wang, Alexander Volodine, Yatao Zhang*, Bart Van der Bruggen, Rapid water transport through controllable, ultrathin polyamide nanofilms for high-performance nanofiltration. *Journal of Materials Chemistry A*, 2018, DOI:10.1039/C8TA05687K.

3) **Shushan Yuan**, Junyong Zhu, Jian Li, Alexander Volodine, Jie Yang, Peter Van Puyvelde, Bart Van der Bruggen, Nano/microstructure decorated thin film composite poly (arylene sulfide sulfone) membrane constructed by induced fouling in organic solvent ultrafiltration, *Chemical Engineering Journal,* 348(2018)180-190.

4) **Shushan Yuan**, Dieter Strobbe, Jean-Pierre Kruth, Peter Van Puyvelde, Bart Van der Bruggen, Super-hydrophobic 3D printed polysulfone membranes with a

switchable wettability by self-assembled candle soot for efficient gravity-driven oil/water separation, *Journal of Materials Chemistry A*, (2017)25401-25409.

5) **Shushan Yuan**, Dieter Strobbe, Jean-Pierre Kruth, Peter Van Puyvelde, Bart Van der Bruggen, Production of polyamide-12 membranes for microfiltration through selective laser sintering, Journal of Membrane Science, 525 (2017) 157-162.

6) **Shushan Yuan**, Juan Wang, Xin Li, Junyong Zhu, Alexander Volodine, Xiaojun Wang, Jie Yang, Peter Van Puyvelde, Bart Van der Bruggen, New promising polymer for organic solvent nanofiltration: Oxidized poly (arylene sulfide sulfone), Journal of Membrane Science, 549 (2018) 438-445.

7) **Shushan Yuan**, Juan Wang, Xiaojun Wang, Shengru Long, Gang Zhang, Jie Yang,Poly(arylene sulfide sulfone) hybrid ultrafiltration membrane with TiO2-g-PAA nanoparticles: Preparation and antifouling performance, Polymer Engineering and Science, 12 (2015)2829-2837

8) Junyong Zhu, **Shusha Yuan**, Adam Uliana, Jingwei Hou, Jian Li, Xin Li, Miaomiao Tian, Ying Chen, Alexander Volodin, Bart Vander Bruggen, High-flux thin film composite membranes for nanofiltration mediated by a rapid co-deposition of polydopamine/piperazine, *Journal of Membrane Science*, (2018).

9) Jian Li, **Shushan Yuan**, Jing Wang, Junyong Zhu, Jiangnan Shen, Bart Van der Bruggen, Mussel-inspired modification of ion exchange membrane for monovalent separation, *Journal of Membrane Science*, (2018).

10) Gang Zhang, **Shushan Yuan**, Zhimin Li, Shengru Long, Jie Yang, Poly (arylene ether sulfone) containing thioether units: synthesis, oxidation and properties, *RSC Advances*, 4 (2014) 23191-23201.

11) Jian Li, Junyong Zhu, **Shushan Yuan**, Jiuyang Lin, Jiangnan Shen, Bart Van der Bruggen, Cation-Exchange Membranes with Controlled Porosity in Electrodialysis

Application, *Industrial & Engineering Chemistry Research*, 56 (2017) 8111-8120.

PATENTS

1) Jie Yang, **Shushan Yuan**, Yue Wang, Xiaojun Wang, Gang Zhang, Shengru Long; One kind of polyarylene sulfide sulfone / sulfonated polymer composite separation membrane and its preparation method. No **CN104209024B**.

2) Jie Yang, Yue Wang, **Shushan Yuan**, Xiaojun Wang, Gang Zhang, Shengru Long; Reinforced solvent-resistant polyarylene sulfide sulfone hollow fiber membrane and its preparation method. No **CN105032218B**.

CONFERENCE

1) **Shushan Yuan**, New promising polymer for organic solvent nanofiltration: oxidized poly (arylene sulfide sulfone), 6thInternational Conference on Organic Solvent Nanofiltration, 04-06.06.2017, Saint-Petersburg, Russia.